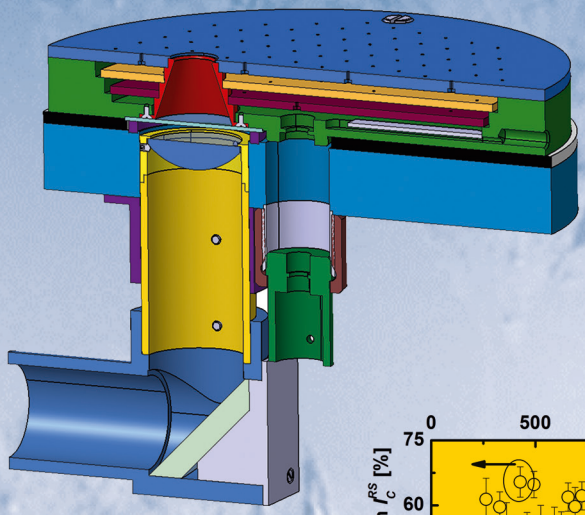

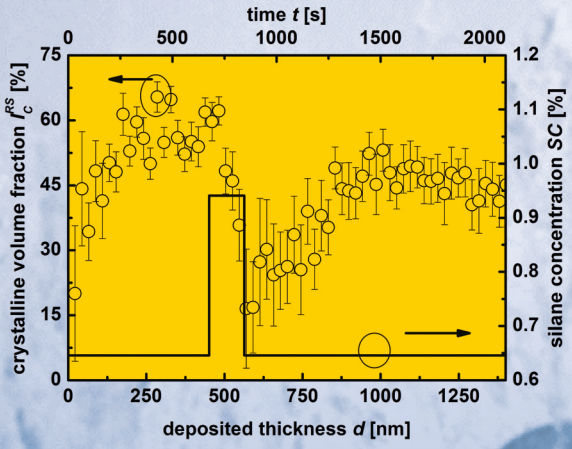

In-Situ Raman Spectroscopy: A Method to Study and Control the Growth of Microcrystalline Silicon for Thin-Film Solar Cells

Stefan Muthmann

Mitglied der Helmholtz-Gemeinschaft

JÜLICH
FORSCHUNGSZENTRUM

Schriften des Forschungszentrums Jülich
Reihe Energie & Umwelt / Energy & Environment Band / Volume 133

Forschungszentrum Jülich GmbH
Institut of Energy and Climate Research (IEK)
Photovoltaics (IEK-5)

In-Situ Raman Spectroscopy: A Method to Study and Control the Growth of Microcrystalline Silicon for Thin-Film Solar Cells

Stefan Muthmann

Schriften des Forschungszentrums Jülich
Reihe Energie & Umwelt / Energy & Environment Band / Volume 133

ISSN 1866-1793 ISBN 978-3-89336-774-0

Bibliographic information published by the Deutsche Nationalbibliothek.
The Deutsche Nationalbibliothek lists this publication in the Deutsche Nationalbibliografie; detailed bibliographic data are available in the Internet at http://dnb.d-nb.de.

Publisher and Distributor:	Forschungszentrum Jülich GmbH Zentralbibliothek 52425 Jülich Phone +49 (0) 24 61 61-53 68 · Fax +49 (0) 24 61 61-61 03 e-mail: zb-publikation@fz-juelich.de Internet: http://www.fz-juelich.de/zb
Cover Design:	Grafische Medien, Forschungszentrum Jülich GmbH
Printer:	Grafische Medien, Forschungszentrum Jülich GmbH
Copyright:	Forschungszentrum Jülich 2012

Schriften des Forschungszentrums Jülich
Reihe Energie & Umwelt / Energy & Environment Band / Volume 133

D 82 (Diss., RWTH Aachen University, 2012)

ISSN 1866-1793
ISBN 978-3-89336-774-0

The complete volume is freely available on the Internet on the Jülicher Open Access Server (JUWEL) at http://www.fz-juelich.de/zb/juwel

Abstract

Optimum performance of a microcrystalline silicon (μc-Si:H) thin-film solar cell is achieved if the absorber layer material is deposited close to the phase transition towards amorphous Silicon. Hence exact knowledge about and control of the deposition process is of great importance. Raman spectroscopy is a characterization method, which allows to determine whether important material properties fulfill the requirements of the narrow process window. This work deals with the design and application of a novel experiment, which enables in-situ Raman measurements during the parallel plate plasma enhanced chemical vapor deposition (PECVD) of μc-Si:H. Measurements of the crystalline volume fraction (I_C^{RS}) and the temperature of a growing film are carried out using the novel setup. To enable in-situ Raman measurement of central regions of the coated substrate in a PECVD system, optical access under normal incidence is necessary. An experimental setup in which an optical feed-through was integrated into a PECVD electrode was developed. This setup introduces a disturbance to the electrical field which sustains the plasma. By designing metallic shields the impact of the feed through was reduced considerably at low optical losses. The homogeneity of films deposited with the novel setup in different growth regimes was studied. A correlation between the magnitude of the inhomogeneity caused by the feed-through and the characteristics of the deposition regimes is found. Raman spectroscopy demands the illumination of a sample with a laser and the collection of the scattered radiation. Due to absorption of the laser light the temperature of the illuminated film is increased. Since the temperature determines the properties of a growing film the laser-induced temperature increase was studied. By pulsing the laser radiation a minimal temperature increase at maximal signal intensity was obtained. The crystalline volume fraction of a growing μc-Si:H layer was determined in-situ with the novel setup. A minimal temporal resolution of less than 17.5 s at sufficient signal-to-noise-ratio was achieved, which corresponds

to less than 9 nm of deposited material during one measurement interval at the industrial standard growth rate of 0.5 nm/s. The obtained results were compared to depth resolved measurements which were carried out after the deposition. An excellent agreement between both methods validates the reliability of the in-situ method. The initial phase of deposition is of great importance for the performance of a μc-Si:H thin-film solar cell. Hence the dependence of the evolution of the crystalline volume fraction during initial layer growth on the properties of the underlying seed layer was studied in-situ. A seed layer dependent increase and subsequent stabilization of the crystalline volume fraction was observed. By actively controlling the deposition parameters based on these results it was possible to reduce the observed inhomogeneity of the Raman crystallinity in growth direction. A possible application of in-situ Raman spectroscopy as basis of an active process control was studied by testing the ability of in-situ Raman spectroscopy to detect fluctuations of the deposition parameters on the example of a disturbance of the process gas flow. It was possible to detect the reaction of the layer growth on a change of deposition conditions in-situ. By correlating the in-situ measurements to results obtained on solar-cells it was found that – unless the process fluctuation happens during the initial phase of deposition– it is possible to maintain state-of-the art solar cell performance by an active process control. Raman spectroscopy can be used to measure the temperature of a film. Up to now, it was only possible to estimate this important process parameter by measurements of the substrate temperature using a pyrometer. Raman Spectroscopy enables the direct determination of the temperature of a growing film. By modulating the plasma emission synchronized to the Raman measurements the signal-to-noise level of the Raman measurements was reduced. Hence the sensitivity of the measurements was increased to a level, which enables the in-situ determination of the film temperature. Two deposition regimes were distinguished by their characteristic plasma induced temperature increase. In situ measurements show that an active control of the substrate heater results in a stabilized temperature of the growing layer throughout the deposition of a μc-Si:H film.

Zusammenfassung

Optimales Absorbermaterial für mikrokristalline (μc-Si:H) Dünnschichtsolarzellen erhält man in einem engen Prozessfenster, nahe am Phasenübergang zu amorphem Silizium. Deshalb sind das genaue Verständnis und die Kontrolle des Abscheidprozesses von großer Bedeutung. Raman Spektroskopie ist eine Messmethode, mit der man beobachten kann, ob wichtige Materialeigenschaften den Anforderungen des schmalen Prozessfensters genügen. Die vorliegende Arbeit beschreibt die Entwicklung und Anwendung eines neuartigen Messaufbaus, der es erlaubt während der Plasma unterstützten chemischen Gasphasen Abscheidung (PECVD) Raman Spektroskopie zu betreiben. Der neue Aufbau wurde benutzt um in-situ Messungen des kristallinen Volumenanteils (I_C^{RS}) und der Temperatur einer wachsenden μc-Si:H Schicht zu bestimmen. Um Raman-Spektroskopie an zentralen Bereichen eines beschichteten Substrats in einem PECVD System durchführen zu können benötigt man optischen Zugang unter senkrechtem Einfall. Ein Messaufbau, der eine optische Durchführung in eine PECVD Elektrode integriert, und minimalen Einfluss auf das Wachstum von dünnen Silizium Schichten nimmt, wurde entwickelt. Dieser Aufbau führt zu Störungen des elektrischen Feldes, mit dem das Plasma erzeugt wird. Durch den Einsatz von elektrischen Abschirmungen wurde der Einfluss der optischen Durchführung bei guter optischer Transparenz stark verringert. Die Homogenität von Schichten die mit dem neuen Aufbau in verschiedenen Wachstumsregimen wurde untersucht. Ein Zusammenhang zwischen der Ausprägung der Inhomogenität die durch die Durchführung verursacht wird und den Eigenschaften der Depositionsregime wurde beobachtet. Da Raman Spektroskopie mittels elastischer Streuung von Laserstrahlung durchgeführt wird kann die untersuchte Schicht durch die Messungen erhitzt werden. Da die Temperatur das Schichtwachstum entscheidend beeinflusst wurde die Aufheizung der Schicht durch Raman Messungen untersucht. Durch Modulieren der Laserleistung wurde maximale Signalintensität bei minimaler Aufheizung er-

reicht. Mit dem neuentwickelten Messaufbau wurden Messungen von I_C^{RS} während der Abscheidung von μc-Si:H durchgeführt. Eine exzellente zeitliche Auflösung von etwa 17.5 s, bei guter Auswertbarkeit der aufgenommenen Spektren, wurde erreicht. Bei einer industriellen Standardwachstumsrate von etwa 0.5 nm/s entspricht diese zeitliche Auflösung weniger als 9 nm Siliziumabscheidung innerhalb eines Messintervalls. Ein Vergleich der in-situ Messungen mit tiefenaufgelösten Daten, die nach der Schichtabscheidung gewonnen wurden, zeigt eine sehr gute Übereinstimmung beider Methoden. Da der Beginn der Absorber-Abscheidung von großem Einfluss für die Eigenschaften einer μc-Si:H Dünnschichtsolarzelle ist wurde die Entwicklung von I_C^{RS} während dieser Abscheidungsphase untersucht. Der Einfluss von Saatschichten auf das Wachstumsverhalten des Absorbers konnte bestimmt werden. Eine Zunahme und anschließende Stabilisierung von I_C^{RS} wurde während der Anfangsphase des Wachstums beobachtet. Es konnte gezeigt werden, dass mit einer aktiven Regelung des Gasflusses eine Verbesserung der Homogenität in Wachstumsrichtung erreicht werden kann. Ein möglicher Einsatz von in-situ Raman-Spektroskopie als Grundlage für eine aktive Prozessregelung wurde anhand des Beispiels einer Störung des Prozessgasflusses während des Absorber-Wachstums einer Silizium Dünnschicht Solarzelle untersucht. Es konnte gezeigt werden, dass Prozessstörungen mit dem neuentwickelten Messaufbau detektiert werden können. Durch Korrelation der in-situ Messungen zu den Parametern von Solarzellen wurde festgestellt, dass es möglich ist, die Leistungsfähigkeit einer Solarzelle durch aktive Prozesskontrolle aufrechtzuerhalten, wenn die Störung der Prozessbedingungen nicht in der Anfangsphase der Abscheidung stattfindet. Raman Spektroskopie ermöglicht die Messung der Temperatur einer wachsenden Schicht. Bisher wurde dieser wichtige Parameter durch die Substrattemperatur angenähert. Raman Spektroskopie ermöglicht die direkte Messung der Schichttemperatur. Durch eine Modulation des Plasmas, die mit den Raman Messungen synchronisiert wurde, konnte eine starke Verringerung des Messrauschens erreicht werden. Dadurch wurden Temperaturmessungen basierend auf Raman Spektroskopie ermöglicht. Zwei Depositionsregime wurden anhand ihres plasmainduzierten Temperaturanstiegs unterschieden. Durch aktive Regelung der Substratheizung konnte eine Stabilisierung der Schichttemperatur während des Wachstums einer μc-Si:H Schicht erreicht werden.

List of Abbreviations and Symbols

μc-Si:H	microcrystalline silicon
a-Si:H	amorphous silicon
c-Si	crystalline silicon
TCO	transparent conductive oxide
ZnO	zinc oxide
IV-characteristics	current-voltage-characteristics
$I_{\mathrm{C}}^{\mathrm{RS}}$	Raman crystallinity
TEM	transmission electron microscopy
SiH_4	Silane
SiH_3	Silyl radical
p	deposition pressure
SC	silane concentration
T	temperature
e	elementary charge
ϵ_0	vacuum electric permitivity
P	discharge power density
V_{oc}	open-circuit voltage
J_{sc}	short-circuit current density
FF	Fill Factor
V_{m}	voltage at maximum power point
J_{m}	current density at maximum power point
P_{m}	maximum power point
P_{ill}	illuminating power
V_{bi}	built in potential
E_{C}	conduction band
E_{V}	valence band
E_{F}	Fermi level
I_{480}	Integrated intensity of amorphous contribution to Raman spectrum

I_{520}	Integrated intensity of crystalline contribution to Raman spectrum
R_{T}	Stokes/anti-Stokes intensity ratio
T_{l}	lattice temperature
d_{op}	diameter of an opening
V_{P}	plasma potential
n_{i}	ion density
d_{sh}	sheath width
λ_{db}	debye length
n_{e}	electron density
d_{inf}	information depth
d_{el}	electrode distance
d_{pl}	plasma bulk thickness
t_{cool}	cool down time between pulses
T_{S}	substrate temperature
T_{H}	heater temperature
ΔT	laser induced temperature increase
T_{crys}	crystallization temperature
l_{p}	pulse length
I_{tot}	total signal intensity
σ_{noise}	standard deviation of the measurement noise
A_{circ}	area of a circular laser spot
A_{elip}	area of an elliptical laser spot
l_{th}	thermal penetration depth
n	index of refraction
n_{eff}	effective index of refraction
c_{P}	heat capacity at constant pressure
λ_{th}	thermal conductivity
ρ	density
d_{max}	maximal thickness
I_0	initial intensity
l_{diff}	diffraction limit
d_{foc}	focal length
d_{beam}	beam diameter
T_{min}	minimum temperature
Δt	time difference between two maxima/minima of intensity
t_{int}	integration time of the CCD
n_{acc}	number of accumulations
t_{tot}	total integration time
t_{net}	net integration time

t_{read}	CCD read out time
t_{shut}	shutter open/close time
R_{d}	deposition rate
$I_{\mathrm{sub,0}}$	initial substrate contribution
d_{avg}	average layer thickness during one measurement interval
t_{dep}	deposition time
I_{SC}	SiH to H_β intensity ratio
T_{heat}	heater temperature
T_{glass}	substrate temperature
t_{spec}	spectrometer chopper open time
t_{off}	plasma off time
DF-image	dark field image
BF-image	brigth field image
SAED	selected area electron diffraction
t_{glow}	afterglow time off a plasma
t_{dark}	total plasma dark time
t_{on}	on time off a plasma
v_{rates}	ratio between pulsed and cw deposition rate
d_{grid}	distance between grid lines
t_{dis}	position of a disturbance in intrinsic layer
w_{dis}	width of a disturbance in intrinsic layer
T_{film}	film temperature
$\Delta\, T$	Temperature increase
C_{Ram}	Calibration constant
$\mathrm{k_B}$	Boltzmann's Constant
I_{ph}	Photo current
SC_{p}	Silane Concentration during p-layer deposition
SC_{I}	Silane Concentration during i-layer deposition
$R_{\mathrm{d,cw}}$	deposition rate during continous plasma deposition
$R_{\mathrm{d,pulse}}$	deposition rate during pulsed plasma deposition

Contents

1 Introduction

Technological improvements in a modern society are often directly related to an increased demand for primary energy. Due to the fact that the emerging countries, which account for more than 80 % of the world population [1], have continuously been adapting their lifestyle to that of the western world, the demand for cheap energy will rise drastically in the future. With the momentary energy mix it will certainly not be possible to cope with this rising demand in the long run. In 2009 only 16 % of the global final energy consumption was provided by renewable energy sources. Fossil fuels supplied the majority (81 %) assisted by nuclear power, which provided a small share (2.8 %) [2]. Obviously, the combination of growing demand and dwindling resources, which is given for the current situation, is designated to fail in the near future. The global climatic change and the rising prices for fossil fuels are only some indicators for the challenge that has to be tackled if we want to sustain our momentary lifestyle. The sun provides more than enough of the desired energy: the amount of solar-energy which our planet receives during one hour is large enough to meet the world's energy demand for one year. Photovoltaic is one way to make use of this abundance.

The price is the strongest argument for whether a technology will prevail on a free market. Future challenges like the effects on the ecosystems or the waste management are often neglected in the decision making process. Hence the price per kilowatt-hour generated by a solar cell is the main argument for the success of this technology.

Thin-film silicon has long been considered as a means to reduce the production costs for solar panels. Low raw material consumption, high throughput, and large module areas are the major advantages of this technology. Maximum initial efficiencies of 16.3 % have been reported for multi-junction devices made from thin-film silicon [3]. To increase the efficiency even further and to keep the module prices low, an active control of the material growth will be of increasing

importance in the future. Since the process window used to deposit optimum microcrystalline silicon material is narrow, an improved understanding and control of the involved growth mechanisms are especially important for this material type. Increasing attention has been drawn to in-situ studies of the growth of thin-film materials:

Real-time spectroscopic ellipsometry is used to study the deposition of amorphous [4, 5, 6] and microcrystalline silicon [7, 8, 9]. This method uses optical models to obtain information about the properties of a growing film. The crystalline volume fraction and the deposition rate of microcrystalline silicon are obtained during deposition by in-situ transmission measurements that use plasma as light source [10, 11]. To obtain information about the plasma, which can be correlated to the properties of a growing thin film, optical emission spectroscopy is widely applied [12, 13, 14, 15, 16, 17, 18].

Raman spectroscopy has been applied previously during the remote plasma deposition of microcrystalline silicon to obtain information about the structural properties and the temperature of a growing silicon layer [19]. The crystalline volume fraction of the microcrystalline silicon absorber layer can be directly correlated to the properties of a thin-film silicon solar cell [20]. Raman spectroscopy is widely applied to determine this important material property [21, 22, 23, 24]. The Raman effect describes the inelastic scattering of light in solids, in which phonons are either created (Stokes-process) or annihilated (anti-Stokes process) [25]. Due to the fact that phonons participate in the Raman scattering, it is also possible to determine the temperature of a growing film with this method [26].

To enable Raman spectroscopy inside a parallel plate plasma-enhanced chemical vapor deposition (PECVD) system, an optical feed through penetrating one of the electrodes is necessary. Hence a disturbance is introduced to the electrical field that generates the plasma. The effect of the disturbance has to be minimized in order to obtain in-situ information that is not only valid for the studied area but also for the rest of the coated substrate. The prerequisite of undisturbed growth poses some challenges regarding the inclusion of an in-situ Raman setup into a parallel plate PECVD system:

On the one hand the intensity of the collected Raman scattered radiation has to be maximized. On the other hand central regions of the coated substrate are of interest for the in-situ measurements since they determine the properties

of a solar module. Hence modifications to the deposition system and optimized measurement parameters, which meet both demands, have to be developed.

The properties of thin-film silicon, the preparation of the layers, and the applied characterization techniques are described in **Chapter 2**.

In **Chapter 3** the implementation of an in-situ Raman experiment into an existing PECVD system is described. The impact of the experiment on a growing film is studied and minimized.

Chapter 4 deals with the parameters used to perform in-situ measurements of the Raman crystallinity with the newly developed system. First measurements are carried out and compared to data obtained after the deposition of the film. The evolution of the crystalline volume fraction during the initial phase of deposition is studied in detail.

The applicability of the in-situ experiment as a means of process control is tested in **Chapter 5**. The influence of a disturbance in the process gas flow on the properties of solar cells is described and the possibility of the in-situ experiment to guide an active process control is discussed.

In **Chapter 6** measurements of the temperature of a growing film are carried out. Pulsed plasma deposition is described as a method to increase the accuracy and temporal resolution of the obtained measurements. The temperature characteristics obtained in two different growth regimes are studied. An example of an active stabilization of the film temperature, which is guided by in-situ measurements, is given.

2 Theory and Experimental Methods

In this chapter the properties of thin film silicon are summarized and the working principle of solar cells is explained. The deposition system and the plasma enhanced chemical vapor deposition method are described. The major characterization techniques used during this thesis are discussed.

2.1 Thin Film Silicon

Two configurations of thin film silicon are deposited with plasma enhanced chemical vapor deposition (PECVD): Amorphous (a-Si:H) and microcrystalline (μc-Si:H) silicon. The important characteristics of these materials and the properties of thin-film silicon solar cells are discussed in this section.

2.1.1 Hydrogenated Amorphous Silicon

Amorphous silicon is a material of great technological importance. Solar cells based on amorphous silicon have been introduced in the seventies of the last century. The conversion efficiency of the first a-Si:H solar cell reported by Carlson and Wronski was as low as 2.4 % [27]. Presently stabilized efficiencies of up to 10.1 % have been acchieved with single junction a-Si:H solar cells [28].

A classical theoretical treatment of electrons in semiconductors is based on the periodic structure of atoms in a crystal. The tetrahedral arrangement of crystalline silicon is maintained in a-Si:H on length scales of a few neighboring atoms. The missing order on larger scales leads to a relaxation of the law of momentum conservation for electronic transitions. An important consequence of

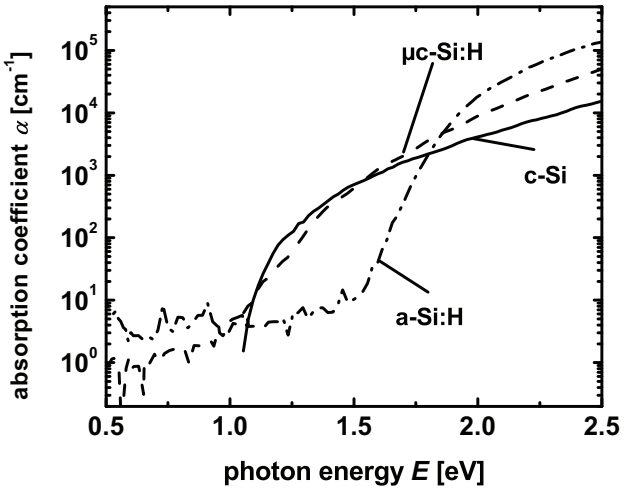

Figure 2.1: Absorption coefficient of amorphous and microcrystalline silicon compared to that of c-Si [30].

the missing conservation of momentum in a-Si:H is that amorphous silicon acts as a direct semiconductor when light absorption is considered. This explains the fact that the absorption coefficient of a-Si:H above photon energies of 1.8 eV is considerably higher than that of crystalline silicon (c-Si) as seen in Figure 2.1. The figure also shows that no clear definition of an optical band gap can be made for amorphous silicon. Instead the optical gap is described by e.g. the E_{04} or the Tauc gap [29]. The missing long range order in amorphous silicon leads to the fact that a large number of unsaturated bonds that generate defect states is created. A majority of these so called dangling bonds are passivated by the incorporation of hydrogen. The so created material is known as hydrogenated amorphous silicon.

The major drawback of a-Si:H is the so called Staebler-Wronski-Effect which describes the reversible degradation of the photo and the dark conductivity of a-Si:H thin films upon illumination [31].

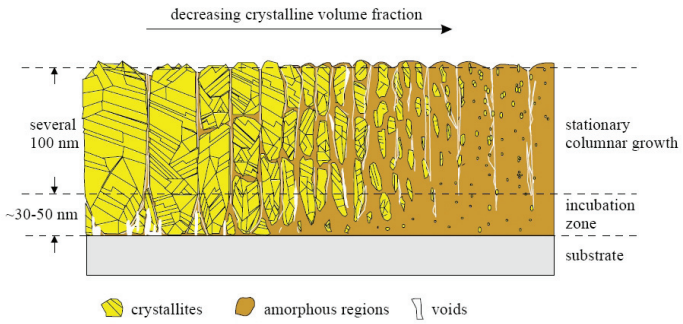

Figure 2.2: Schematic diagram illustrating the microstructural features of μc-Si:H grown by PECVD. The crystalline volume fraction decreases from left to right. The Figure is taken from [20]

2.1.2 Hydrogenated Microcrystalline Silicon

From the first report about microcrystalline silicon by Veprek *et al.* in 1968 [32] to the realization of a μc-Si:H solar cell by Faraji *et al.* [33] 24 years passed by. This might be due to the fact that the homogeneous deposition of μc-Si:H is much more challenging than that of a-Si:H. Also the microstructure is more complex since μc-Si:H is best described as an amorphous matrix with embedded microcrystalline grains. This phase mixture is characterized by the crystalline volume fraction which describes the ratio of the crystalline volume to the amorphous fraction of a sample. Figure 2.2 schematically shows the composition of a microcrystalline film with different crystalline volume fractions. This figure was obtained using a combination of various characterization techniques like X-ray diffraction, transmission electron microscopy and Raman spectroscopy [20]. The left side of Figure 2.2 illustrates material with a high crystalline volume fraction. Here the crystalline regions are no perfect single grains with undisturbed translational symmetry. Stacking faults and unpassivated twin defects separate perfectly coherent individual crystals that grow in a columnar fashion. Even so the columns can be considered as separate units since the lattice orientation is maintained throughout an entire column. With a typical size of about 20 nm the length scale of undisturbed grains is considerably smaller than that of the columns [34, 22, 35]. The optimum material for solar cell absorber material de-

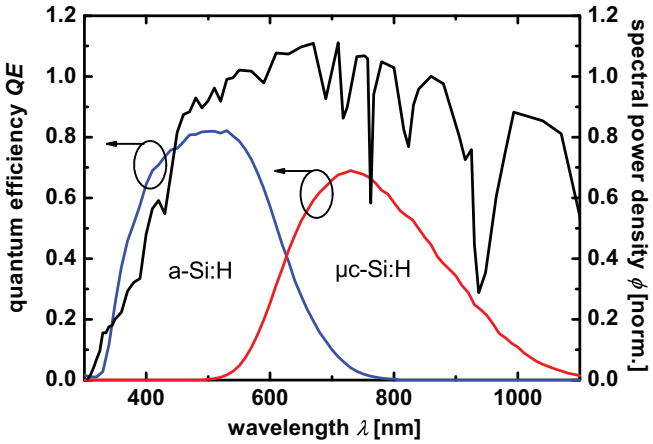

Figure 2.3: Quantum efficiency of a tandem solar cell and spectral power density of AM 1.5 irradiation (black). The photons with a low wavelength are mainly absorbed in the a-Si:H top cell (blue color). Photons with an energy below the a-Si:H bandgap of 1.8 eV are absorbed in the μc-Si:H bottom cell (red)

posited with plasma enhanced chemical vapor deposition (PECVD) lies close to the phase transition towards amorphous material with a crystalline volume fraction between 40 % to 60 % [20, 36]. The electronic properties of the material represented by the right side of Figure 2.2 are strongly degraded [37].

Due to the complex structure, the optical and electrical properties of μc-Si:H are determined by its composition. A great number of studies dealing with the interdependence of structural, optical and electrical properties has been published in the last two decades of which a summary is given in Reference [38].

The achieved maximal efficiencies of 10.1 % for μc-Si:H single junction solar cells [39] are in the same region as those of a-Si:H devices. Due to the smaller absorption coefficient above the bandgap of μc-Si:H, as seen in Figure 2.1, higher absorber layer thicknesses are necessary for microcrystalline silicon solar cells. It can also be seen in Figure 2.1 that the optical bandgap of μc-Si:H is much smaller than that of a-Si:H. This means that by combination of the two silicon config-

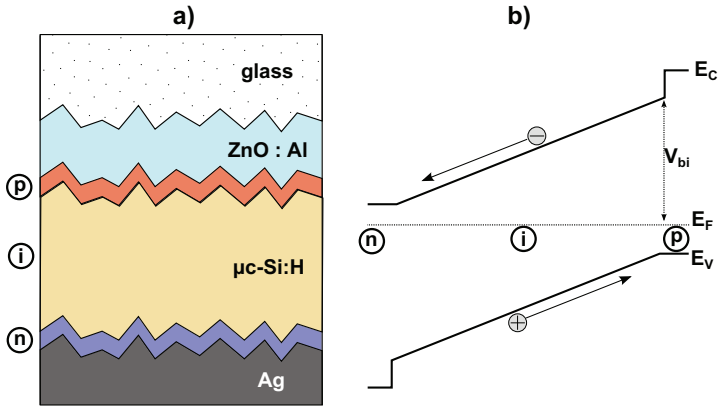

Figure 2.4: a) Schematic structure of a thin film silicon solar cell. The cell is illuminated from the top side. The front contact is typically zinc oxide. The silver back reflector acts as electrical back contact and ,additionally, reflects the light back into the cell.
b) Conduction band (E_{C}), valence band (E_{V}), Fermi level (E_{F}), and built in potential (V_{bi}) in a pin solar cell.

urations in a so called tandem structure the sunlight is utilized very efficiently. This is illustrated by measurements of the combined quantum efficency (QE) as shown in Figure 2.3. The measuremet procedure to obain QE is described e.g. in Reference [40]. A tandem cell increases the utilization of the solar spectrum leading to record efficiencies of 11.9 % [41].

2.1.3 Thin-Film Silicon Solar Cells

The photovoltaic effect which converts electro-magnetic radiation into electricity was first observed by Becquerel [42]. In a solar cell electron hole pairs are generated by the absorption of photons. The charge carriers are separated at selective contacts, that represent a barrier for either the holes or the electrodes, and extracted from the device. Conventional crystalline silicon solar cells are realized by a p/n-junction. A mono or polycrystalline wafer which is typically p-type doped is implanted with n-type dopands on the illuminated side.

The p/n type solar cell is not suitable for thin-film silicon due to the low

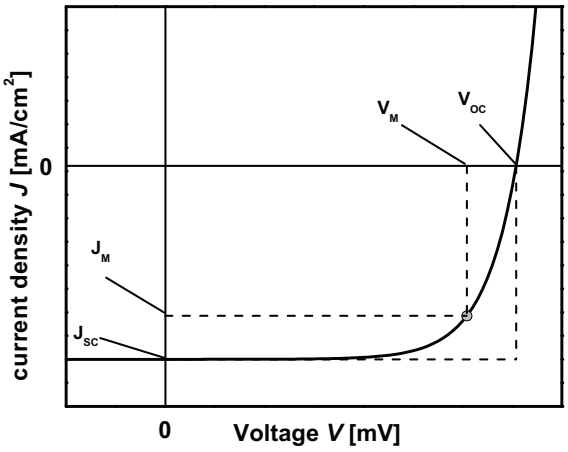

Figure 2.5: Current voltage characteristics of a solar cell under illumination. Voltage (V_{m}) and current density (J_{m}) at the maximum power point are indicated as well as the short-circuit current density (J_{sc}) and the open-circuit voltage (V_{oc}).

mobility in doped a-Si:H and μc-Si:H. To overcome this problem the concept of the drift type solar cell with an intrinsic absorber is introduced as seen in Figure 2.4. In this type of solar cell the majority of the electrons/hole pairs is generated in the intrinsic layer. The selectivity of the contacts is provided by thin p- and n-type layers. Due to the built in potential (V_{bi}), that is illustrated in Figure 2.4, an electric field extends over the whole intrinsic layer and supports the carrier extraction which is beneficial for low mobilities [43].

The front contact shown in Figure 2.4 a) is realized by a transparent conductive oxide (TCO), which in case of this thesis, sputtered Zinc Oxide (ZnO) is used as the TCO [44, 45]. The surface of the TCO is structured by a wet-chemical etching step. Due to the rough surface the impinging light is scattered into the film leading to an effectively higher absorption length. A silver back contact additionally increases the pathlength of the light in the silicon absorber by back reflection. The combination of these path enhancing methods, which

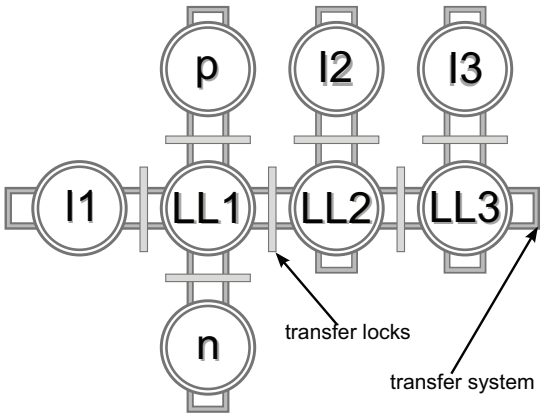

Figure 2.6: Layout of the plasma enhanced chemical vapor deposition system. The chambers used for the deposition of intrinsic layers are labeled I1, I2 and I3. The doped layers are deposited in the p and n chamber for p- and n-type doping respectively to avoid cross contamination. The load and transfer chambers are labeled LL1, LL2 and LL3

is also referred to as light trapping effect, enables a reduction of the absorber thickness. A reduced absorber thickness leads to less recombination and hence an improved carrier extraction.

The performance of a solar cell is described by its current-voltage (IV)-characteristics under illumination which is schematically shown in Figure 2.5. The efficiency η is defined as the ratio between the maximum power (P_{m}) that is extracted and the illuminating power (P_{ill})

$$\eta = \frac{P_{\mathrm{m}}}{P_{\mathrm{ill}}}. \tag{2.1}$$

The open-circuit voltage (V_{oc}) describes the voltage at which no current is extracted and the short-circuit current density (J_{sc}) is defined as the current density at zero voltage. These two parameters are linked to P_{m} by the fill factor (FF)

$$FF = \frac{\mathrm{P}_m}{\mathrm{V}_{oc} \cdot \mathrm{I}_{sc}} = \frac{\mathrm{V}_m \cdot \mathrm{I}_m}{\mathrm{V}_{oc} \cdot \mathrm{I}_{sc}} \tag{2.2}$$

where V_{m} and J_{m} are voltage and current density at the maximum power point.

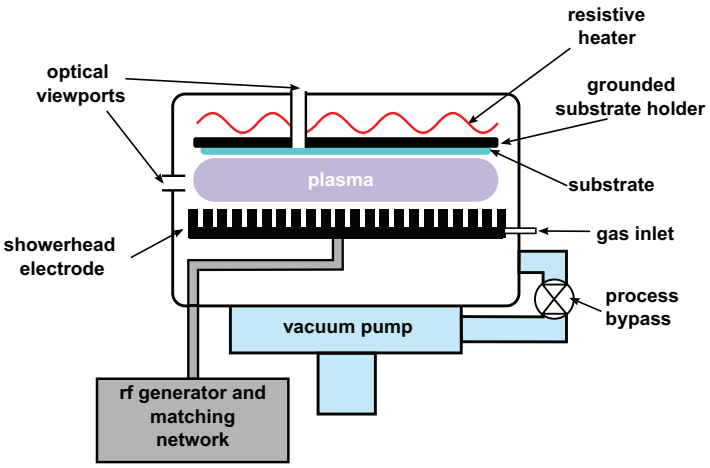

Figure 2.7: Schematic of the I1-deposition chamber. The chamber contains a powered showerhead electrode through which the process gases are fed into the deposition chamber, connected to a rf-generator via a matching network. During the deposition the pressure is controlled by a showerhead valve in the process bypass. The temperature of the holder, the substrate is mounted on, is controlled by a resistive heater. Optical view ports enable the collection of light emitted by the plasma

2.2 Sample Preparation

In this section the deposition system and the technique used to fabricate the studied samples is described.

2.2.1 The Five-Chamber Deposition System

The in-situ Raman setup is included into an existing UHV deposition system which consists of five different process chambers that are interconnected by three evacuated loading/transfer chambers. Together with transfer locks this setup enables the deposition of the doped and intrinsic layers of a solar-cell in different chambers without braking vacuum conditions. The schematics of the deposition

system is shown in Figure 2.6. Intrinsic layers are deposited in the chambers labeled I1 - I3. The chamber I3 is made from aluminum which enables experiments with fluorine etchants [46]. The I2 chamber is used for the deposition of standard layers and solar cells. Additionally the contamination of intrinsic layers by oxygen and nitrogen is studied in this chamber [47, 48]. The I1 chamber has been used for in-situ process study and control before [49].

Figure 2.7 shows a schematic drawing of the I_1 chamber. The process gases are fed in via a showerhead electrode. Hereby the uniformity of the gas composition in the volume relevant for the deposition of the layers is guaranteed. The substrate is mounted parallel to the showerhead on a grounded substrate holder. The distance (d_{el}) between the substrate and the showerhead electrode is 10 mm. The plasma is generated by applying an alternating voltage to the showerhead electrode. The output impedance of the generator and that of the deposition system is matched by a matching network. A resistive heater is used to radiatively heat the substrate. To monitor the temperature of the glass substrate (T_S) an optical feed through is included in the heater and the substrate holder. Thus it is possible to determine T_S radiatively [50].

The doped layers for solar cells are deposited in separate chambers to avoid cross contamination of the intrinsic layer with dopant atoms. The p- and n-chamber are equipped with a simple cross flow gas inlet. Vacuum conditions in all the chambers are established with a two-stage pumping system composed of a rotary and a turbo molecular pump. Hence base-pressures of less than 1×10^{-7} Torr are achieved. During the deposition of a layer the pressure is usually in the range of a few Torr. This pressure regime is realized by controlling the pressure via a butterfly-valve in the process bypass as indicated in Figure 2.7. The layers are deposited on either Corning Eagle XG glass or Zinc Oxide covered glass substrates of a size of 10×10 cm^2. Previous to each deposition a temperature equilibration step is carried out under an Argon atmosphere at 5 Torr pressure to guarantee a reproducible substrate temperature. In Table 2.1 typical parameters obtained for amorphous and microcrystalline silicon thin film solar cells deposited in the 5-Chamber deposition system are summarized. These results are obtained for solar cells of 1×1 cm^2 with a silver back back reflector.

material	V_{oc} [mV]	J_{sc} [mA/cm^2]	FF [%]	absorber thickness [μm]
a-Si:H	900	14	72	0.3
μc-Si:H	520	22	70	1.2

Table 2.1: Open-circuit voltage, short-circuit current density, fill factor, and absorber thickness of standard 1×1 cm^2 amorphous an microcrystalline silicon solar cells deposited in the 5-Chamber system on ZnO substrates with silver back reflectors.

2.2.2 Plasma-Enhanced Chemical Vapor Deposition

Growth Models Plasma enhanced chemical vapor deposition (PECVD) is a standard process used to deposit various thin film materials [51, 52, 53, 54]. In this thesis a source gas composition containing hydrogen (H_2) and silane (SiH_4) is decomposed in a parallel-plate reactor to deposit amorphous and microcrystalline silicon thin films. The decomposition of silane into the growth precursors is achieved by applying an alternating voltage of a frequency of 13.56 MHz to the powered electrode. Due to the resulting alternating field a plasma is generated between the parallel plates. The kinetic energy of the fast electrons of the plasma is large enough to decompose SiH_4. As a result neutral radicals like SiH_3, SiH_2 and SiH and ionized species like SiH^+, SiH_2^+ and SiH_3^+ are generated. The most important species present during silane plasma deposition of silicon are summarized in [55]. The radicals that contribute to the deposition –also referred to as growth precursors– diffuse towards the film surface. There a complex interplay between adsorption, desorption and secondary gas-phase reactions takes place. There are three different schools of thought concerning the growth of μc-Si:H

- The hydrogen etching model is based on the fact that there is continuous etching and redeposition of silicon during the growth of a μc-Si:H film [56, 57]. Under the assumption that a-Si:H is preferentially etched [58] predominantly microcrystalline material develops under certain process conditions.
- The second model - proposed by Matsuda et al. [59] - relates the formation of a microcrystalline phase to the hydrogen coverage of the film surface. When most of the surface sites are occupied by hydrogen atoms the diffusion

length of growth precursors, as SiH_3, on the surface is high. This promotes the formation of a crystalline phase.

- The third model suggested by Shibata et al. [60] attributes the formation of crystallites to a chemical annealing effect that takes place during deposition. In this model it is assumed that hydrogen atoms penetrate several atomic layers into the growing film. There they promote a transformation of a-Si:H into μc-Si:H which is called "network propagation reaction" or "H chemical annealing".

In conclusion hydrogen plays an important role in all the discussed growth models. According to the models the formation of the microcrystalline phase could either take place in a fraction of the layer that has already been deposited or instantaneously when the growth precursors attach to their position in the silicon network.

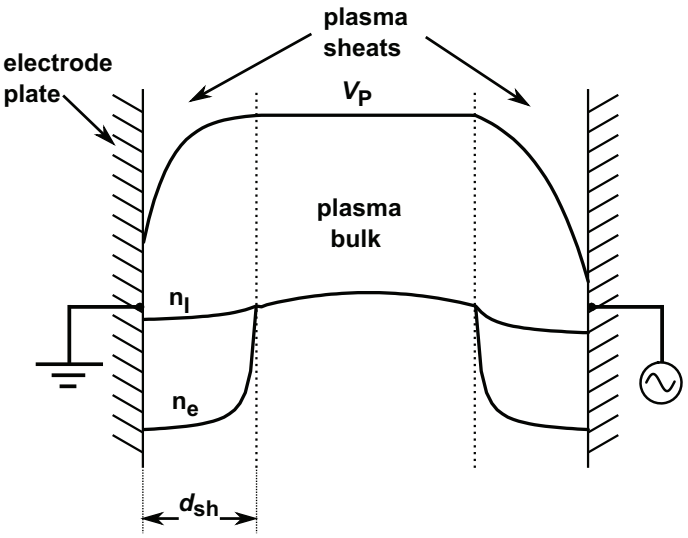

Figure 2.8: Plasma potential V_P, electron density n_e, and ion density n_i in a rf-discharge after [61]. The plasma sheaths between the plasma bulk and the electrode plates are indicated.

Electrical Properties of the Plasma The deposition of a thin film using a plasma process is governed by the electrical properties of the plasma used to decompose the source gases. Applying a rf-frequency leads to a time averaged plasma potential (V_{P}), and electron (n_{e})/ion(n_{i}) densities between the electrode plates as shown in Figure 2.8. The plasma potential is zero at the grounded electrode throughout the whole rf-cycle. At the powered electrode V_{P} is usually below zero. This asymmetry is mainly due to the difference of the areas of the grounded and the powered electrode which is especially pronounced in a small area deposition system since the for small electrode areas the electrons lost to the grounded chamber walls lead to an increase of the asymmetry of the potential.

Due to the large mass difference the electrons are much more mobile than the ions. Hence the ions are assumed as static in the case of radio frequency discharges. Accordingly more electrons than ions that are generated in the plasma are lost on the electron surface during the phase of plasma ignition. Since no net current flows in the stabilized plasma an electric field is generated in the regions close to the electrode surfaces repelling the electrons. Due to the electric field in the region close to the electrodes –also referred to as plasma sheath region– ions are accelerated towards the electrode and substrate surfaces. The width (d_{sh}) of the sheath is in the order of a few plasma debye lengths (λ_{db}) [61]

$$d_{\mathrm{sheath}} \cong \lambda_{\mathrm{db}} = \sqrt{\frac{\epsilon_0 k_{\mathrm{B}} T_e}{n_e e^2}} \tag{2.3}$$

where T_{e} is the electron temperature, n_{e} the electron density in the plasma, and ϵ_0 the electric permit

Deposition Parameters There are several deposition parameters that determine the properties of the plasma and with that the features of the growing film. The major parameters of a PECVD plasma are:

- The **deposition pressure** p. It determines the density of particles inside the reaction chamber and hence the mean free path of electron, atoms, and molecules and thus the electron energy and the energy of bombarding ions. The crystalline volume fraction decreases with increasing p at otherwise constant deposition conditions.

- The **silane concentration** (SC) describes the ratio of the silane gas-flow

to the total gas flow

$$SC = \frac{\mathrm{SiH_4}}{\mathrm{SiH_4 + H_2}}. \tag{2.4}$$

It has a direct influence on the ratio of hydrogen atoms to growth precursors. A standard way to vary the composition of thin film silicon from purely amorphous to highly crystalline is to decrease SC with the rest of the deposition conditions being constant.

- The **temperature** T of the growing film is of great importance for its properties since it determines, amongst others, the hydrogen coverage of the growing surface. The temperature (T_H) that is usually measured and controlled is that of the external heater. In the work of van den Donker *et al.* it was shown that the time resolved behavior of T_H can differ from the temperature (T_S) of the glass substrate [50]. In the present thesis a method to directly measure the vibrational temperature T_film of the growing film using Raman spectroscopy is applied.
- The **discharge power density** P influences the deposition rate (R_d) at incomplete SiH_4 depletion. At increasing SiH_4 depletion the crystalline volume fraction is determined by P. Hence the optimum crystalline volume fraction for solar cell performance can be achieved at a high R_d by simultaneously increasing P and SC. The increase of R_d is limited since the material properties are known to degrade for large input powers [36].

Standard Deposition Conditions The properties of a grown layer are determined by the deposition conditions described above. In Table 2.2 the deposition parameters applied in the 5-Chamber system for the deposition of standard μc-Si:H p-doped and intrinsic layers are summarized.

layer	p **[Torr]**	SC **[%]**	T_H **[°C]**	**P [W/cm^2]**
μc-Si:H-p	3	0.27	250	0.15
μc-Si:H-i	10	0.64	200	0.5

Table 2.2: Deposition pressure, silane concentration, heater temperature, and input power density used to deposit standard μc-Si:H p-doped and intrinsic layers at an excitation frequency of 13.56 MHz in the 5-chamber system.

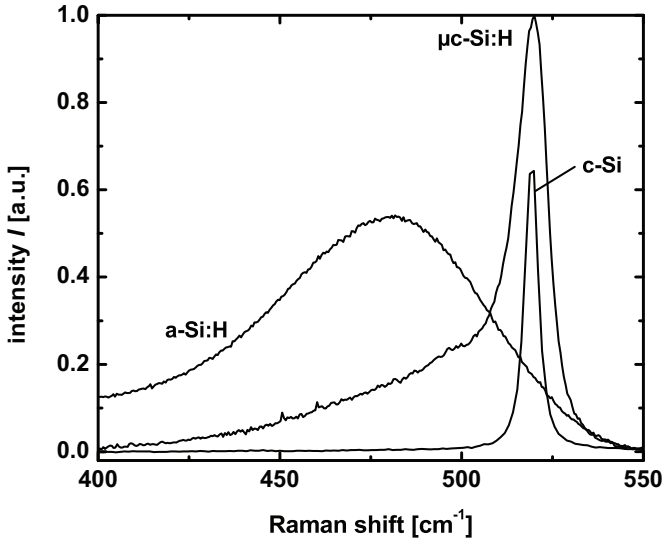

Figure 2.9: Stokes Raman shift of microcrystalline, amorphous and crystalline silicon.

2.3 Characterization

Apart from Raman spectroscopy optical emission spectroscopy and the determination of solar cell IV-characteristics will be discussed in this section as means of characterization of thin silicon films and solar cells.

2.3.1 Raman Spectroscopy

Raman Scattering in Silicon The Raman effect has been discovered in the first half of the last century [25]. It describes the inelastic scattering of light by molecules and solids. Raman spectroscopy is frequently used to measure fundamental optical and vibrational properties of solids. The theory of Raman scattering is discussed in the literature [62, 63, 64]. During the Raman scattering process a phonon is either excited (Stokes process) or annihilated (anti-Stokes process). In Figure 2.9 the first order Raman shifts of crystalline, amorphous, and microcrystalline silicon are compared. The Raman shift of c-Si at room tem-

perature is centered at 520 cm^{-1}. This corresponds to the excitation of the Γ'_{25} phonon. The strict selection rules for crystalline silicon are reflected in the small full width at half maximum (FWHM) of ~ 3.5 cm^{-1}.
The Raman spectra of μc-Si:H and a-Si:H look different. In Figure 2.9 it can be seen that the Raman shift generated by amorphous material is centered at 480 cm^{-1} and widened to a FWHM of about 70 cm^{-1}. The broadened peak is related to the relaxation of the momentum selection rules in an amorphous semiconductor. The microcrystalline Raman spectrum can be described as a combination of amorphous and crystalline contributions. Due to stress and finite grain size in μc-Si:H the peak representing the crystal contribution is often widened and shifted from the Γ'_{25} resonance in crystalline silicon [21].

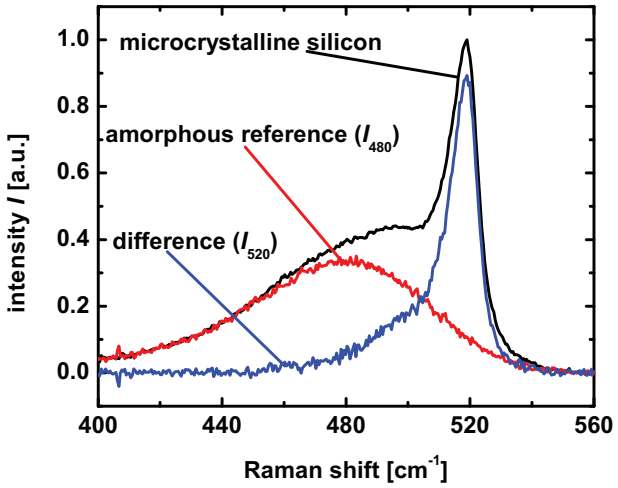

Figure 2.10: Typical Raman spectrum of a μc-Si:H film with a crystalline volume fraction of 39%. An amorphous reference spectrum is subtracted from the measurement to evaluate I_C^{RS}.

Estimation of the Crystalline Volume Fraction Raman spectroscopy is widely used to obtain a measure of the crystalline volume fraction of μc-Si:H films [21, 22, 23, 24]. An amorphous reference spectrum, of the integrated inten-

sity I_{480}, is subtracted from the original measurement to obtain the contribution (I_{520}) of the crystalline material. As seen in Figure 2.10 the intensity of the amorphous reference spectrum is fitted to minimize the intensity of the difference spectrum in the wavenumber region from 400 cm^{-1} to 440 cm^{-1}. The Raman crystalline volume fraction (I_C^{RS}) is evaluated from the ratio of the integrated areas of I_{520} and the total intensity of the signal [65]

$$I_C^{RS} = \frac{I_{520}}{I_{520} + I_{480}}. \tag{2.5}$$

It has been shown [22] that I_C^{RS} is in good agreement with the crystalline volume fraction determined from X-ray diffraction (XRD) and transmission electron microscopy (TEM) measurements. The term crystalline volume fraction will be used as an equivalent of the crystalline volume fraction obtained by Raman spectroscopy in the following.

Information Depth The volume of the layer probed by Raman spectroscopy is determined by Lambert-Beers law. Equation 2.6 describes the decrease of the initial intensity (I_0) of the probe beam by absorption in the film

$$I(d) = I_0 \cdot e^{-d \cdot \alpha(\lambda)}. \tag{2.6}$$

The absorption coefficient (α) depends on the wavelength (λ) of the light according to Figure 2.1. This effect is exploited for depth dependent measurements of I_C^{RS} using different excitation wavelengths [66].

The information depth d_{inf} of a Raman scattering experiment corresponding to a specific wavelength is defined as the thickness of a layer in which more than $\frac{2}{e}$ of the Raman shifted light is generated. The scattered light is absorbed on its way back towards the surface. Assuming similar absorption coefficients for the elastically scattered and the Raman shifted light d_{inf} is approximated as $0.5/\alpha(\lambda)$. Figure 2.11 shows d_{inf} of a-Si:H and highly crystalline (75 %) μc-Si:H as a function of the wavelength based on the absorption coefficients shown in Figure 2.1. Assuming absorption coefficients of $4 \cdot 10^{-4}$ cm^{-1} and $9 \cdot 10^{-4}$ cm^{-1} for μc-Si:H and a-Si:H at a λ of 532 nm respectively d_{inf} is approximated as 125 nm and 56 nm for these materials. When using different wavelengths for Raman scattering experiments the energy dependence of the Raman scattering cross section also has to be considered. According to Bermejo *et al.* and Grimsditch *et al.* the

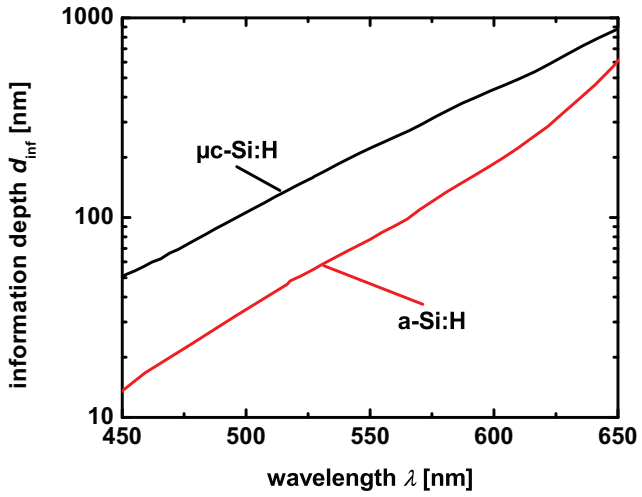

Figure 2.11: Information depth in amorphous and highly crystalline (75 %) microcrystalline silicon as a function of the wavelength of the probe light.

cross sections for both silicon configurations are almost constant for laser wavelength ranging from 480 nm to 532 nm which represents the relevant wavelengths applied during this thesis [67, 68].

Temperature Measurements using Raman Spectroscopy Figure 2.12 shows a typical Raman spectrum of crystalline silicon obtained in the spectral range from -600 cm^{-1} to 600 cm^{-1} at room temperature. The Stokes and anti-Stokes peaks are centered at 520 cm^{-1} and -520 cm^{-1}. Since phonons are bosons their occupational statistics follows the Bose-Einstein-Distribution [69]. Hence the ratio R_T of the Stokes to anti-Stokes scattering intensity is proportional to the lattice temperature (T_l)

$$\frac{R_S}{R_{aS}} \propto \frac{n(\omega_0)+1}{n(\omega_0)} \tag{2.7}$$

where $n(\omega_0)$ is the phonon occupation probability and phonon frequency ω_0. The constant of proportionality depends on the laser wavelength, and the Stokes and

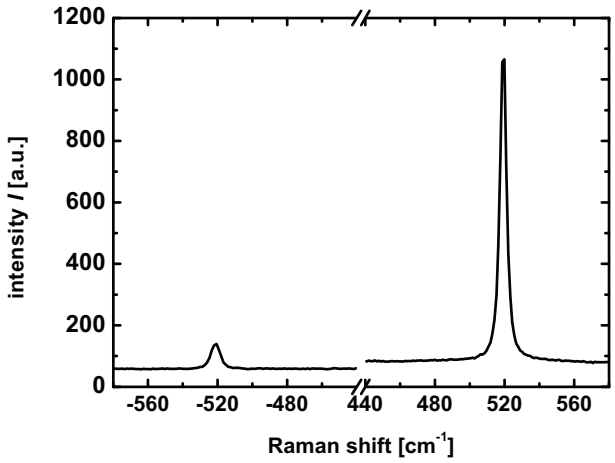

Figure 2.12: Stokes and anti-Stokes scattering of crystalline silicon at room temperature.

anti-Stokes phonon frequencies ω_L, ω_S and ω_{AS}. Also the Stokes and anti-Stokes Raman-scattering cross sections $\sigma(\omega_L, \omega_S)$ and $\sigma'(\omega_L, \omega_{AS})$ are influencing R_T. Following Lo et al. [26] the temperature dependent ratio of counting rates for Stokes-to-anti-Stokes Raman scattering is given by

$$R_{\mathrm{T}} = \frac{(\alpha_L + \alpha_{AS})\omega_s^3 \sigma(\omega_L, \omega_S)}{(\alpha_L + \alpha_S)\omega_{AS}^3 \sigma'(\omega_L, \omega_{AS})} exp(\hbar\omega_0/kT) \tag{2.8}$$

where α_L, α_{AS} and α_S are the absorption coefficients in the material for laser, anti-Stokes and Stokes radiation. For a specific laser wavelength Equation 2.8 is rewritten as

$$R_{\mathrm{T}} = C \cdot exp(\hbar\omega_0/\mathrm{k_B}T) \tag{2.9}$$

with the constant C_{Ram}. This constant only depends on the studied material and the experimental system and can be determined if the temperature of a studied film is known (see Section 6.1). For a known C_{Ram} the lattice temperature can be directly extracted from measurements of the Stokes and anti-Stokes scattering intensities.

Experimental Setup The experimental setup used for Raman spectroscopy

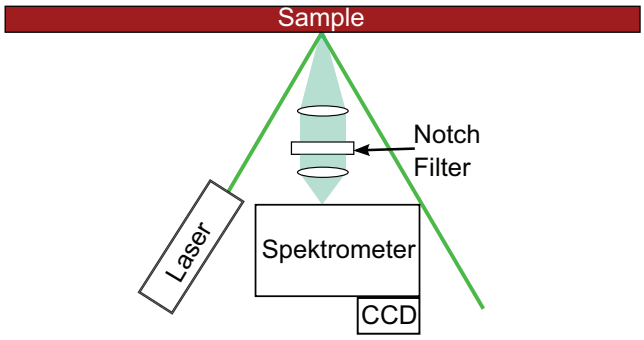

Figure 2.13: Schematics of a setup for Raman spectroscopy on thin films. The sample is illuminated by a laser. Elastically scattered light is blocked by a narrow band notch filter. The scattered light is split into its spectral parts in a spectrometer and recorded by a CCD camera.

is schematically shown in Figure 2.13. The sample is illuminated with a laser under a small angle and the scattered light is collected perpendicular to the sample by a spectrometer. Since the intensity of the inelastically scattered light is very low the laser frequency has to be blocked by a narrow band notch filter.

2.3.2 Optical Emission Spectroscopy

A common way to monitor the composition of a PECVD plasma is optical emission spectroscopy (OES). Due to the simple experimental setup the equipment for OES can be readily added to existing deposition equipment. The view port that enables optical access to the plasma region is shown in Figure 2.7. From there the light is coupled into a spectrometer e.g. by a glass fiber. There it is decomposed into its spectral contributions and their intensity is determined. A typical spectrum of the PECVD plasma emission in a wavelength region from 200 nm to 800 nm is shown in Figure 2.14. The plasma emission is composed of individual lines indicating electronic transitions in atoms e.g. the H_β line at 486 nm and electronic, vibrational, and rotational transitions of the plasma molecules that result in molecular bands.

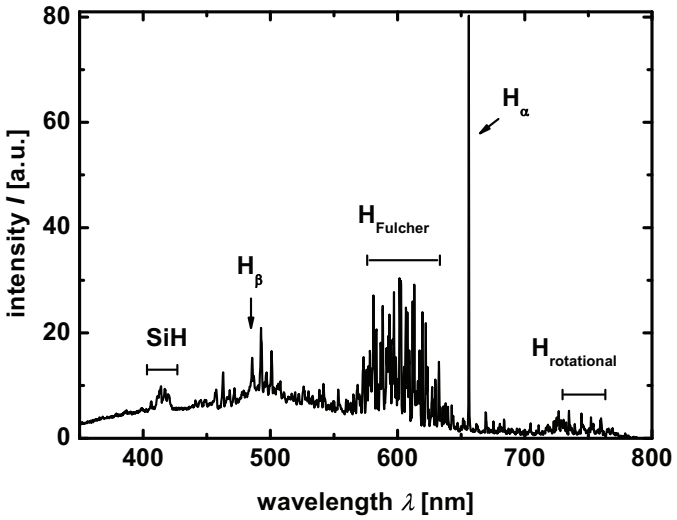

Figure 2.14: Emission of a typical plasma used for the deposition of microcrystaline silicon. Characteristic atomic hydrogen lines and molecular bands are indicated.

2.3.3 Solar Cell Characterization

The most important parameters of a solar cell can be extracted from measurements of the I-V-characteristics under illumination. These measurements are performed under standard conditions using a spectrum fitted to an AM 1.5 reference and a stabilized temperature of 25°C . Figure 2.5 shows a typical I-V-characteristics of a solar cell. From this curve the maximal output power P_{m} of the solar cell is determined as indicated in the figure. Under the assumption of the superposition principle for the dark current of an ideal diode and the photo current (I_{ph}) generated under illumination the diode equation of a solar cell is approximated as [70]

$$I(V) = I_0(\mathrm{e}^{\frac{qV}{k_B T}} - 1) - I_{\mathrm{ph}} \tag{2.10}$$

where I_0 is the dark saturation current, T the temperature, q the elementary charge and k_B Boltzmann's constant factor.

3 Experimental Realization of an In-Situ Raman Setup Inside a PECVD Chamber

The integration of an in-situ Raman setup into a conventional parallel plate PECVD system requires substantial modification. In this chapter the requirements for an in-situ Raman experiment regarding the optical components and the deposition system are discussed. The impact of the setup on growing films is studied. An experimental system that combines optimum optical properties with a minimal impact on growing films is developed.

3.1 Experimental Requirements and Restrictions

In-situ Raman spectroscopy during the growth of μc-Si:H has been reported previously during remote plasma deposition [19]. When integrating such a setup into a parallel plate PECVD system additional challenges arise. The major difference with regards to in-situ Raman spectroscopy between remote and parallel plate PECVD is the restricted optical access in the latter case. Hence extensive modifications of the deposition system are necessary to enable in-situ Raman spectroscopy. Special care has to be taken to avoid an impact of these modifications on the layer growth. The absorption of the laser light used for the scattering experiments induces a temperature increase. The heating has to be minimized since the film temperature has an impact on the properties of a growing film. A preliminary study focused on the choice of the optical components and the influence of the laser parameters on the heating of a film has been carried out by Köhler [71].

The main demands for an in-situ Raman setup inside a parallel plate PECVD system are:

- **Adequate temporal resolution**. For a deposition with an excitation frequency of 13.56 MHz the typical deposition rate of μc-Si:H films is 5 Å/s. The deposition rate can be increased at 13.56 MHz but the material properties are known to deteriorate for rates that are larger than 10 Å/s at this excitation frequency [72]. Hence for an in-situ experiment a temporal resolution in the order of 10 s is sufficient since at growth rates of 5 Å/s a layer with a maximum thickness of 10 nm will grow during one measurement interval. Raman spectroscopy is used to obtain information about the bulk of a layer. Hence a smaller temporal resolution will not result in additional information since then the contribution of the fraction of the layer that is deposited during one measurement interval to the overall signal will be very small.

- **Good signal-to-noise-ratio**. It was found by Köhler that a minimum signal-to-noise ratio of 5 is sufficient to evaluate the crystalline volume fraction [71]. He also discussed the Raman efficiency of microcrystalline silicon that describes the ratio between illuminated and Raman shifted photons was determined to be as low as 10^{-11}. When performing Raman measurements during PECVD the light emitted by the plasma will be part of the recorded spectra. Together with the demand for short integration times requested by the high temporal resolution the large background signal presents a challenge to obtain the necessary signal-to-noise ratio.

- **Durability**. The main challenge regarding the durability of an in-situ Raman setup is that in a PECVD environment all the components with a direct line of sight to the plasma zone are coated. This is due to neutral radicals –like SiH_3– generated in the plasma. Some of the radical lifetimes are large enough to enable them to leave the central regions of the plasma. Hence these radicals contribute to the desired growth of layer but also to the coating of optical components which leads to a reduction of the collected intensity during deposition.

- **Homogeneous deposition**. When performing in-situ measurements it is important that the obtained results are valid for the whole active area of a

solar cell. Hence it has to be made sure that no inhomogeneities are caused in the growing film by the measurement setup itself. These requirements demand a careful construction of the electrode. Disturbances in an electrode surface above a certain size are expected to cause inhomogeneities in the electric field. These will lead to inhomogeneous layers if no precautions are taken. Furthermore, state-of-the-art parallel plate PECVD reactors are typically equipped with showerhead electrodes that guarantee a homogeneous gas distribution in the plasma volume. The influence of the in-situ setup on the gas distribution has to be minimized.

- **Minimal heating**. The laser radiation used to record the Raman spectra can lead to a considerable increase of the film temperature. Since the temperature of a growing film is known to have a large impact on its optical and electrical properties the laser induced temperature increase has to be minimized in an in-situ Raman setup.

3.2 Integration of a Raman Setup into a Parallel-Plate PECVD Reactor

In this section the integration of an in-situ Raman setup into a PECVD reactor and the optical path used to guide the light into the deposition chamber are described. Methods to maximize the obtainable Raman spectra and to remove the signal originating from the PECVD plasma are discussed.

3.2.1 Optical Path of the In-situ Setup

The principle of Raman spectroscopy requires the illumination of the observed sample by a laser and the collection of the scattered light. This can be realized in two configurations. As illustrated in Figure 2.13 it is possible to illuminate the sample under a small angle and collect the scattered light perpendicular to the surface. The advantage of this configuration –which is referred to as near backscattering setup– is that very little of the elastically scattered light is part of the analyzed radiation.

In another configuration the illumination of the sample takes place by the

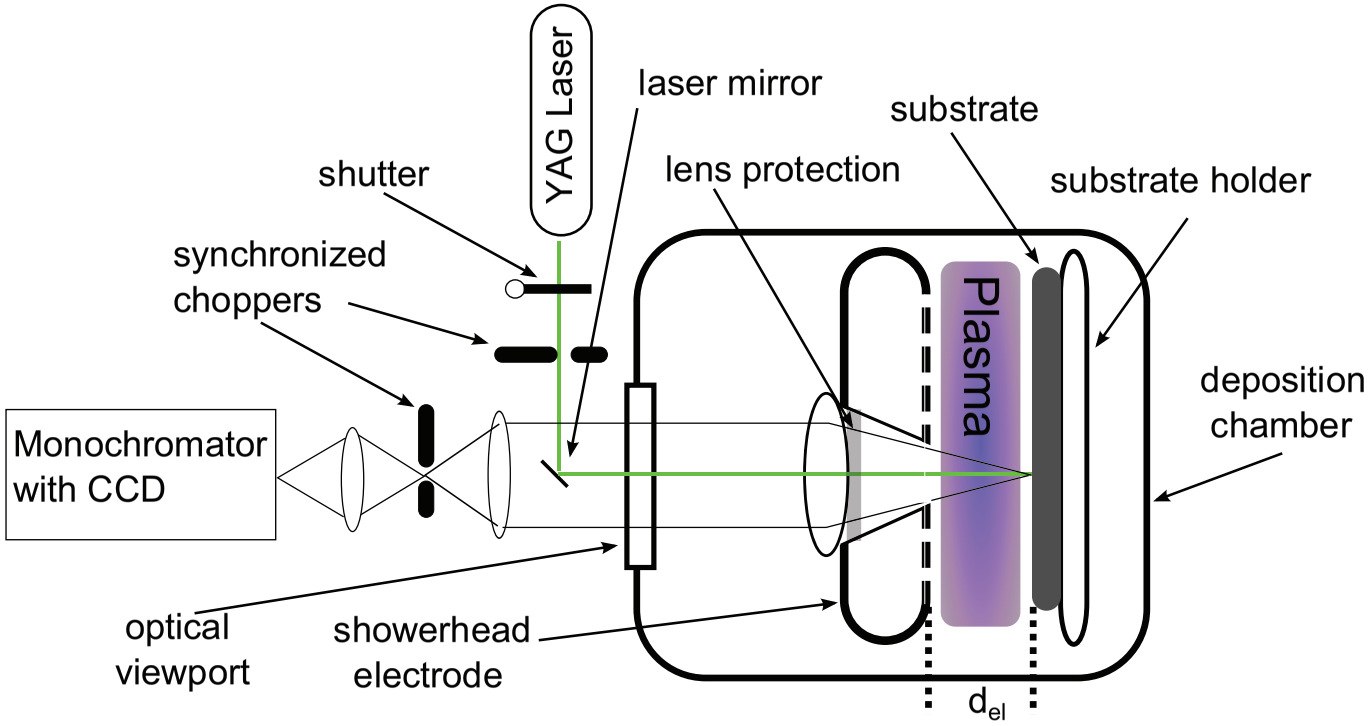

Figure 3.1: Integration of a Raman setup into a PECVD chamber. The laser radiation is directed perpendicularly onto the sample, which is positioned at a distance d_{el} to the electrode, using the same path as the collected light. The recording of the Raman spectra is synchronized to the laser pulses by rotating chopper wheels. The laser light is blocked by a shutter to record background spectra. A lens protection that can be readily removed prevents a coating of the optics

Laser Type	Power [mW]	Beam diameter [μm]	Spectral linewidth
Cobolt Samba	1000	700	< 1 MHz

Table 3.1: Type, output power, beam diameter and linewidth of the laser applied for the in-situ measurements.

same optical path as the collection of the scattered light. This configuration – which is shown in Figure 3.1– was chosen for the in-situ Raman experiment due to several reasons:

On the one hand this setup can be realized more compact. The fact that the in-situ Raman setup will be integrated in an existing PECVD chamber inflicts strict limitations of the available space. On the other hand only one feed through is needed in the electrode surface for illumination and collection. Hence the constructive effort and the disturbance of the plasma is minimal. The near backscattering configuration would require more intensive modifications of the PECVD reactor of which more than one optical feed through would be particularly complex.

The drawback of the selected configuration is that more of the elastically scattered light is collected. The intensity of this light is reduced far enough to enable Raman measurements by including two notch filters into the optical path.

The setup shown in Figure 3.1 is also more flexible with regards to the electrode distance. The lens simply has to be adjusted vertically after a change of d_{el} to keep the focus of the laser beam on the substrate.

A 532 nm Neodym YAG solid state laser with a very narrow line width of less than 1 MHz is used for the Raman experiments. The specifications of the laser are summarized in Table 3.1. A laser with a shorter wavelength would have the advantage of a smaller information depth. Unfortunately lasers with the required parameters like output power and line width could not be made available so far.

3.2.2 Optimizing the Optical Components

To perform Raman measurements during PECVD the optical components have to be optimized. Due to a desired temporal resolution in the range of some ten seconds the expected Raman signal is rather low. Hence all the applied compo-

nents like mirrors and lenses are selected for optimum performance at the used laser wavelength. As mentioned in Section 3.1 the coating of the optics by radicals generated in the PECVD process has to be minimized. As shown in Figure 3.1 this is realized by a lens protection that can be readily replaced. Removing and cleaning of the lens would require the optical path to be readjusted. Since the covering of the lens protection during deposition continuously reduces the collected Raman signal the optical components are situated as far from the plasma zone as possible.

Due to the reduction of the signal during deposition the number of measurements possible before cleaning the reactor is limited. To enable preconditioning of the chamber without coating the optics the feed trough is covered with a metal plates. Using a magnet this cover is removed before the in-situ measurements without breaking vacuum conditions.

As seen in Figure 3.1 and in more detail in Figure 3.4 the feed through is constructed with a conical shape. Due to this layout the optical acceptance angle used to collect the scattered radiation is enlarged with a relatively small opening on the side facing the plasma volume. This leads to a reduction of the impact of the feed through on deposition homogeneity with a simultaneous optimization of the optical properties.

3.2.3 Reducing the Plasma Contribution

Apart from the problem of a coating of the optics, the plasma also introduces a strong background signal. Figure 3.2 shows the plasma emission in the spectral region relevant for Raman spectroscopy with 532 nm laser radiation. It was recorded with the in-situ Raman setup during the deposition of a standard μc-Si:H intrinsic layer. In addition to a continuous background molecular lines are distinguished in the spectrum. Since these plasma lines will also be present during an in-situ Raman measurement the Raman signal has to be large enough to be separated from the Plasma contribution.

By the shutter shown in Figure 3.1 the laser radiation is blocked to record the plasma background spectrum. To enable the subtraction of the plasma background the plasma emission has to be constant while the Raman and the background spectrum is recorded. Apart from the initial ignition this assumption is

valid for integration times in the order of 1 s [73, 74].

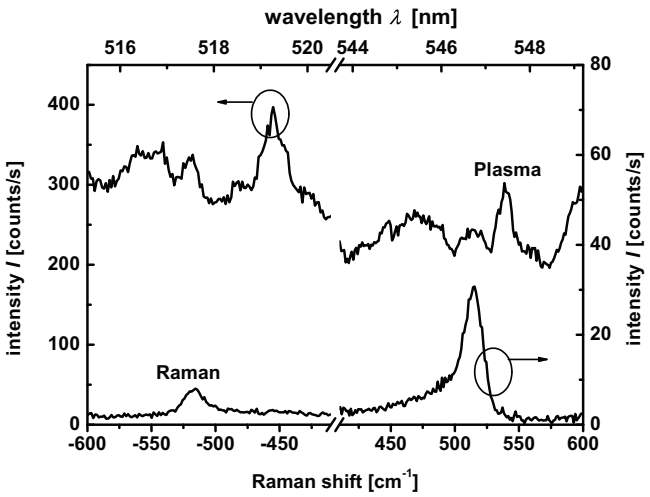

Figure 3.2: Emission of a hydrogen plasma in the spectral region that is important for the Raman shift together with an in-situ Raman measurement at a wavelength of 532 nm from which the Plasma contribution has been subtracted.

3.2.4 Maximizing the Signal-to-Noise Ratio

As mentioned above the Raman efficiencies of amorphous and microcrystalline silicon are very low. Hence high laser powers are applied to generate Raman signals with an intensity comparable to that of the plasma radiation. Since high laser powers lead to a heating and eventually a crystallization of silicon thin films [75], the laser light is pulsed to allow the film to cool down between two pulses. If the pulse is short enough the laser power in one pulse is relatively high and therewith the ratio of Raman light to plasma emission is improved with simultaneously reducing the amount of energy transfered to the film. This effect is studied in detail in Section 3.5. The pulsing of the laser radiation is realized with a chopper between the laser and the illuminated substrate. To guarantee that light only enters the spectrometer when the sample is illuminated the laser

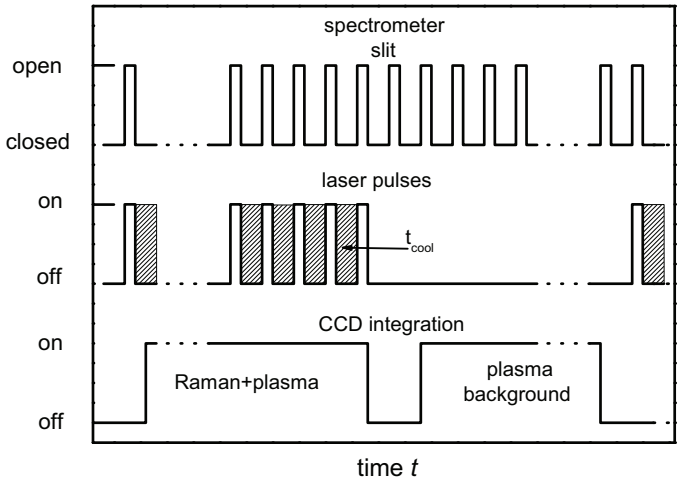

Figure 3.3: Timely course of the optical path leading to the spectrometer, the laser light and the CCD integration time during a measurement. A Plasma background spectrum with the same exposure time as the Raman spectrum is recorded during the phase with no laser illumination. During illumination of the sample it is guaranteed that light only enters the spectrometer during a laser pulse. The layer cools down between pulses in a time t_{cool}.

pulses are synchronized with a second chopper in front of the spectrometer. With this configuration no plasma background radiation is recorded during the time in which the sample is not illuminated by the laser. Due to the thereby enabled longer integration times of the CCD camera the contribution of the read-out-noise is strongly reduced when compared to measurements of single pulses.

Both of the choppers can rotate with a frequency of up to about 100 Hz. Since every chopper has 5 slits pulse frequencies up to 500 Hz are possible. The width of the pulses is adjusted by narrowing or widening of the chopper slits. By simultaneously changing the frequency of the coppers the pulse and cooling time (t_{cool}) between two pulses can hence be controlled independently. The timely course of such a measurement is shown in Figure 3.3.

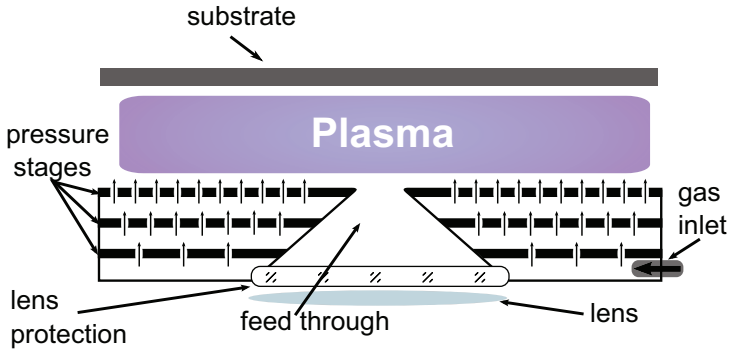

Figure 3.4: Schematic drawing of a showerhead with a conical opening. The gas is distributed homogeneously with the help of pressure stages. A lens protection which can be readily removed and cleaned prevents a coating of the lens by silicon radicals.

3.3 Integration of a Raman Setup into a Showerhead Electrode

To guarantee a homogeneous deposition of microcrystalline silicon a showerhead electrode is implemented in the deposition system. One way to realize a gas showerhead is to guide the source gases through several pressure stages. Without the optical feed through and therewith closed pressure stages Figure 3.4 would represent the standard showerhead electrode used in the 5 chamber deposition system. Using this setup a continuous decrease of the pressure from the gas-inlet to the process chamber is realized. When integrating an optical feed through the pressure gradient has to stay unaffected to avoid disturbances of the gas distribution. Additionally the arrangement of showerhead holes on the top plate has to stay close to the standard configuration to sustain the homogeneity of the gas composition. Due to the layout of the original showerhead it was possible to fulfill these prerequisites with minor modifications of the showerhead electrode.

The feed through is positioned in an area without showerhead holes in the three pressure stages. Due to the distribution of the holes on the plate facing

the plasma the maximal diameter of the opening in this plate is limited to about 10 mm. With this diameter the number of showerhead holes per area, their position and accordingly the gas distribution is not changed.

3.4 Electrical Shielding of the Feed Through

A feed through integrated into a showerhead electrode that is large enough to enable Raman spectroscopy is expected to deteriorate the homogeneity of deposited films. In this section the impact of the feed through on layer growth at different deposition conditions is studied. Electrical shields to reduce the effect of the feed through are developed [76].

3.4.1 Plasmas Inside a Cavity

When an opening with a diameter (d_{op}) above a specific size is integrated into a PECVD electrode this opening is expected to cause inhomogeneities in the plasma and hence the deposited films. Standard thin-film silicon depositions performed with conventional showerhead electrodes do not suffer from inhomogeneities caused by the holes distributing the gases. Typically the diameter of this type of holes is smaller than 1 mm. The length scale on which openings begin to influence the properties of a plasma is the debye length λ_{db}:

As mentioned in Section 2.2.2 the width of the plasma sheath is in the order of a few λ_{db}. Figure 3.5 shows a plasma inside a cavity with a diameter d_{op}. In a rf-discharge the cavity is filled with the plasma bulk of a thickness d_{pl} and the plasma sheaths of a thickness d_{sh}. If the diameter of the cavity is smaller than twice d_{sh} it is not possible for a plasma to ignite since the plasma sheaths would extend over its full diameter. The two experimental parameters determining λ_{db} are the electron temperature T_{e} and the electron density n_{e}. In Reference [77] the electron temperature for silane hydrogen plasmas with pressures above 2 mbar is found to be roughly 0.8 eV. However, this value is determined for very high frequency excitation with 60 MHz. Since T_{e} is expected to decrease with increasing frequency [78, 79] 0.8 eV is considered as a lower limit for T_{e} in a 13.56 MHz Plasma. Amanatides *et al.* have published data for n_{e} at 13.56 MHz [80]. They

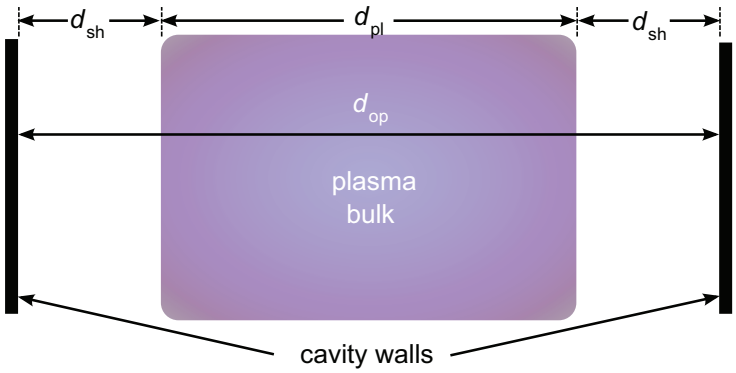

Figure 3.5: Schematic drawing of a plasma inside a cavity showing the width of the sheath (d_{sh}), the plasma bulk width (d_{pl}) and the diameter of the cavity.

estimate the space averaged electron density to be 0.7×10^8 cm^{-3}. With these parameters the diameter d_{inh} above which a discontinuity in an electrode surface can cause inhomogeneities at standard μc-Si:H deposition conditions is estimated to be $d_{inh} \sim 0.8$ mm.

As mentioned above the opening shown in Figure 3.4 has a diameter of 10 mm at the side facing the deposited film. Hence inhomogeneities are present in a film deposited without an electrical shielding of the feed through at standard deposition conditions.

3.4.2 Solar Cells in Different Growth Regimes

Due to the dependence of the plasma parameters on the deposition conditions the impact of the feed through on film homogeneity is expected to vary in different growth regimes. Hence layers with a standard deposition rate of 5 Å/s were deposited under different deposition conditions. Optimum absorber material was developed at pressures of 6, 10 and 18 Torr by depositing a series of samples at each pressure with variations of the silane concentration. The optimum deposition conditions for absorber layers deposited at a pressure of 10 Torr are described in Table 2.2.

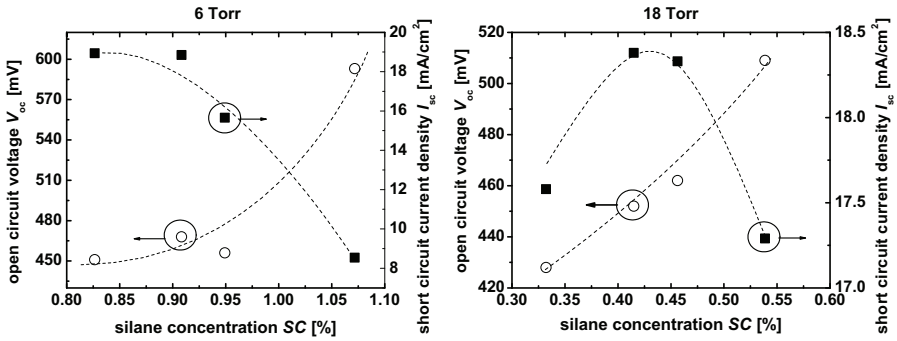

Figure 3.6: Short-circuit current density and open-circuit voltage for solar cells deposited at pressures of 6 Torr and 18 Torr with various silane concentrations.

deposition pressure [Torr]	**power density** $[W/\mathrm{cm}^2]$	**silane concentration [%]**
6	0.4	0.8 - 1.1
10	0.5	0.6 - 0.7
18	0.8	0.3 - 0.6

Table 3.2: Deposition pressure, power density and silane concentration used to deposit solar cells at a growth rate of 5 Å/s

Figure 3.6 shows short-circuit current density and open-circuit voltage of solar cells at deposition pressures of 6 Torr and 18 Torr as a function of the silane concentration. An optimum of performance is found for intermediate silane concentrations. This is attributed to an optimum in crystalline volume fraction [20]. To obtain growth rates of roughly 5 Ås in each pressure regime the input power was adjusted [54]. The input power and other important process parameters used in the different regimes are summarized in Table 3.2. The optimized intrinsic layers obtained with these deposition conditions were chosen as examples for the further study of inhomogeneities caused by the optical feed through.

3.4.3 Homogeneity without Electrical Shields

To study the impact of the feed through without an applied electrical shield on film homogeneity layer were deposited using the novel electrode and applying the optimized parameters described above. Spatially resolved measurements of the film thickness and the crystalline volume fraction were carried out. In Figure 3.7 a) spatially resolved measurements of the deviation of the thickness to the maximum d_{max} opposite the feed-through are shown for pressures of 6, 10 and 18 Torr. Figure 3.7 a) shows that the thickness of the layer is larger in the areas opposite of the feed through for pressures of 6 Torr and 10 Torr. For a pressure of 18 Torr no impact of the opening on the homogeneity of the film thickness is shown in the figure.

The trend of increasing homogeneity with an increase of the deposition pressure is also observed in the spatially resolved measurements of $I_{\mathrm{C}}^{\mathrm{RS}}$ –that was measured ex-situ– shown in Figure 3.7 b). In this figure the difference of the crystalline volume fraction to that opposite the feed through in the electrode surface is shown. The crystalline volume fraction is minimal in the area opposite the feed trough. At the center of the inhomogeneity the Raman spectra indicate an almost completely amorphous film for the for a deposition pressure of 6 Torr. The impact of the feed through on the $I_{\mathrm{C}}^{\mathrm{RS}}$ of the layers deposited at 10 Torr and 18 Torr is smaller. In these measurements the gradient of $I_{\mathrm{C}}^{\mathrm{RS}}$ towards positive values of the y-position is due to the proximity of the electrode edge which is situated at y = 22 mm.

A possible explanation for increased film thickness opposite of the feed-through is a deformation of the plasma bulk. This could lead to a larger plasma volume and an increased generation of radicals that results in a thicker layer. Another effect that could play a role is the increase of the electrical field at sharp edges. When looking at Figure 3.4 it could be suspected that the relatively sharp edges at the rim of the feed through could lead to an enhancement of the electrical field. This could result in a larger fraction of decomposed SiH_4 molecules. The increased mean free path of radicals at low pressure conditions would then explain that the impact of the feed-through is more pronounced for low deposition pressures.

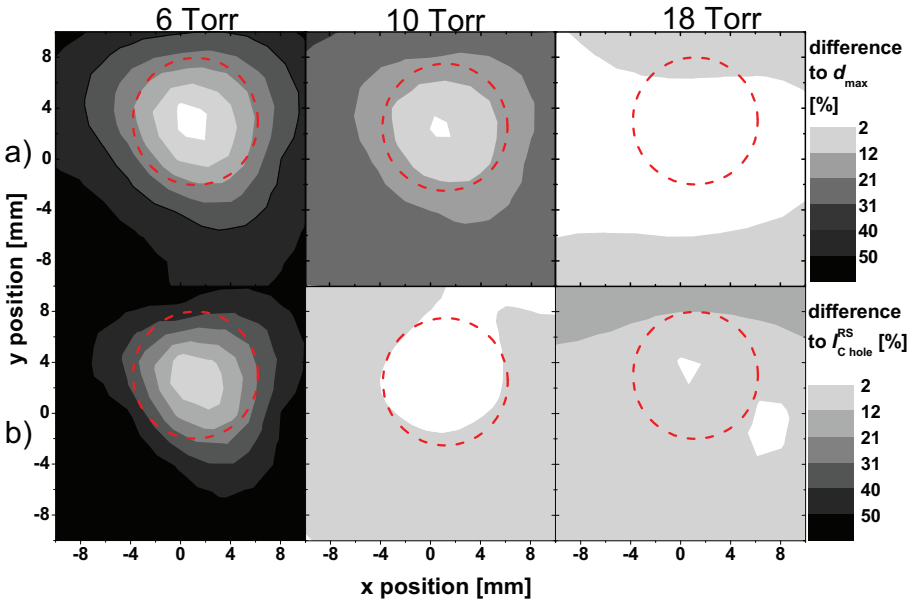

Figure 3.7: Scans of the film homogeneity opposite of the feed through at different deposition pressures without a shield covering the opening in the electrode surface.
a) Deviation of the measured thickness of films deposited at various pressures from the thickness opposite the feed through.
b)Difference of the ex-situ measured crystalline volume fraction to that measured directly opposite the feed through. The position and size of the feed-through is indicated by the dotted lines.

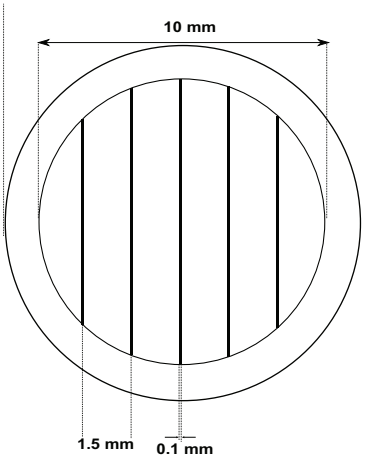

Figure 3.8: Schematic drawing of a 5 line grid used to shield the optical feed-through.

3.4.4 Shielding the Feed Through with Metallic Grids

To attenuate the inhomogeneities of the deposited films the disturbances of the plasma introduced by the penetrated electrode surface have to be minimized. This is realized by covering the feed through with metallic grids. If the distance (d_{grid}) between the individual grid lines is short enough it is not possible for a plasma to ignite between the lines as described above (Figure 3.5). To guarantee a minimal disturbance of the layer growth independent of the growth regime d_{grid} should be as small as possible to provide a shielding of the feed through at various debye lengths. This requirement collides with the demand for a high transparency of the shield that is necessary to obtain high Raman signal intensities.

To study the effect of d_{grid} on the layer homogeneity grids with a d_{grid} of 0.8 mm, 1.5 mm and 3.3 mm corresponding to 2, 5 and 10 lines at 10 mm diameter of the opening in the electrode plate were manufactured. Figure 3.8 shows an example of a 5 line grid. As seen in the Figure the width of the individual grid lines is 0.1 mm. Hence the area covered by non-transparent material is relatively small and the signal loss due to shading is reduced. In Figure 3.9 a) the inhomogeneity in film thickness at different deposition pressures is shown for

a metallic grid with 10 lines. The difference to the maximum thickness shows a much less pronounced image of the feed through on the film for pressures of 6 Torr and 10 Torr when compared to Figure 3.9. In the low pressure regime the impact of the feed through is still visible when the grid is applied but the magnitude of the thickness deviation is almost halved. In the 18 Torr regime no further improvement was possible since the layer deposited without a metallic shield did not show any influence of the feed through on its homogeneity beforehand.

Figure 3.9 b) shows mappings of the deviation of the I_C^{RS}, determined ex-situ, from that measured opposite of the feed through. A difference to the results obtained without a shield is that with the 10 line grid the crystalline volume fraction opposite of the feed through is slightly increased when compared to the rest of the layer. Also the magnitude of the deviation is much less pronounced for the layer deposited at 6 Torr. An image of the feed-through is observed in the Raman mappings on the layer deposited at 10 Torr.

In Figure 3.10 the homogeneity of the crystalline volume fraction, measured ex-situ and the thickness of films deposited at 10 Torr and 18 Torr is compared. Results obtained from films deposited at 6 Torr are not shown in the figure since no sufficient homogeneity is obtained in this deposition regime with the studied grids. In Figure 3.10 a) the average deviation of I_C^{RS} from that opposite of the hole is shown. For a deposition pressure of 10 Torr the impact of the feed through on I_C^{RS} seems to reach its maximum for a grid with 2 lines and decreases again. For the 10 line shielding the homogeneity of the layers deposited at 10 Torr and 18 Torr are similar. Not much improvement is expected if the density of lines is increased further.

In Figure 3.10 b) the standard deviation of the difference to d_{max} is shown. A reduction of the inhomogeneity is observed for a deposition pressure of 10 Torr. In the 18 Torr growth regime no change of the homogeneity in thickness is visible with increasing number of grid lines.

For a grid with 10 lines the homogeneity of the film thickness as well as that of I_C^{RS} is drastically improved at deposition pressures of 10 Torr and 18 Torr. Raman spectra measured with and without this grid show that the intensity of the scattered light is reduced by roughly 15 % when compared to an unshielded feed through. A further increase of the line density is expected to result in minor improvements of the homogeneity at a simultaneous decrease of the intensity of

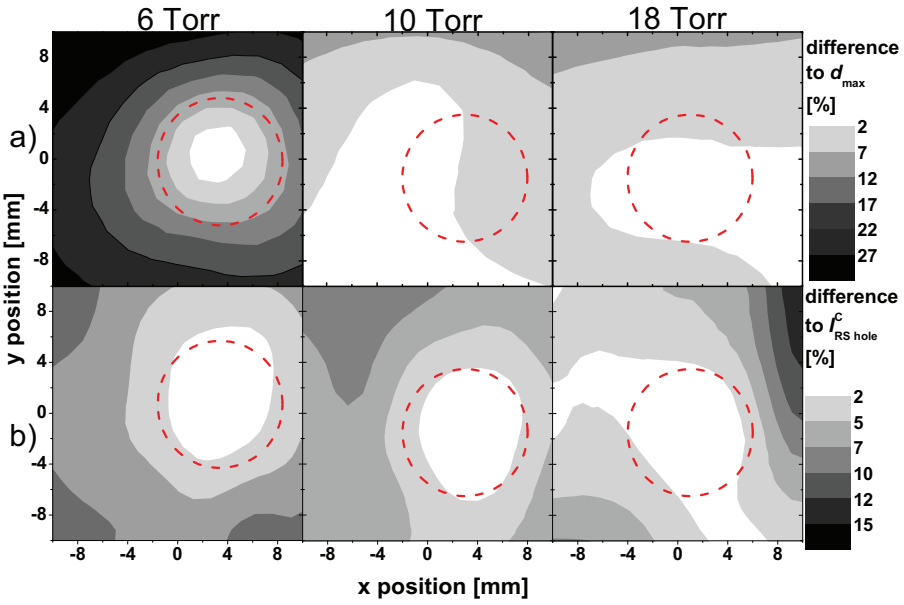

Figure 3.9: Scans of the film homogeneity opposite the feed through at different deposition pressures. The opening in the electrode surface is covered by a metallic grid with 10 grid lines.
a) Deviation of the measured thickness of films deposited at various pressures from the thickness opposite the feed through.
b) Difference of the ex-situ measured crystalline volume fraction to that measured directly opposite of the feed through. The position and size of the feed through is indicated by the dotted lines.

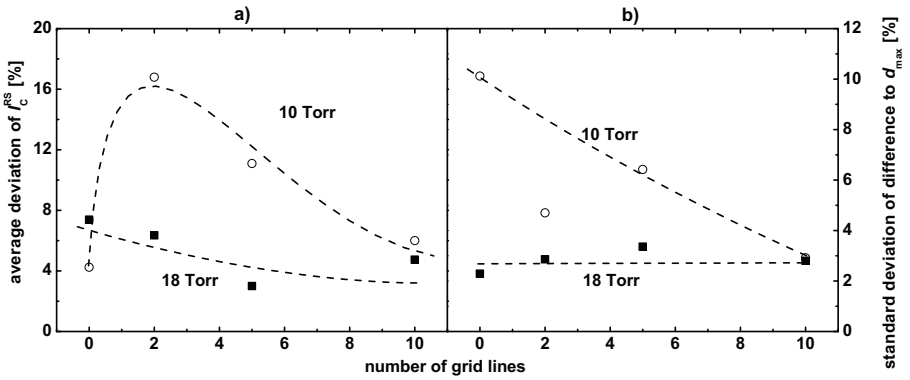

Figure 3.10: a) Average deviation of the crystalline volume fraction to the $I_{\mathrm{C}}^{\mathrm{RS}}$ opposite of the feed through for deposition pressures of 10 and 18 Torr.
b) Standard deviation of the difference in film thickness to the thickness opposite of the feed-through for deposition pressures of 10 and 18 Torr.

the Raman spectra. Hence the 10 line grid was selected for in-situ measurements that are performed at deposition pressures of 10 Torr and above.

3.5 Laser Induced Heating

The absorption of radiation in a solid is alway accompanied by an increase of temperature. When performing in-situ Raman spectroscopy this means that special care has to be taken to minimize the temperature increase due to the laser light. This is due to the fact that the temperature is known to be an important process parameter. A reduction of the temperature increase and a maximization of the emitted Raman signal are requirements that are mutually excluding each other on the first glance. An increase of the Raman signal per time unit is achieved straight forward by increasing the number of photons used to illuminate the sample. If the size of the laser spot is kept constant the energy per unit area increases in this case. Hence the temperature increase of the layer by absorption is larger. A straight forward way to circumvent this problem is to

expand the laser spot on the sample to decrease the energy density. As mentioned in Section 3.2 another way to limit the temperature increase is to pulse the laser light and thereby minimize the dissipated energy at large peak Raman intensities.

3.5.1 Experimental Minimization of the Laser Induced Temperature Increase

In an in-situ experiment the temperature increase ΔT has to be kept as low as possible. This results in demanding restrictions for the experimental parameters. For ex-situ Raman measurements it might be sufficient to limit ΔT to a value T_{crys} that prevents laser induced crystallization. Since the temperature is determining the optical, structural and electronic properties of a growing μc-Si:H layer ΔT has to be minimized in an in-situ experiment.

Hence T_{crys} is determined in a first estimation as the upper limit of the temperature increase. By choosing an experimental setup that makes sure that ΔT is much smaller than the determined T_{crys} the influence of the Raman measurements on the growing film is minimized. Since the laser induced temperature increase can not be completely avoided it has to be made sure that the crystalline volume fraction of a growing layer is unaffected by the laser radiation. The results obtained with the in-situ setup only allow conclusions about the undisturbed growth if it is made sure that the influence of the laser heating is minimal. To determine the impact of the in-situ measurements on the layer growth, in-situ data is compared to measurements obtained ex-situ at a position of the sample that is not affected by the Raman measurements, in Section 4.3.

When considering the two material types a-Si:H and μc-Si:H it is expected that at 532 nm radiation ΔT will be larger for an amorphous film. The thermal conductivity of microcrystalline silicon lies somewhere between that of amorphous and polycrystalline silicon which is –in the studied temperature regime– larger than that of a-Si:H [81, 82]. Hence the higher absorption coefficient of a-Si:H will result in a higher ΔT due to the slower dissipation of the absorbed heat. The measurements presented in this section were carried out under vacuum conditions at room temperature. Hence the ΔT that induces crystallization represents an upper limit since at the elevated temperatures during μc-Si:H deposition it is expected that less laser energy is necessary to induce the crystallization of a

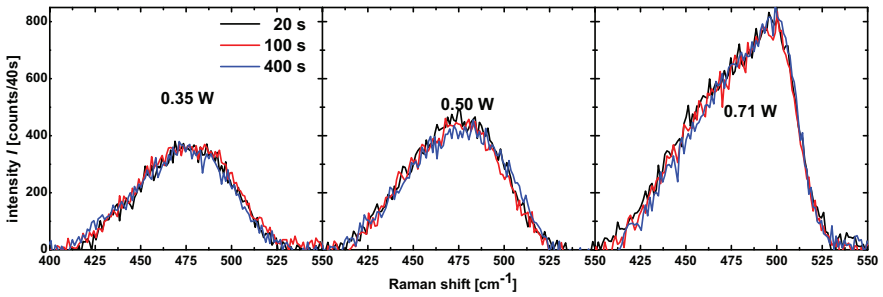

Figure 3.11: Raman spectra of initially amorphous films recorded with different laser powers. The spectra were recorded after 20 s, 100 s and 400 s of pulsed illumination.

layer.

Influence of the laser power on the film temperature To regulate the power of the laser beam gray filters with different optical densities were applied. The optical density is defined as

$$I = I_0 \times 10^{-OD} \tag{3.1}$$

where I_0 is the initial intensity of the light. This means that a filter with an optical density of 0.3 reduces the intensity of the incident light by 50 %. Additional to attenuating the intensity a grey filter also expands the beam slightly. Due to intensity losses caused by the optical components used to guide the laser light towards the sample the power at the film is reduced compared to the laser output. A power of 320 mW without an OD filter was determined at the sample with the help of an optical power meter. This means that almost 70 % of the laser power is lost by reflection and absorption on the way towards the sample.

To study the influence of the laser power on the film temperature Raman measurements on a 1 μm thick amorphous silicon layer were carried out. A pulse length of 65 μs was set by adjusting the width of the chopper slits. The chopper was rotating with a frequency of 85 Hz leading to a duty cycle of roughly 3 %. An individual spectrum is recored by accumulating 5 spectra for one second. The applied measurement parameters are summarized in Table 3.3. In Figure 3.11 the Raman spectra of initially amorphous layers recorded after pulsed illumination for 20, 100 and 400 s at laser powers of 0.35, 0.5 and 0.71 W are shown. For

pulse length [μs]	**optical density**	**output power [W]**	**power at sample [mW]**
65	0	1	320
65	0.15	0.71	227
65	0.3	0.50	160
65	0.45	0.35	112

Table 3.3: Pulse length and optical density of the filter that diminishes the laser power, resulting output power and power at the sample. These parameters were used to study the influence of the laser power on the temperature increase of a film.

output powers below 0.71 W no change in the Raman spectra is observed. For a larger laser power a contribution of the crystalline phase is observed for all of the spectra.

This means that the crystallization temperature was not exceeded for laser powers below 0.71 W. Even after a long time the spectra only contain an amorphous contribution. Hence the duty cycle of the laser radiation is low enough to allow the sample to cool down between two pulses since otherwise the crystallization would take place after some time.

For a laser power of 0.71 W the dissipated energy during one measurement interval is high enough to partially crystallize the sample. After the first measurement no further increase of the crystalline volume fraction is observed. This could be due to fact that the partially microcrystalline film absorbs less light and that the heat conduction is increased in μc-Si:H.

Influence of the pulse length on the film temperature For pulse lengths in the range of 100 μs it is expected that no steady state temperature is reached during one pulse. This means that the maximum temperature in the film also depends on the length of the pulse l_p. The slits of the chopper is widened or narrowed to adjust l_p. Therefore an increase of l_p simultaneously leads to an increase of the duty cycle. Hence the time of the layer to cool down between two pulses is reduced.

To study the influence of the pulse length on the film temperature Raman

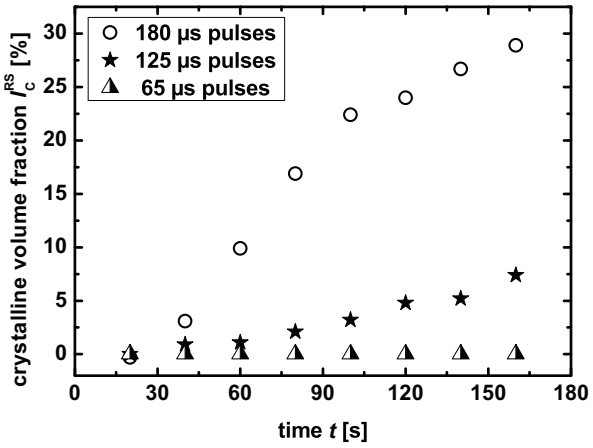

Figure 3.12: Crystalline volume fraction of an initially amorphous layer during pulsed laser illumination with a laser power of 0.5 W. The length of the laser pulses is varied from 65 μs via 125 μs to 180 μs.

measurements with an output power of 0.5 W and pulse lengths of 65, 125 and 180 μs were carried out. Figure 3.12 shows that for pulses longer than 65 μs a crystallization takes place. For a l_p of 125 μs the crystallization rate is very low. After about 100 s almost no crystalline fraction is detected. After an even longer illumination time a contribution of a small crystalline fraction is observed in the spectra. This could mean that the sample is not cooling down completely between two pulses and after a specific time enough heat is accumulated in the layer to initialize the formation of a crystalline phase. For a l_p of 180 μs the crystallization rate is higher. From these results it is concluded that with the given setup either the laser power has to be lower than 0.5 W or the pulse length shorter than 125 μs to avoid a crystallization of an amorphous layer.

Decreasing the film temperature by a larger laser spot To increase the maximum possible laser power without further increasing the temperature the light is dissipated over a larger area. Due to the quadratic dependence of the area of a spot on its radius, large reductions in energy density are achieved by

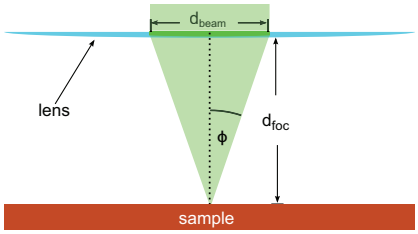

Figure 3.13: Part of the optical path used to calculate the diffraction limit of a laser beam.

moderate increases of the radius of the laser spot. Since the collected radiation is eventually focused onto the spectrometer entrance slit it is only possible to expand the beam in one direction without loosing intensity. This is realized by positioning a cylindrical lens in the optical path between the laser and the substrate. The resulting laser spot will have the shape of an ellipse.

To estimate the decrease of the power density, the size of the spot on the sample with and without the cylindrical lens is estimated:

The initial size of the spot cannot be smaller than the diffraction limit l_{diff} of a circular lens. Hence it depends on the wavelength of the light and the focal length of the lens used to focus the laser light onto the sample. It is defined as

$$l_{\text{diff}} = \frac{0.6 \cdot \lambda}{n \cdot \sin\phi} \tag{3.2}$$

where n is the refractive index of the surrounding medium (in this case $n = 1$ since the setup is in vacuum). The angle ϕ is calculated from the diameter of the laser beam and the focal length according to Figure 3.13. With a beam diameter of 0.7 mm and a focal length of 38 mm a l_{diff} of 35 μm is obtained. The increase of the size of the spot on the sample by a cylindrical lens is determined very roughly by recording an image of the spot with the CCD and counting the illuminated pixels. From the known pixel size of 26×26 μm^2 the elongation of the spot was estimated to about 1.3 mm. This means that the ratio of areas with (A_{elip}) and without cylindrical lens (A_{circ}) is at least 37

$$\frac{A_{\text{elip}}}{A_{\text{circ}}} = \frac{0.65\text{mm} \cdot 35\mu\text{m} \cdot \pi}{(35\mu\text{m})^2 \cdot \pi} = 37. \tag{3.3}$$

Even after long illumination of an amorphous samples with pulse lengths of more than 200 μs and a laser power of 1 W without an OD filter no crystallization was

detected. Without the cylindrical lens a maximum pulse length of 125 μs with a OD 0.3 filter was determined. Since the filter with an optical density of 0.3 reduces the delivered power density by a factor of 2 and expands the beam only slightly it is assumed that the sample is heated very little by 125 μs long pulses with a cylindrical lens and no gray filter. Hence no gray filter is applied when the cylindrical lens included in the optical path and the pulse length is increased to 220 μs to maximize the collected Raman signal.

Summary of the Experimental Results The laser parameters that were determined in this section allow a minimization of the laser induced temperature increase at sufficient signal intensities. By using pulse length of roughly 200 μs and expanding the beam by a cylindrical lens a temperature increase that is well below the crystallization temperature is expected at a laser output power of 1 W. Since the heating of the growing film is not completely avoided by this setup, it has to be made sure that the layer growth is undisturbed by the Raman measurements. The results obtained in Sections 4.3 and 5.3 indicate that the crystalline volume fraction of a growing film is not influenced by the Raman measurements.

3.5.2 Finite Element Simulations of the Laser Induced Temperature Increase

Geometry and physical Parameters used in the Simulation To get a better understanding of the way the thermal energy is dissipated in a thin silicon layer a finite element simulation using the software "elmer" was performed based on heat conduction and Lambert-Beer absorption. The procedure to simulate the absorption of laser pulses in thin film silicon is analogous to the method described by Haas [83]. The work of Haas is focused on the laser ablation of thin-film silicon for module fabrication. Hence the temperatures and power densities are much higher. In the temperature regime of Raman spectroscopy the physics is more simple since melting and evaporation of silicon do not have to be considered.

When describing the heating of a solid by laser pulses an important parameter is the thermal penetration depth(l_{th}). This parameter is calculated from the specific heat capacitance at constant pressure (c_{P}), the heat conductivity (λ_{th})

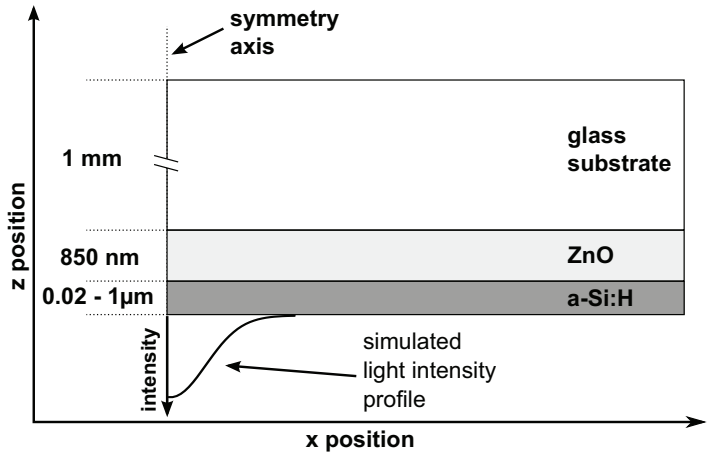

Figure 3.14: Schematic drawing of the simulated layer stack analogous to Reference [83]. Due to the symmetry of the laser pulse only half of the illuminated area has to be considered. The intensity distribution of the laser light is indicated.

and the density (ρ) of a material

$$l_{\mathrm{th}} = 2 \cdot \sqrt{\frac{\lambda_{\mathrm{th}} \cdot t}{\rho \cdot c_{\mathrm{P}}}} \tag{3.4}$$

where t is the duration of the pulse. Figure 3.14 schematically shows the layer stack used to simulate ΔT caused by a laser pulse. The Zinc Oxide and the glass substrate were assumed to be transparent for the considered wavelength of 532 nm. The reflection of light is also not included into the model. For the amorphous layer the absorption of the laser light is assumed to follow Lambert-Beer's law according to Equation 2.6 with a constant coefficient of absorption. The absorption coefficient is expected to decrease above the crystallization temperature due to a reduced absorption of the crystalline phase. This effect is not considered in the simulations. The thickness of the amorphous silicon layer was chosen to be 1 μm, that of the TCO 850 nm and that of the glass substrate as 1 mm. To account for the non perfect imaging of the system and the expansion of the beam by the gray filter the diameter of the circular spot on the sample was chosen as 100 μm. To reduce the calculation time the simulation was performed in a 2 D

geometry. The 2 D setup is chosen due to the relatively short laser pulses and the aim to determine the maximum temperature in the film as described below:

A cylindrical symmetry of the spot on the sample with the symmetry axis in the center of the spot was assumed in the simulations. For the simulation of an elliptical pulse –as created by the cylindrical lens– this assumption is not true since the elongation of the pulse is much larger in one direction than in the other. For the simulation of this system an infinite extension of the spot on the sample in one direction was assumed. Under this assumption the obtained temperature increase will overestimate the experimental values slightly:

The maximum temperature is expected at the center of the pulse. Hence the minor semi-axis of the ellipsoidal spot includes the point with maximum temperature. The ratio of the minor and major axes of the ellipse is very small (50 μm/1.3mm). Hence the power density close to the center is assumed as constant on small length scales at positions along the major axis. The thermal penetration depth l_{th} is about 19 μm for amorphous silicon at pulse lengths of 220 μs. This means that due to the approximately constant power density along the y axis of Figure 3.14 on this length scale the same amount of heat is transported in and out of the simulated area in the y direction.

The thermal conductivity and the heat capacitance of zinc oxide and amorphous silicon are temperature dependent. This effect was accounted for in the simulations according to References [84, 85, 83]. The temperature of the backside of the substrate was held constant at 400 K. This is also the initial temperature set for the layer stack.

The interface towards the vacuum of the silicon layer was assumed as thermally isolated. This assumption is valid since no heat conduction due to convection is possible in a vacuum chamber. Due to the relatively small increase in temperature, the short pulses and the large energy of the laser pulses the radiative emission of heat can also be neglected in the considered time frames [86].

In the x-direction of Figure 3.14 the laser beam is described by a Gaussian intensity distribution. It was assumed that the power density is dissipated in a Gaussian distribution in x and y direction of the pulse. For a circular pulse it is assumed that the full width at half maximum (FWHM) of the Gaussian distribution is at the radius of the laser spot. The same assumption was made for an ellipsoidal spot with the difference that the measured elongation caused by the

cylindrical lens is chosen as the FWHM in the y-direction. The power density used in the simulation is calculated from these dimensions. Due to the symmetry of the laser spot it is sufficient to simulate only one half of the pulse. As indicated in Figure 3.14 the axis of symmetry of the laser pulse has to be at the edge of the simulated sample to make use of this simplification. The variation of time of the laser intensity was approximated by a rectangular shape since the sharp edge of the chopper slits determine the on and off time of the laser. The length of the individual time steps of the simulation was set to 200 ns.

Computational Results of the Temperature Increase Figure 3.15 shows

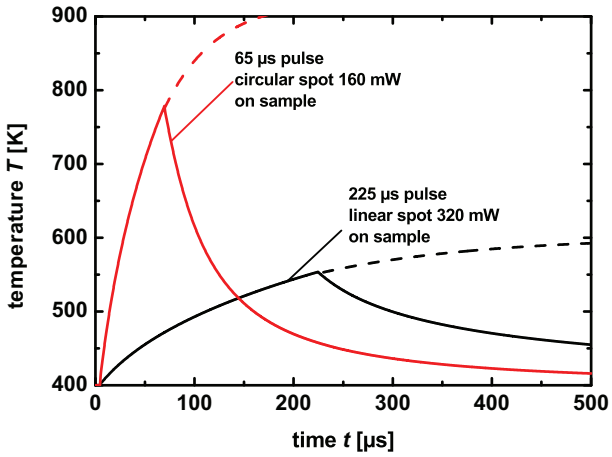

Figure 3.15: Simulated temperature increase (continuous lines) caused by the illumination of a sample by an elliptical spot and a circular spot. The dotted lines represent an exponential fit. The input powers are 1 W and 0.5 W for the elliptical and the circular spot respectively. This results in about 320 mW and 160 mW on the sample. The simulated pulse lengths were 225 μs for the elliptical spot and 65 μs in the circular case.

examples of the temperature increase caused by one laser pulse and the subsequent cooling when the optical path of the laser is blocked by the chopper. In

the figure the temperature increase caused by a circular laser spot with an input power of 0.5 W is compared to that of an elliptical laser spot with an input power of 1 W. The laser pulse starts at 5 μs. A fast increase of the temperature, with a larger rate for the circular spot, is observed in both cases. After the end of the laser pulse the film starts to cool down. The initial temperature of 400 K is almost obtained after a total duration of 500 μs in the case of the short circular pulse.

Under the conditions assumed in the simulation the temperature seems to approach a maximum for long pulses. In this case the heat transfer towards the edges of the sample –which were chosen as heat sinks– will be the same as the amount of heat transfered to the layer by the laser. In an experiment this maximum temperature will be lower since heat transfer by radiation and convection has not been considered in the simulation.

An exponential increase of T is fitted to the temperature curves during illumination

$$T = A \cdot \exp(-t/t_{heat}) + T_0. \tag{3.5}$$

The sum of the constants A and T_0 equals the initial temperature of the sample and the time constant t_{heat} describes the heating rate which depends on spot size and input power. For a long pulse duration time the maximum temperature approaches T_0. Hence the maximum temperature increase T_{max} can be estimated from equation 3.5 as a function of the pulse length without having to perform complete simulations. The cooling of the layer after a pulse can also be fitted with the exponential function described by equation 3.5 and the opposite sign of the constant A.

Discussion of the Simulation The simulations provide additional insight into the experimental data. Even though the absolute values that were obtained have to be considered as upper limits the informations about heating and cooling rates give valuable insight into the laser induced temperature variations. The strong difference in crystallization rate for varying pulse length illustrated in Figure 3.12 could be explained by the large rate of temperature increase during the initial phase of heating obtained in the simulations. The simulated maximum temperature increase with a cylindrical lens is much lower than without, although the input power is higher. Even though convection and radiative emission were not

minimum deposition pressure [Torr]	line density of shield [1/cm]	laser power at sample [mW]	laser pulse length [μs]
10	10	320	< 250

Table 3.4: Minimum deposition pressure, line density of the electric shield, laser input power and laser pulse length at which the influence of the in-situ Raman measurements on the film growth is small.

considered as heat transfer mechanisms the film temperature seems to decrease relatively fast. Hence the times without illumination of more than 2 ms that were discussed in Section 3.5.1 should be sufficient to allow the layer to cool down between the individual pulses.

3.6 Summary

The successful design of a new electrode that enables the homogeneous deposition of μc-Si:H layers and in-situ Raman spectroscopy has been described in this chapter. The homogeneity of the layers deposited with the novel system is strongly related to the deposition parameters. In Table 3.4 the parameters that have been obtained to minimize the influence of the Raman setup on the growing film are summarized.

The temperature increase caused by the laser used for Raman spectroscopy was studied. To maximize the collectable light the spot size on the sample was expanded by a cylindrical lens. With this additional component the impact of in-situ Raman measurements on the growing film are small when the parameters described in Table 3.4 are applied. The temperature increase determined in this chapter has to be seen as an estimate since the conditions during deposition are be different from the studied ones. In Sections 4.3 and 5.3 no laser induced crystallization is found, with the laser parameters determined in the present chapter, in a comparison of the crystalline volume fraction that is obtained in-situ with measurements that were carried out after the deposition.

4 Determination of the Crystalline Volume Fraction of Growing μc-Si:H Layers

With the optimized experimental configuration and the measurement parameters obtained in the previous chapter that are summarized in Table 3.4 it is possible to perform in-situ Raman measurements during the deposition of a microcrystalline silicon layer. The impact of the setup and the measurements them self on the growing film is expected to be small. In the present chapter the parameters that determine the temporal resolution are described. It is also shown that for an accurate determination of the crystalline volume fraction one has to make sure that background contributions are carefully removed from the recorded spectra. In-situ measurements during the growth of a film with an intentional variation of the crystalline volume fraction are performed and compared to depth dependent measurements carried out after the deposition. The suitability of in-situ Raman spectroscopy for the study of the initial phase of the deposition of a μc-Si:H layer is demonstrated.

4.1 Recording and Processing of the in-situ Raman Spectra

The temporal resolution of in-situ measurements is a crucial parameter since it determines the timescale on which changes of the studied material can be detected. It depends on the framework conditions set by the read out times, the dark- and read-out noise of the CCD camera and the intensity of the Raman

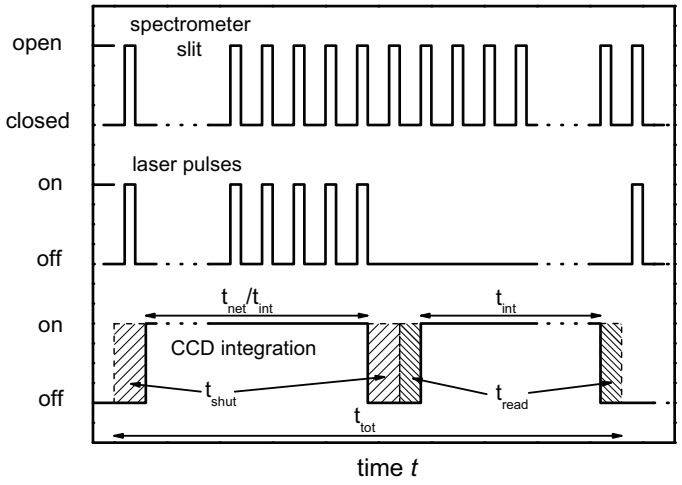

Figure 4.1: CCD exposure, laser pulsing and CCD integration during one in-situ Raman accumulation of the duration t_{tot}. The nett integration time (t_{net}), the integration time (t_{int}), the read-out time (t_{read}) and the shutter delay time (t_{shut}) are indicated.

shifted light. The main parameters that influence the signal-to-noise ratio will be studied in this section. To obtain the crystalline volume fraction background contributions have to be subtracted. In the following the origin and the magnitude of the background contributions is studied.

4.1.1 Parameters Determining the Duration of a Measurement Interval

The main parameters that determined the duration (t_{tot}) of an in-situ measurement are the integration time (t_{int}) of the CCD camera and the number (n_{acc}) of accumulations. Together with the read out time (t_{read}) of the CCD camera and the open/close time (t_{shut}) of the shutter used to switch the laser beam on and off these parameters determine t_{tot}. By increasing n_{acc} and t_{int} the intensity of the Raman signal is increased due to the increased number of pulses recorded by the CCD but the temporal resolution declines. The net integration time t_{net} during

which the Raman signal is recorded is defined as:

$$t_{\mathrm{net}} = t_{\mathrm{tot}} - n_{\mathrm{acc}} \cdot (t_{\mathrm{int}} + 2 \cdot (t_{\mathrm{shut}} + t_{\mathrm{read}})) \tag{4.1}$$

During each accumulation one t_{int} is used to record the plasma background signal. Since the shutter has to open and close during each measurement cycle and the Raman and the plasma background both have to be read out from the CCD chip t_{shut} and t_{read} have to be subtracted twice. Figure 4.1 schematically shows the time course of the data collection during one accumulation. To guarantee that no laser light enters the spectrometer during the recording of the background spectra t_{shut} was set to 250 ms. This means that together with a t_{read} of roughly 0.5 s about 0.75 s are not used for the integration of the Raman light during each accumulation independent of the integration time.

4.1.2 Parameters Determining the Intensity of the Collected Signal

In this section the factors that determine the collectable signal intensity are described. Figure 4.2 shows a typical Raman spectrum recorded during the deposition of a μc-Si:H film in comparison to an ex-situ reference spectrum. For this deposition 10 spectra with an integration time of 1 s have been accumulated which results in a t_{tot} of about 28 s. The growth rate during this measurement was about 2.5 Å/s. Hence a layer with a thickness of about 7 nm is deposited during each measurement interval. The in-situ spectrum shown in Figure 4.2 shows the characteristic shape of microcrystalline silicon with a lower signal-to-noise ratio when compared to the reference spectrum. The main reason for this is the lower t_{tot} used for the integration of the in-situ spectrum. The position of the in-situ peak is shifted from 520 cm^{-1} to roughly 515 cm^{-1}. This is attributed to the elevated temperature of the film which is about 130°C [87]. The increased width of the microcrystalline peak is also partially due to the temperature of the film. Additionally the spectral resolution of the in-situ experiment is smaller due to the reduced line density of the diffraction grating applied in the spectrometer.

Apart from t_{tot} the intensity of the Raman signal is also determined by the thickness of the film and its crystalline volume fraction. This is especially important during the initial phase of deposition. For thicknesses at which not all of

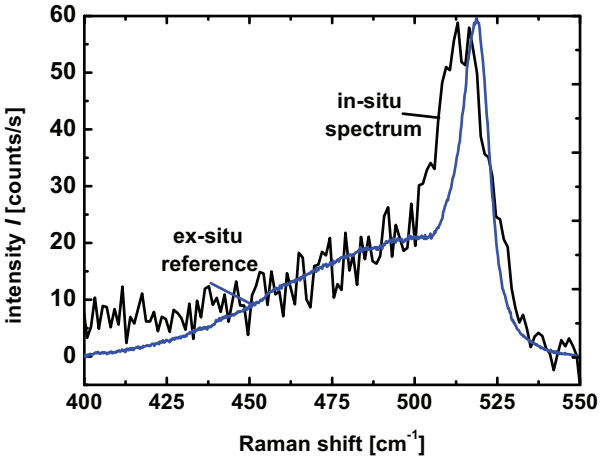

Figure 4.2: Stokes Raman shift recorded in-situ compared to an ex-situ reference spectrum. The in-situ spectrum is recorded at with a total integration time of about 28 s.

the laser light is absorbed in the silicon laser the signal increases with increasing layer thickness. At this stage of deposition the intensity of the Raman signal is modulated by interference effects caused by multiple reflections at the Si/TCO and the Si/vacuum interface.

Figure 4.3 shows the intensity of the Stokes peak during depositions with deposition rates of 0.26 nm/s (low rate) and 0.64 nm/s (high rate). The high rate case represents the standard conditions for solar cell deposition described in chapter 2. To reduce the deposition rate and maintain state of the art solar cell performance the input power is decreased to 0.2 W/cm^2 and the silane concentration is adapted. As described in Reference [88] state of the art solar cell performance is achieved in this regime at a growth rate of approximately 2.5Å/s.

For both depositions the intensity varies as a function of the deposition time (t_{dep}). A modulated intensity of the Raman scattered radiation caused by interference effects is visible at the beginning. After the thickness of the layer is large enough so that most of the light is absorbed the modulation disappears. The knowledge about the distance (Δt) of two maxima or minima is used to

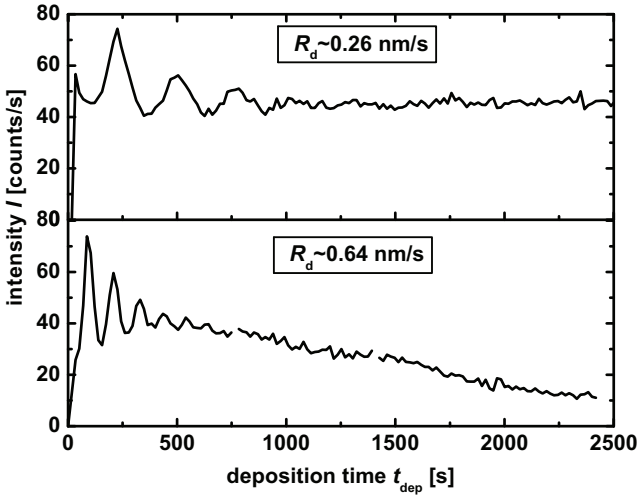

Figure 4.3: Intensity of the Stokes peak during two depositions with growth rates of 0.26 nm/s and 0.64 nm/s. The modulation of the intensity at the beginning of the deposition are caused by multiple reflections inside the growing silicon film.

determine the growth rate (R_d) in-situ [89, 90] when assuming that a layer with a thickness $R_\mathrm{d} \cdot \Delta t$ is deposited during one time interval Δt. The conditions for constructive or destructive interference then result in

$$R_\mathrm{d} = \frac{\lambda}{2 \cdot n \cdot \Delta t} \tag{4.2}$$

where n is the refractive index of silicon and λ the wavelength of the Raman shifted light. Since the films are deposited on rough TCO substrates the path length of the light is enhanced inside the silicon. This effect is corrected for by using an effective refractive index (n_eff) in equation 4.2 [11]. To estimate n_eff the growth rate is determined ex-situ from a thickness measurement with a profilometer and the total deposition time. Assuming a constant growth rate during one deposition a n_eff of 3.9 is determined for a standard deposition. This n_eff is used for all depositions on standard ZnO substrates.

For the high-rate case a strong decrease of total intensity with deposition time is observed. This reduction of the intensity is due to the coating of the lens protection with a silicon film that was described in Chapter 3. When looking at

Figure 4.3 it can be seen that the magnitude of this effect strongly depends on the applied deposition conditions. In the low growth rate regime the signal intensity stays almost constant with time while it decreases rapidly in the high-rate case.

There are several possible explanations for this effect: A change of the mean free path of growth precursors at a change of the deposition conditions could lead to the different characteristics of the intensities. Since both layers were deposited at the same pressure the mean free path is expected to be similar. Hence a difference in the lifetime of the radicals that are coating the lens protection could be responsible for the difference in intensity decrease. In the high-rate case far more growth precursors seem to reach the glass plate and subsequently the protection is coated much faster. Another possible explanation is that the disturbance of the plasma is different for the two deposition regimes. A possible penetration of the plasma bulk into the feed through in the high rate case could lead to a faster coating of the optics.

Due to the signal loss caused by the coating of the lens protection a frequent replacement is carried out. To guarantee for equal properties of the reaction chamber after the replacement process a solar-cell is deposited under standard conditions prior to the in-situ studies. During this deposition the metal plate mentioned in Section 3.2.2 is covering the optical feed through. The silane concentration during deposition of the standard solar cell is adjusted to obtain the same performance as achieved prior to the replacement of the lens protection.

4.1.3 Background Contributions to an In-Situ Signal

A detectable Raman signal is generated by the quartz components used to guide to light. As seen in Figure 3.1 the laser light is focused on the sample by a lens. On the way to the sample it also passes the lens protection plate. To estimate the intensity of the signal that is generated in the optical components of the in-situ setup measurements without a substrate holder inside the deposition chamber were performed. The detected signal with lens protections made from different materials is compared to a spectrum that was measured without any protection plate. In these measurements very little light is directly reflected back from the focal plane inside the deposition chamber.

In Figure 4.4 the spectra are compared. A broad Raman signal centered at

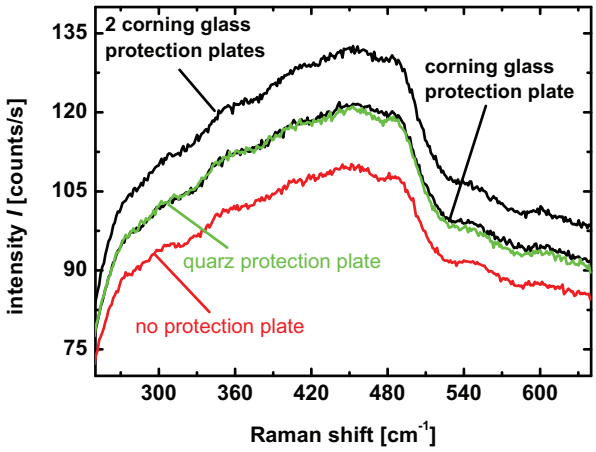

Figure 4.4: Signal generated by the optical components of the in-situ experiment. No substrate or layer was in the focal plane of the experiment during the measurements. The signal generated without a lens protection is compared to those with one and two Corning Eagle XG protections and one quartz protection. No baseline was subtracted from the spectra.

about 450 cm^{-1} is shown for all the studied configurations. When comparing the intensities shown in Figures 4.2 and 4.4 it can be seen that the signal generated by the optical components contributes a considerable share to an in-situ spectrum. In Figure 4.4 measurements with one and two Corning Eagle XG protection plates and one quartz glass plate without any substrate at the focal plane are compared to a spectrum recorded without a lens protection. The spectra with one Corning glass and one glass plate are almost identical. Since the Raman signal which originates from the Corning glass should differ from that of a quartz plate it is concluded that the Raman signal shown in the figure is not generated in the protection plate. Hence the lenses used to guide the light onto the sample seem to be the main sources of this signal. The increase of intensity with two plates could be explained by the increased back reflection from the additional interfaces which leads to an enhanced amount of Raman scattering inside the quartz lenses.

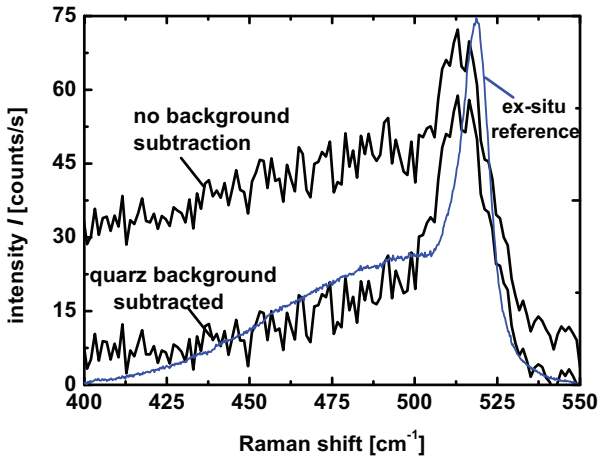

Figure 4.5: Spectrum recored from a silicon film with and without a subtraction of the quartz background signal compared to an ex-situ reference spectrum.

Since the lenses are not affected by the deposition inside the PECVD chamber the shape and intensity of the generated signal is assumed as constant throughout the deposition of a layer. Hence it is subtracted with a constant intensity from the measured Raman spectra. The difference of two spectra with and without a quartz background correction are shown in Figure 4.5.

Another important contribution to the measured spectra originates from the ZnO substrate on which the layers are deposited. Figure 4.6 shows the Raman shift generated by a TCO substrate together with a reference spectrum of an a-Si:H layer. The quartz contribution has been subtracted from the spectra. It can be seen that large parts of the spectra are overlapping. The TCO contribution will be dominant during the initial in-situ measurements of a growing film since the silicon signal is relatively weak at this point due to the still thin layer. For an accurate determination of the crystalline volume fraction during this phase the substrate contribution is removed.

To do this a spectrum of the substrate to be coated is recorded prior to every deposition. The substrate is heated to the deposition temperature before this

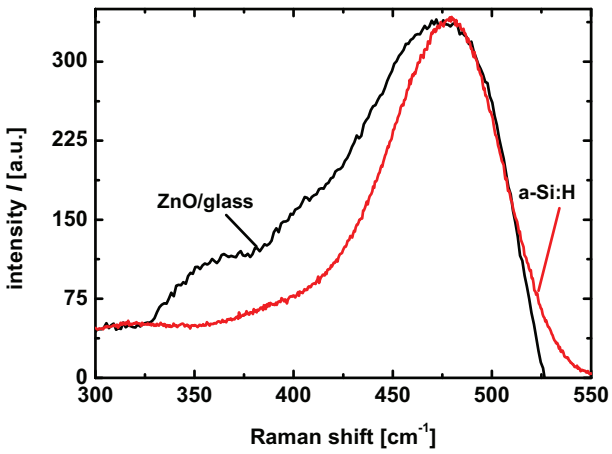

Figure 4.6: Stokes Raman shift generated by a ZnO/glass substrate compared to that of an amorphous silicon layer.

measurement. It has been shown previously that the intensity of the initial spectra is determined by interference effects in a growing film. To enable a consistent reduction of the substrate contribution the intensities of all the measured spectra –including the TCO spectrum– are normalized to the intensity of the first in-situ spectrum. This procedure is reasonable since the first in-situ spectrum is expected to mainly represent the substrate contribution. Due to the increase of the thickness of the silicon layer with time the contribution of the substrate decreases in the subsequent spectra. The rate of the decrease is approximated by assuming a Lambert-Beer like absorption of the laser light and the Raman scattered phonons in the silicon layer. Under this assumption the decrease of the initial substrate contribution $I_{\mathrm{sub},0}$ is estimated

$$I_{\mathrm{sub}}(d) = I_{\mathrm{sub},0} \cdot \mathrm{e}^{(-\alpha(\lambda)d)} \cdot \mathrm{e}^{(-\alpha(\lambda+\Delta\lambda)d)} \approx I_{\mathrm{sub},0}\mathrm{e}^{(-\alpha(\lambda)d_{\mathrm{avg}})}. \tag{4.3}$$

Here d is the thickness of the silicon layer and α the absorption coefficient which is assumed to be the same for the laser wavelength λ and the wavelength of the Raman shifted light. Since the silicon layer is growing during one measurement interval there is no definite thickness d. Hence the average thickness (d_{avg}) during one measurement interval is used in equation 4.3. It is determined from R_{d} and

t_{dep} of the measurement.

With this procedure for the subtraction of the substrate signal and the removal of the quartz background it is now possible to estimate the crystalline volume fraction of a thin silicon film in-situ.

4.2 Estimation of the Errors in the Determination of the Crystalline Volume Fraction

Three major sources of error have to be considered concerning the determined crystalline volume fraction:

- An incorrect subtraction of the quartz background signal.
- An over- or underestimation of the substrate contribution which is especially important during the initial phase of layer growth.
- The measurement noise that is relatively large due to the short integration times used during an in-situ measurement.

The quartz background signal is recorded with very long integration times. Since it originates from optical components that are not influenced by the deposition it is assumed as constant. Hence the error introduced by the subtraction of the background signal is neglected.

Due to the low absorption of the silicon layer during the initial phase of layer growth the subtraction of the ZnO substrate signal is especially important during the initial measurements. As shown in Figure 4.6 the Raman shifts of the ZnO/glass substrate and that of a-Si:H are overlapping in a large parts. Hence $I_{\mathrm{C}}^{\mathrm{RS}}$ will be overestimated if the subtracted contribution of the substrate is too large.

Since the absorption coefficient α used in equation 4.3 depends on the crystalline volume fraction of the material –which still has to be determined– it is not exactly known. This introduces a large error since α varies from approximately $4 \cdot 10^4 \mathrm{cm}^{-1}$ to $9 \cdot 10^4 \mathrm{cm}^{-1}$ for μc-Si:H and a-Si:H material respectively. Hence an average α of $6.5 \cdot 10^4 \mathrm{cm}^{-1}$ with an absolute error $\Delta\alpha$ of $2.5 \cdot 10^4 \mathrm{cm}^{-1}$ is assumed for the substrate subtraction in a first approximation.

Due to uncertainties in the determination of the deposition rate d_{avg} is not

known with a precision that is large enough to exclude a possible error arising from this parameter. The deposition rate can be determined either in-situ using equation 4.2 or after the deposition from the total thickness and the deposition time. The error introduced by these methods is relatively small compared to the uncertainty $\Delta\alpha$ of α. Hence the error in absorption coefficient is assumed as dominant one considering the substrate contribution. The relative error of the subtracted substrate intensity (I_s) is determined according to equation 4.4

$$\frac{\Delta I_\mathrm{s}}{I_\mathrm{s}} = \frac{1}{I_\mathrm{s}} \cdot \frac{\partial I_\mathrm{s}}{\partial \alpha} \Delta\alpha = \frac{1}{I_\mathrm{s}} (-2 d_\mathrm{avg} \cdot \Delta\alpha) \cdot I_\mathrm{s} = -2 d_\mathrm{avg} \cdot \Delta\alpha. \tag{4.4}$$

Due to the decrease of the silicon signal caused by the coating of the lens protection the measurement noise becomes more dominant with increasing deposition time. The noise introduces an uncertainty in the contribution of the amorphous fraction to the total intensity. To estimate the resulting error of I_C^RS equation 2.5 is rewritten

$$I_\mathrm{C}^\mathrm{RS} = 1 - \frac{I_{480}}{I_{520} + I_{480}} = 1 - \frac{I_{480}}{I_\mathrm{tot}}. \tag{4.5}$$

Here I_tot is the total signal intensity. The absolute error of I_C^RS is estimated as following

$$\Delta I_\mathrm{C}^\mathrm{RS} = \frac{\partial I_\mathrm{C}^\mathrm{RS}}{\partial I_{480}} \cdot \Delta I_{480} = -\frac{\Delta I_{480}}{I_\mathrm{tot}}. \tag{4.6}$$

To estimate the absolute error of the amorphous contribution, ΔI_{480}, the standard deviation of the measurement noise (σ_noise) in the region from 400 cm^{-1} to 500 cm^{-1} is determined and the absolute error is estimated as $\sigma_\mathrm{noise} \cdot I_{480}$.

As a conclusion the uncertainty in the absorption coefficient of the growing film and the subsequent uncertainty in the subtraction of the substrate contribution will be the major source of error during the initial phase of deposition. The error that is caused by the noise in the measured signals will be dominant for films that are thicker than the information depth of a layer.

4.3 In-Situ Measurements of the Crystalline Volume Fraction

In this section in-situ measurements performed on a growing film are compared to data collected ex-situ on the same sample. The suitability of the in-situ setup to detect changes of the crystalline volume fraction of a growing film is validated by observing changes induced by varying deposition parameters [91].

4.3.1 Crystalline Volume Fraction Determined During the Deposition of an Intrinsic μc-Si:H Film

In-situ measurements of the crystalline volume fraction during the growth of a μc-Si:H film were carried out to study the ability of the in-situ setup to detect changes in the growth of a layer. A non-constant crystalline volume fraction was induced to the growing film by varying the SC with time. Figure 4.7 a) shows the $I_{\mathrm{C}}^{\mathrm{RS}}$ determined in-situ together with data obtained after the deposition as described in Section 4.3.2. In Figure 4.7 b) the silane concentration during the deposition is shown. As described in Chapter 2 the film crystallinty is expected to decrease with increasing SC at otherwise constant depositions conditions.

The spectra used to obtain the in-situ $I_{\mathrm{C}}^{\mathrm{RS}}$ were recorded with the settings summarized in 3.4 and 5 accumulations of 1 s each which results in a t_{tot} of 17.5 s. The quartz and ZnO contributions were subtracted according to Section 4.1.

The figure clearly shows that the crystalline volume fraction determined in-situ follows the trend that was intended by profiling SC. The crystalline volume fraction increases from roughly 40 % to about 80 % during the first 300 nm. This increase is attributed to gradual increase of $I_{\mathrm{C}}^{\mathrm{RS}}$ that has been observed previously [92, 93, 9]. In these studies the formation of an amorphous incubation layer and a subsequent nucleation of crystalline grains was observed. The crystalline volume fraction obtained in-situ is influenced only weakly by the increase of SC from region I to region II in Figure 4.7 b). A small decrease from 80 % to about 70 % of the average $I_{\mathrm{C}}^{\mathrm{RS}}$ is observed. The second increase of the SC from region II to III in the figure results in a stronger change of the crystalline volume fraction obtained in-situ. The $I_{\mathrm{C}}^{\mathrm{RS}}$ decreases with deposition time to an average of roughly

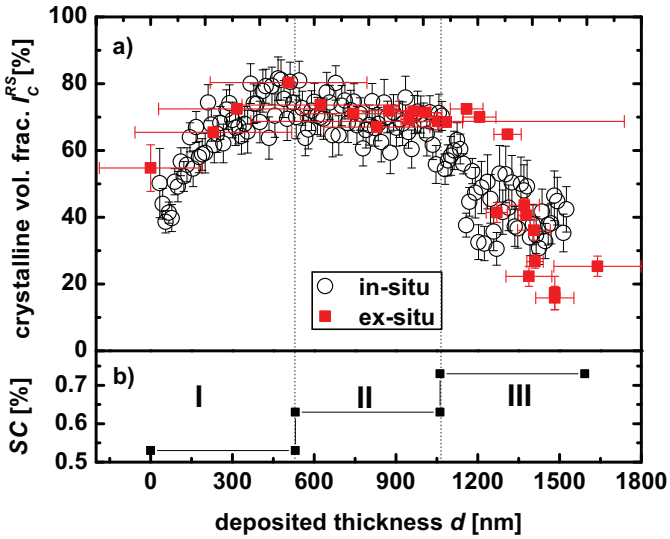

Figure 4.7: a) In-situ and ex-situ measurements of the crystalline volume fraction as a function of deposited film thickness.
b) Silane concentration during the deposition of the layer.

35 %. Towards the end of deposition the error in I_C^{RS} increases due to the decrease of intensity of the signal caused by the coating of the optical components by radicals from the plasma.

Even though the scatter of the in-situ data can not be neglected and despite the increasing error due to a weaker Raman signal towards the end of deposition, the measurements presented in this section show that it is possible to follow the evolution of the crystalline volume fraction during deposition with the newly developed setup. The reaction of the growing film to a change of process conditions –in this case a change of the gas composition– was observed. The measurements were performed with a temporal resolution below 20 s, which means that at the given growth rate about 10 nm of μc-Si:H were deposited during one measurement. Since the measurements were carried out with a laser wavelength of 532 nm a larger fraction than the grown 10 nm of the layer is probed during one measurement interval. This means the the data shown in Figure 4.7 does not only represent the crystallinty deposited at the time of measurement but a weighted average of the information depth of 125 nm. Due to the Lambert-Beer like absorption of the laser light the the newly deposited layer is contributing the largest fraction to the obtained signals. This might explain the fact that the change in deposition conditions is seen with a relative short delay in the figure.

4.3.2 Depth Dependent Ex-Situ Measurements

To validate whether the results obtained by the in-situ measurements are representative for the rest of the film they are compared to depth resolved measurements performed at a different local position. If the two methods are in agreement one can be sure that the influence of the laser heating and the disturbed electric field of the PECVD electrode caused by the Raman setup is small enough to leave the growth of a μc-Si:H layer unaffected.

Additionally to the influence of the measurement setup a potential difference between the ex-situ and in-situ data could also be expected due to a post crystallization that might happen during layer growth. As described in Section 2.2.2 some models for the growth of μc-Si:H assume an increase of the crystalline volume fraction of already deposited layers due to a deposition with a hydrogen rich plasma.

The depth resolved Raman measurements were carried out on a crater etched into the silicon layer. To enable a good depth resolution of the ex-situ measurement the slope of the crater wall has to be relatively small. A measurement setup that enables the etch of such craters into thin silicon films has been developed by Köhler *et al.* [94]. Figure 4.8 shows the depth profile of the crater etched into the film. By performing spatially resolved measurements in the area of the

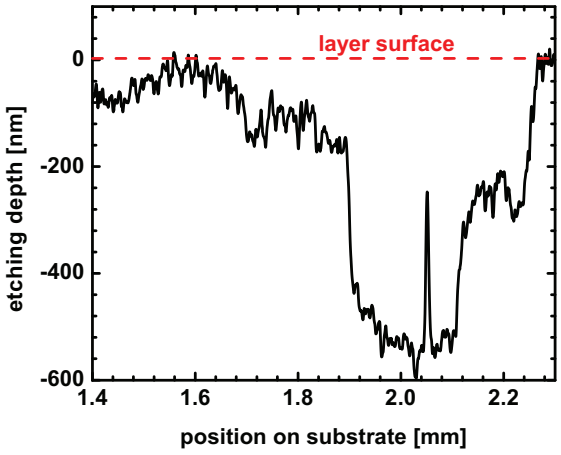

Figure 4.8: Depth profile of a crater etched into a silicon laser. By performing spatially resolved Raman spectroscopy on such a crater it is possible to get depth dependent information about the crystalline volume fraction of a layer.

crater it is possible to gain the depth resolved information about the crystalline volume fraction The thus obtained data is shown in Figure 4.7. These ex-situ measurements were carried out with a 488 nm laser in difference to the 532 nm used in-situ. Since the Raman scattering cross section for microcrystalline and amorphous material is similar for both wavelengths the influence of the wavelength on the crystalline volume fraction determined from the Raman spectra can be neglected [67, 68]. It can be seen that it is in good agreement to the in-situ data. During the initial phase of the deposition the increase of I_C^{RS} measured ex-situ follows the in-situ data. The slight decrease of I_C^{RS} that was observed

in-situ during the second phase of deposition is also found in the ex-situ data. During the third phase the strong decrease of I_C^{RS} that has been observed in-situ is reproduced by the ex-situ data. The ex-situ measurements however show a crystalline volume fraction that is about 15 % less than the in-situ results at the topmost fraction of the layer.

4.3.3 Comparison of Ex-situ and In-situ Measurements

An excellent agreement was found between the ex-situ and the in-situ Data during the major part of the deposition. For the topmost fraction of the layer a deviation was observed between the results obtained with the two techniques. There are two possible reasons for this difference: The Raman measurement setup could influence the layer growth. Additional heating by the laser pulses could promote the crystallization. This effect can not be dismissed completely. Especially at very low crystallinties –which represent material very close to the phase transition– small variations in the temperature could have an effect on the growing film. Also the inhomogeneities in the electric field could result in a small difference in the conditions at the position of the Raman measurements. In Section 3.4 the crystalline volume fraction opposite of the feed through with an electrical shielding was slightly higher than at the rest of the layer. The amplitude of this inhomogeneity however was much smaller than the 15 % difference between the ex-situ and in-situ results. Hence it can only partially explain the deviation.

The difference in information depth due to the two applied laser wavelength could also partially explain the difference. In the third section of the experiment described by Figure 4.7 the ex-situ as well as the in-situ measurements show a strong gradient in crystalline volume fraction. Assuming absorption coefficients of $4{\cdot}10^4$ cm^{-1} and $8{\cdot}10^4$ cm^{-1} for 532 nm and 488 nm light in μc-Si:H respectively [30, 95] the associated information depths are 125 nm and 63 nm. The I_C^{RS} is basically an average of the probed layer weighted by the absorption. In Figure 4.9 the fractions of a layer with a negative gradient in I_C^{RS} that are probed with the two wavelengths are shown schematically. Due to larger information depth obtained with the 532 nm laser the resulting crystalline volume fraction will be higher at this wavelength.

One could also think of subsurface reactions that take place after the material

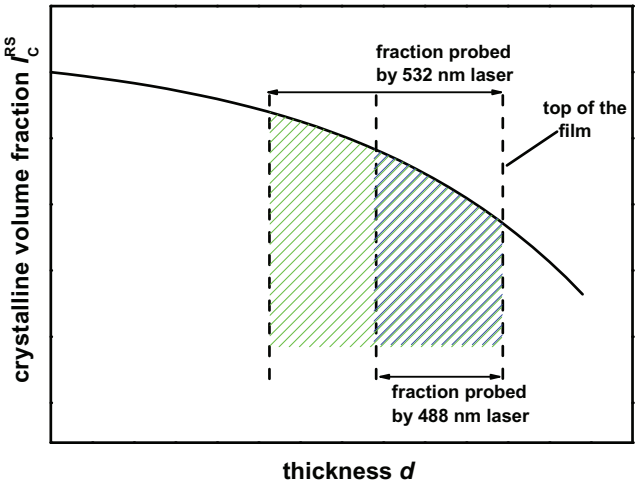

Figure 4.9: Schematic of the crystalline volume fraction in a layer with a negative gradient in $I_{\mathrm{C}}^{\mathrm{RS}}$. The fractions of the layer probed by a 488 nm laser and a 532 nm laser are shown in blue and green respectively.

has been deposited as a reasons for the difference in the ex-situ and in-situ results. As mentioned in Section 2.2.2 these reactions are believed to be responsible for the subsequent crystallization of μc-Si:H layers. This means that –assuming these reactions have not been completed during the in-situ measurements of the topmost fraction of the layer– the ex-situ $I_{\mathrm{C}}^{\mathrm{RS}}$ would be larger than the in-situ obtained crystalline volume fraction. Since the observations are vice versa the sub surface reactions can not be the reason for the observed difference of the in-situ and ex-situ data.

The results presented in this section show that the newly developed in-situ Raman setup provides valuable information about the composition of a layer during its deposition. At an excellent temporal resolution of less than 20 s the crystalline volume fraction was determined in-situ. The in-situ results are in a very good agreement to depth dependent measurements performed ex-situ on an etch crater.

4.4 In-situ Study of the Initial Phase of Deposition

In this section the applicability of the in-situ setup to study the initial phase of deposition with a high resolution of the deposited thickness is studied. The influence of different seed layers on the layer growth is observed in-situ and a method to influence the growth is tested.

4.4.1 Increase of the Depth Resolution

The initial phase of the deposition of the absorber layer is of great importance considering its influence on solar cell performance [96, 97, 98, 99]. At constant deposition parameters the properties of the μc-Si:H material are evolving in growth direction. This is due to the fact that no epitaxial like growth happens during a typical μc-Si:H deposition on amorphous substrates. Hence predominantly amorphous material –the so called incubation layer– is deposited before a detectable μc-Si:H phase develops.

Since the initial phase of deposition is characterized by an evolving crystalline volume fraction in-situ Raman spectroscopy is very suitable to study this important part of the deposition process. This gradual increase of $I_{\mathrm{C}}^{\mathrm{RS}}$ is expected to occur during the deposition of the first $\sim$ 100 nm. Hence it is beneficial to reduce the growth rate of the intrinsic layer to decrease the thickness of the layer that is deposited during one in-situ Raman measurement interval. The low input power, low growth rate regime described in Section 4.1 was applied to obtain state-of-the-art material at a growth rate of approximately 2.5 Å/s.

4.4.2 Influence of the Substrate on the Initial Phase of Deposition

To study the development of the $I_{\mathrm{C}}^{\mathrm{RS}}$ on the properties of different p-seed layers their crystalline volume fraction was determined. Figure 4.10 shows the Raman shift of three p-layers deposited with different silane concentrations (SC_{p}). The parameters of the p-layers are summarized in Table 4.1. These spectra were measured inside the process chamber prior to the intrinsic layer deposition. Since the

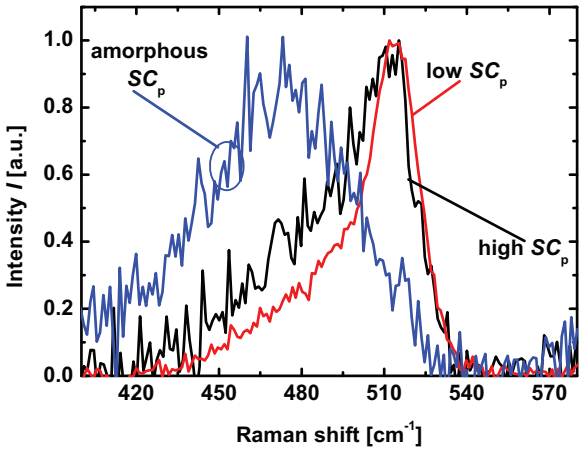

Figure 4.10: Raman shift of $\sim$ 20 nm thick p-layers that were deposited with different $I_{\mathrm{C}}^{\mathrm{RS}}$ measured prior to intrinsic layer deposition inside the deposition chamber.

layers are approximately 20 nm thick a total integration time of 60 s and 10 accumulations was used to record the spectra to increase the signal-to-noise-ratio. An $I_{\mathrm{C}}^{\mathrm{RS}}$ of 56 % and 64 % is estimated for the low and high SC p-layers respectively. The spectrum of the p-layer deposited with amorphous process conditions shows no crystalline contribution around 520 cm^{-1}.

The $I_{\mathrm{C}}^{\mathrm{RS}}$ of the intrinsic layer during deposition is determined with an integration time of 2 s and 5 accumulations. This results in a temporal resolution of $\sim$ 27.2 s. The long integration time was chosen to increase the signal-to-noise-

p-layer	SC_{p} **[%]**	$I_{\mathrm{C}}^{\mathrm{RS}}$ **p-layer**	SC_{I} **[%]**	**min** $I_{\mathrm{C}}^{\mathrm{RS}}$ **i-layer [%]**
amorphous	9.5	0	0.48	0
high SC	0.31	56	0.48	15
low SC	0.24	64	0.47	23

Table 4.1: Properties and deposition parameters of the p-layers and i-layers studied in-situ

ratio which is especially important for the very thin layers during the initial phase of deposition. Together with the R_d of 2.5 Å/s this results in roughly 7 nm that are deposited during one measurement interval.

Figure 4.11 shows the I_C^{RS} during the deposition of intrinsic absorbers on highly

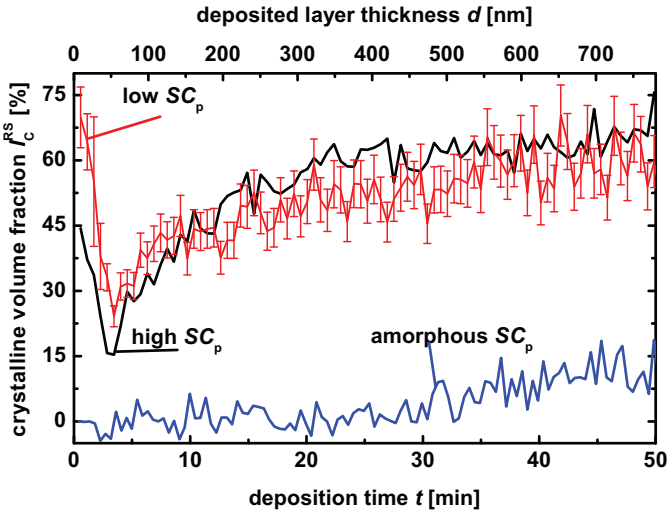

Figure 4.11: Crystalline volume fraction of intrinsic layers measured during deposition. The layers were grown on TCO substrates coated with p-layers deposited with a high silane concentration (high SC_p), a low SC_p and an amorphous SC_p.

crystalline p-layers. The silane concentrations (SC_I) used for intrinsic layer deposition are also shown in Table 4.1. The SC_I of the film deposited on the low SC_p p-layer is slightly lower. This adaption was carried out since the deposition chamber was cleaned between the measurements. To obtain optimum performance of the standard cell after replacement of the lens protection the SC was adjusted slightly.

It is shown in the figure that without a microcrystalline seed layer it takes almost 30 min or $\sim$ 450 nm until a crystalline contribution is observed in the Raman spectra. The scatter of the data around $I_C^{RS} = 0$ % –including negative values– is due to the noise in the spectra.

The situation is different for depositions on μc-Si:H seed layers. A decrease

of the measured I_C^{RS} from that of the p-layer towards roughly 23 % is observed for the layer deposited on the low SC_p layer. The minimum I_C^{RS} of the layer deposited on the high SC_p layer is about 15 %. A subsequent increase of I_C^{RS} is observed in both cases, resulting in a crystalline volume fraction of roughly 60 % and 67 % for the films deposited on the low SC_p and the high SC_p layers respectively.

The initial decrease of the crystalline volume fraction observed for the two films deposited on microcrystalline p-layers could be attributed to the formation of predominately amorphous material. This observation is rather surprising since both of the μc-Si:H p-layers are expected to act as seed layers for the intrinsic layer growth. The diffusion of silane molecules from the reaction chamber into the plasma volume observed in Reference [100] could be an explanation for the decrease of I_C^{RS} during the initial phase.

Both of the intrinsic layers show a relatively fast increase of the I_C^{RS} after the decrease at the beginning. As mentioned above the silane concentration during the two depositions was slightly different. This could be the reason for the faster increase of I_C^{RS} for the material grown on the low I_C^{RS} p-layer and the larger I_C^{RS} towards the end.The slight difference of SC_I seems to influence latter stages of deposition but the minimal I_C^{RS} obtained during the initial phase are contra directionally and seem to be dominated by the influence of the seed layers, which is similar to previous observations [101, 102, 103, 104, 105, 106, 107]. Otherwise the minimum I_C^{RS} of the film deposited on the low SC_p p-layer with a low SC_I would be expected to be smaller than the minimum I_C^{RS} observed on the high SC_p layer.

4.4.3 Controlling the the Initial Phase of Deposition

Constant material properties through the absorber layer are believed to result in improved solar-cell performance. The high amorphous volume fraction at the beginning of growth that has been observed in Figure 4.11 is expected to act as a barrier for the extraction of holes [108]. Hence a constant I_C^{RS} at the p/i interface could be beneficial for device performance. One way to improve the constancy of the I_C^{RS} is the active control of the silane concentration during the initial phase of deposition. Similar experiments have been carried out based on the stabilization

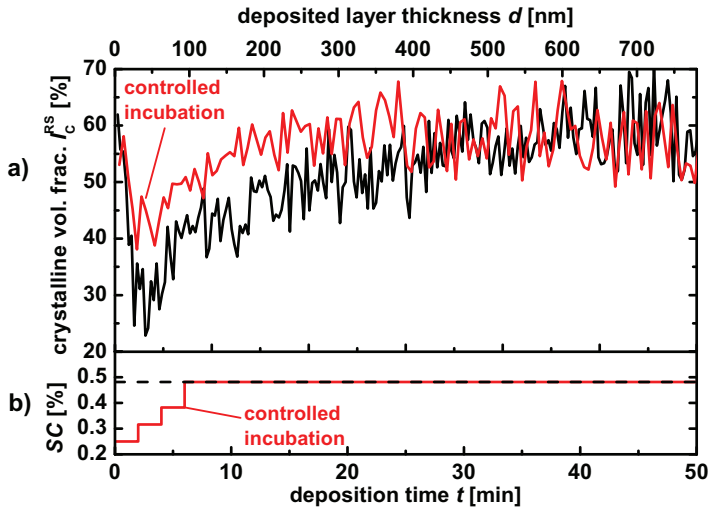

Figure 4.12: a) Crystalline volume fraction of layers deposited with and without an adjustment of the silane concentration during the initial phase of growth.
b) Silane concentration during deposition of the layers.

of the plasma emission [18, 109]. This method was applied to control the initial phase of deposition of the intrinsic film deposited on the low SC_p layer. In Figure 4.12 a) the I_C^RS of layers with and without a control of the SC during the initial phase of deposition is compared. Figure 4.12 b) shows the timely course of the silane concentrations during the depositions. It can be seen that the decrease of I_C^RS after the beginning of deposition is attenuated by profiling the SC. Whereas the layer deposited with constant SC shows a minimum I_C^RS of 23 % this minimum is reduced to $\sim$ 38 % for the layer deposited with a controlled initial phase of growth. A perfectly constant I_C^RS during the whole intrinsic layer was not yet achieved with this method. By further optimizing the SC profile this seems to be possible.

4.5 Summary

It was shown that it is possible to determine the crystalline volume fraction in-situ with the novel setup. To accurately determine I_C^{RS} in-situ, background contributions that originate in the plasma emission and in scattering on the optical components of the experimental setup and on the coated substrate were removed.

The accuracy of the determination of I_C^{RS} is influenced by the temporal resolution of the measurements. A minimum of 17.5 s is possible with reasonable signal-to-noise-ratio. By increasing the duration of one measurement interval the intensity of the collected silicon signal is increased at the cost of the temporal resolution. Hence the measurement parameters can be optimized for the studied question.

In-situ data were compared with results that were obtained after the deposition. Both are in excellent agreement during the major part of the deposition. This means that no hydrogen induced change of the crystalline volume fraction –as described in Section 2.2.2– was observed with the new experiment. Since the scanned fraction of the layer is relatively large these results do not exclude such a mechanism. If the hydrogen induced crystallization takes place in a very thin, topmost fraction of the growing film it is not possible to observe it with the given laser wavelength of 532 nm.

The important initial phase of the deposition of a μc-Si:H layer was studied on different substrates. A gradual increase of the crystalline volume fraction was observed in all cases. It was possible to change the rate of the increase by actively controlling the source gas flows during deposition.

5 Influence of a Process Instability on Layer Growth and Solar Cell Performance

In this chapter the application of the in-situ Raman setup to detect process disturbances is evaluated. The reaction of film growth and solar performance on a disturbance of the process gas flow was studied. With the obtained results it is determined whether the data collected by in-situ Raman spectroscopy can be used to counterbalance process instabilities by an active control of the gas flows.

5.1 Influence of a Process Disturbance on the Plasma and the Growing Film

In this section a reference experiment for a disturbance of the intrinsic layer growth is described. The reaction of the plasma composition to a change of the source gas flow is determined. The subsequent adaption of the crystalline volume fraction of the growing film is studied.

5.1.1 Design of the Experiment

The impact of variations in the process conditions on a growing film depends on three characteristics: The magnitude, the length and the point in time of the disturbance. A model experiment for an intentionally introduced disturbance is designed: Since the correlation between silane concentration and crystalline volume fraction of a layer is well known this parameter is varied during deposition.

The point in time (t_{dis}) and duration (w_{dis}) of a disturbance that is introduced intentionally is varied in the model experiment. The impact of the variations on solar cell performance, growth of the layer and the properties of the deposition plasma is studied. The point in time of the disturbance is defined as the time after starting the intrinsic layer deposition at which the disturbance is introduced. The layers studied in the model experiment are grown on texture etched ZnO substrates covered with a highly crystalline μc-Si:H p-layer with an estimated thickness of 20 nm. The p-layer is deposited to enable the preparation of solar-cells based on the studied intrinsic layers.

Figure 5.1 shows the silane and hydrogen flow during a disturbed deposition. The baseline of the gas flows results in a standard intrinsic layer used in μc-Si:H solar cells as described by Tables 2.2 and 2.1. An intentional disturbance to the layer growth is introduced by increasing the silane flow by a factor of 1.46 for a time w_{dis} of 180 s. At an expected growth rate of 5 Å/s this results in roughly 90 nm of disturbed layer growth. By changing t_{dis} the disturbance is introduced at different positions between the p/i and the i/n interface.

5.1.2 Reaction of the Plasma Composition to a Change of the Source Gases

To study the reaction of the plasma on a disturbance the optical emission was recorded during a step in SC. Figure 5.2 shows the ratio (I_{SC}) of intensities of a SiH^* line at 414 nm to the hydrogen beta line at 486 nm. This ratio is known to be proportional to the silane concentration inside a PECVD plasma [14, 15, 16, 17]. The spectra used to evaluate the intensities were recorded with the setup described in Section 2.3.2 at an integration time of 1 s and five accumulations which results is a temporal resolution of 5 s.

The plasma is ignited at $t = 0$ s. About 180 s after ignition I_{SC} stabilizes at roughly 0.72. The initial instability of the silane concentration in a PECVD plasma has been studied elsewhere and is attributed to the diffusion of silane molecules into the plasma zone from the rest of the reactor volume [100]. After 300 s the SC was increased from 1.05 % by 50 % to 1.56 %. A fast reaction of I_{SC} is observed. After a reaction time of roughly 10 s I_{SC} has reached a plateau value of about 0.81. This delay in the change of the plasma composition is attributed

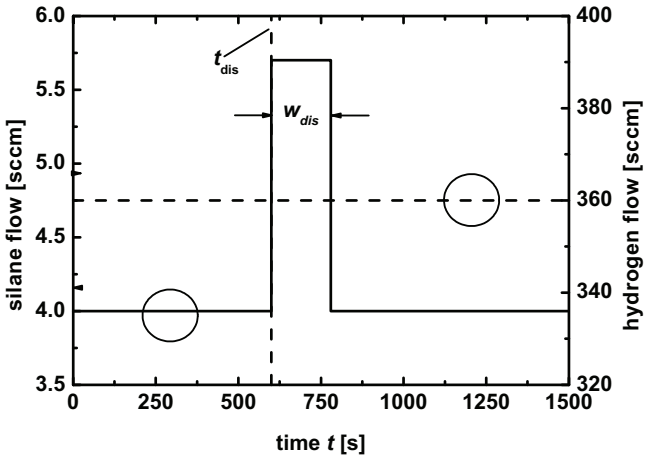

Figure 5.1: Silane and hydrogen source gas flows during a deposition with an intentional disturbance of the growth process. The silane flow is increased by a factor of 1.46 for 180 s at constant hydrogen flow. The position of the disturbance can be varied.

to the reaction times of mass flow controllers that regulate the gas flow and to the time it takes for the gas mixture in the deposition chamber to be completely replaced. For roughly 60 s some fluctuations are seen in I_{SC} before the plasma emission stabilizes. A similarly fast reaction of the plasma on a change of gas flow with almost no fluctuations is observed when the SC is reduced after 480 s.

5.1.3 In-situ Raman Measurements During a Process Disturbance

In-situ Raman spectroscopy offers a way to directly study the influence of a variation of process conditions on the crystalline volume fraction of a growing layer. Hence the combination of the information gained from OES and in-situ Raman spectroscopy enables the investigation of the connection between properties of the deposition plasma and the growing film.

To obtain information about the reaction of the film on the change of the gas

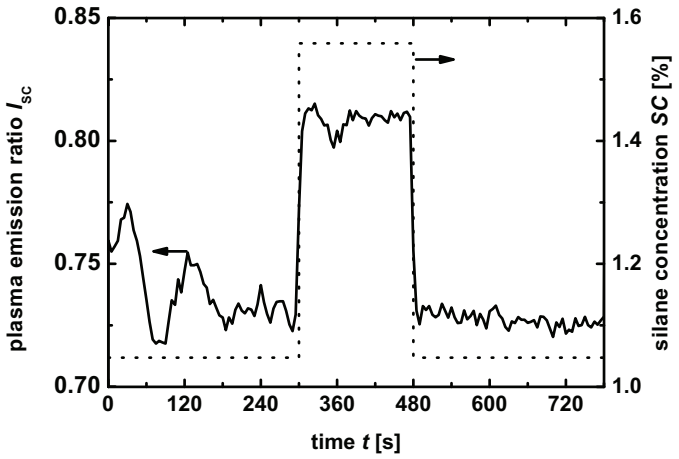

Figure 5.2: Ratio of the intensities of a SiH* line at 414 nm and the hydrogen beta line at 486 nm compared to the silane concentration during a deposition. The silane concentration was adjusted by changing the silane source gas flow.

composition at a good temporal resolution and signal to-noise-ratio 10 spectra of 1 s each were accumulated which results in a temporal resolution of about 35 s. The measurements were carried out with the parameters described in Table 3.4. Figure 5.3 shows the in-situ I_C^{RS} determined during a deposition with a t_{dis} of 840 s, which results in approximately 480 nm of deposited film and a w_{dis} of 180 s. The film thickness on the horizontal axis of the figure was calculated from the deposition rate of 5.8 Å/s which was determined using equation 4.2 and the time resolved intensity of the Stokes peak. The in-situ measurements show an increase of I_C^{RS} at the beginning of growth which represents the expected gradual increase of I_C^{RS} at constant deposition conditions described in Section 4.4. After about 150 nm a stable I_C^{RS} of $\sim$ 60 % developes. The increase of SC at t_{dis} is followed by a decrease of the measured I_C^{RS} to a minimum of about 17 %. When SC is decreased again the I_C^{RS} of the layer starts to recover to about 45 %.

The rate of I_C^{RS} increase as a reaction to the decrease of SC is lower than the rate observed after increasing SC. Also the observed final I_C^{RS} is lower than

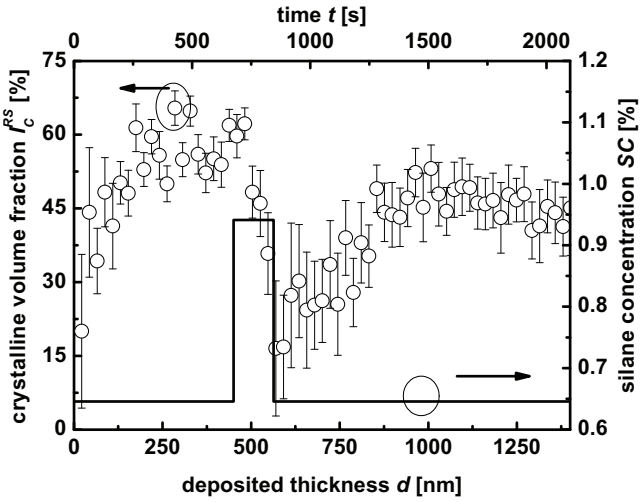

Figure 5.3: Crystalline volume fraction and silane concentration during the growth of a layer in which a disturbance of the silane concentration with a duration of 180 s was introduced after 840 s of deposition.

before the disturbance. The intensity of the Raman signal however is becoming relatively small towards the end of the deposition due to the coverage of the lens protection. Hence the uncertainty in I_C^{RS} is increasing.

To study the influence of the duration of a disturbance on the decrease of I_C^{RS} layers with a w_{dis} of 60 s, 180 s and 300 s and a t_{dis} of 1050 s were deposited. In Figure 5.4 the in-situ Raman crystallinities obtained during these depositions are compared. The t_{dis} of 1050 s results in about 650 nm of deposited layer prior to the disturbance. Before the change of SC an I_C^{RS} of approximately 62 % is observed for the layers. As seen in Figure 5.3 the crystalline volume fraction starts to decrease when SC is increased. The slope of the decrease of the I_C^{RS} curves is similar for the three depositions.

The minimum obtained crystalline volume fraction scales with w_{dis}. For the w_{dis} of 300 s the Raman spectra show a completely amorphous film towards the end of the disturbance. The measurements of the films with SC disturbances of a lower duration show the inclusion of a crystalline volume fraction at the time SC is decreased again.

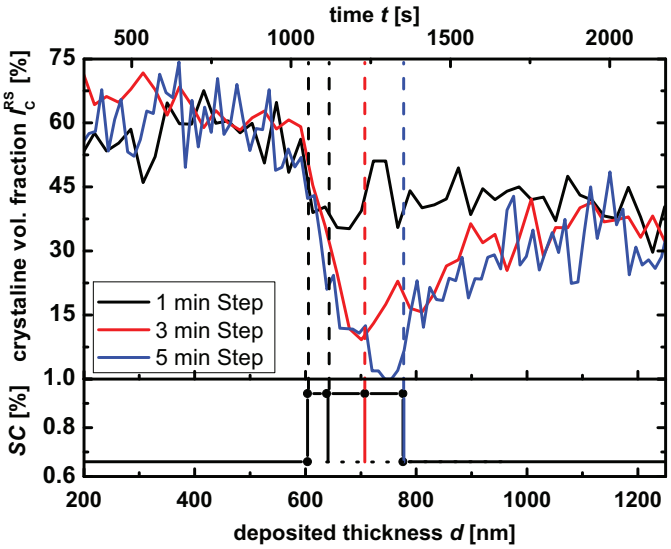

Figure 5.4: Crystalline volume fraction and silane concentration during the growth of three different layers. A disturbance of the silane concentration of three different durations (60 s, 180 s and 300 s) was applied after 1050 s of deposition.

After the SC is decreased the I_C^{RS} of the three layers is recovering towards its value before the disturbance. It stabilizes at roughly 40 % for all the depositions. As mentioned above the intensity of the Raman signal is reduced during this phase of deposition. Hence the error of I_C^{RS} increases with deposition time. To obtain an improved lucidity the error bars –that are comparable to those in Figure 5.3 are not shown in Figure 5.4.

5.1.4 Discussion

It was shown that it takes longer for the layer growth to adjust to a fluctuation of the source gas composition than for the plasma composition. There are two possible reasons for this behavior:

As discussed in Section 4.4 the part of a layer that has been grown previously provides a seed function for a continuing growth of silicon crystals. Due to the

change of the ratio between hydrogen and silane radicals in the plasma the involved growth mechanisms will eventually cause an amorphous film to grow. Due to the influence of the underlying film it is expected that this reaction of the film growth will take place gradually and not in the step like fashion as the change of plasma composition.

The crystalline volume fraction shown in Figure 5.4 represents –as discussed in Section 2.3.1– a weighted average of the fraction of the roughly 125 nm probed by the 532 nm radiation. This means that even if the topmost fraction of a layer does not contain a crystalline phase Raman spectra will show a positive $I_{\mathrm{C}}^{\mathrm{RS}}$ if the amorphous layer is relatively thin. Due to the growth rate of 5.8 Å/s the deposited thickness in one measurement interval is roughly 20 nm. As discussed in Section 4.1 the obtained Raman spectra represent a time average of one measurement interval. Hence a large share of the collected intensity is generated by a film that has been grown previous to the data collection. Figure 5.4 shows a continuous decrease of $I_{\mathrm{C}}^{\mathrm{RS}}$ during the deposition phase with an increased SC. Since about 180 nm are grown for a w_{dis} of 300 s the underlying layer that has been deposited under conditions optimized for μc-Si:H growth will contribute to the measured signal throughout almost the full duration of all the disturbances.

In conclusion in-situ Raman spectroscopy can not be used to determine the immediate reaction of the growth process to a change of deposition conditions. The composition of the plasma reacts within roughly 10 s to the changing gas flows. Due to the temporal resolution of 35 s and the large information depth of 125 nm a direct temporal correlation between the start of a disturbance and the reaction of the growth processes can not be made.

Nevertheless in-situ Raman spectroscopy provides an excellent way to study the influence of deposition parameters on the growth of a layer. A relatively fast decrease and a much slower increase of $I_{\mathrm{C}}^{\mathrm{RS}}$ were observed in-situ as the result of an increase and a subsequent decrease of the SC. For the studied amplitude of the disturbance it was possible to detect the process disturbance with in-situ Raman spectroscopy before a large fraction of the layer was affected. By decreasing SC to its initial value the crystalline volume fraction was increased after the disturbance without recovering to the initial $I_{\mathrm{C}}^{\mathrm{RS}}$. This process can be optimized by studying the reaction of a growing layer to an intentional change of SC in more detail. The thus obtained results can be used as an input for an active

process control.

5.2 Influence of a Process Disturbance on μc-Si:H Solar Cell Performance

In this section the influence of the position and duration of a disturbance of deposition conditions –in this case a temporal increase in silane concentration– on the performance of thin-film silicon solar cells is studied. The impact of the disturbance on the IV-characteristics of solar cells is correlated to the crystalline volume fraction obtained in-situ in the previous section.

5.2.1 Influence of the Position of the Disturbance

To study the dependence of solar cell performance on the position of a disturbance devices with various t_{dis} and a w_{dis} of 180 s were fabricated.

Figure 5.5 a) shows the FF and the V_{oc} as a function of t_{dis}. It can be seen that both parameters decrease if t_{dis} is changed from 0 s to 180 s. For a further increase of t_{dis} the FF increases continuously whereas V_{oc} reaches a maximum for a t_{dis} of 1050 s followed by a decrease for larger t_{dis}.

The J_{sc} of the resulting solar cells shown in Figure 5.5 b) is minimal for a t_{dis} of 0 s and increases continuously if the position of the disturbance is shifted towards the n-layer. Due to the characteristics of FF and V_{oc} the dependence of J_{sc} on t_{dis} results in the minimum of η for a t_{dis} of 210 s and an increase if the position is shifted towards the n-layer.

The open-circuit voltage of the solar cell with the disturbance directly at the start of deposition is strongly increased to a value expected for an a-Si:H device. When the position of the disturbance is moved towards the i/n interface the fill factor as well as the open-circuit voltage is increasing. The maximum observed in V_{oc} of 535 mV at a t_{dis} of 1050 s is larger than expected for the standard solar cell described in Table 2.1. Together with the relatively high FF and J_{sc} excellent characteristics for a μc-Si:H single junction solar cell are obtained. This result is rather surprising when considering the depth resolved crystalline volume fraction

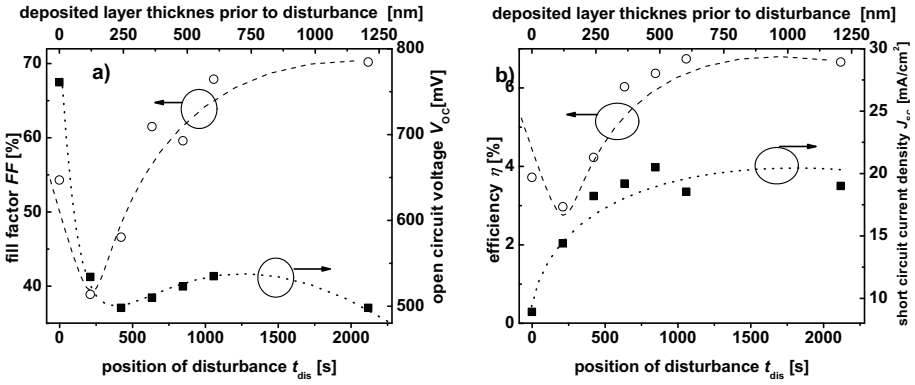

Figure 5.5: Solar cell a) fill factor and open-circuit voltage b) efficiency and short-circuit current density as a function of the position of a discontinuity in the silane concentration. The duration of the disturbance was 180 s for all the solar cells.

shown in Figure 5.4. In this figure it can be seen that for a w_{dis} of 180 s the crystalline volume fraction drops to less than 20 % which represents a discontinuity in the intrinsic layer that is expected to degrade the device performance.

The local maximum of V_{oc} at a t_{dis} of about 600 nm could be attributed to the beneficial effect of a active control of the SC described previously [110]. They observed an increase of the $I_{\mathrm{C}}^{\mathrm{RS}}$ with film thickness at constant deposition conditions. By increasing the SC with deposition time they managed to obtain μc-Si:H material with a relatively low $I_{\mathrm{C}}^{\mathrm{RS}}$ over its whole extend. If a disturbance like the ones described in this section results in a short decrease of the $I_{\mathrm{C}}^{\mathrm{RS}}$ this could prevent a detrimental increase of $I_{\mathrm{C}}^{\mathrm{RS}}$ with time.

The decrease of fill factor for small t_{dis} could be explained by the depth resolved measurements of the crystalline volume fraction shown in Figure 5.6 that were performed during the deposition of the solar cells. In this figure the $I_{\mathrm{C}}^{\mathrm{RS}}$ obtained in-situ during the first 30 minutes of deposition of solar cells with t_{dis} of 0 s and 210 s and a w_{dis} of 180 s are compared.For the intrinsic layer deposited with $t_{\mathrm{dis}} = 0$ s an initial crystalline fraction of roughly 20 % is observed. The $I_{\mathrm{C}}^{\mathrm{RS}}$ is strongly reduced with increasing deposition time. After more than 600 s –which is much longer than the duration of the disturbance– the crystalline volume fraction starts to increase towards roughly 50 % at a deposition time of

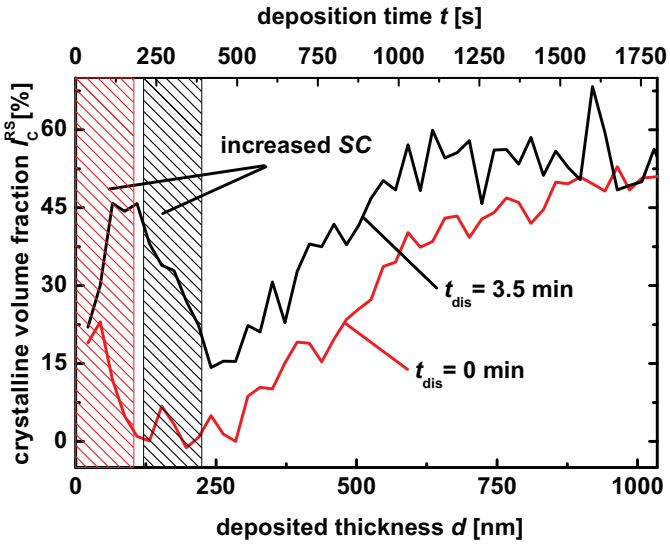

Figure 5.6: Crystalline volume fraction measured during the deposition of two intrinsic layer with a disturbance during deposition. The the position (t_{dis}) and duration of the disturbances are indicated by the hatched areas.

30 min. The intrinsic layer deposited with a t_{dis} of 210 s shows a different characteristics. Here the initial increase of $I_{\mathrm{C}}^{\mathrm{RS}}$ under μc-Si:H deposition conditions that has been observed before e.g. Section 4.4 is shown. After SC is increased the in-situ obtained crystalline volume fraction decreases by about 20 % towards the end of the disturbance. When SC is decreased again the film growth reacts with a relatively short delay. The crystalline volume fraction observed during the first measurements is partially attributed to the highly crystalline p-layer which contributes to the in-situ signal due to the large d_{inf}. The observed difference in the thickness of the disturbed layer could be explained by the fact that a completely amorphous layer is deposited during the initial phase for a t_{dis} of 0 s. Hence it can not act as a seed-layer for the film deposited with a reduced SC after the end of the disturbance. A similar effect was observed in Section 4.4 for an intrinsic μc-Si:H layer deposited on an a-Si:H p-layer. It is rather surprising that even though more than half of the absorber layer of the solar cell with $t_{\mathrm{dis}} =$

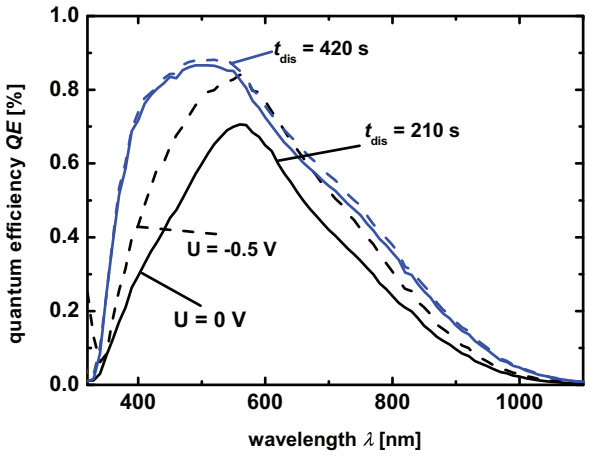

Figure 5.7: Quantum efficiency of two solar cells with increased silane concentration for 180 s after 210 s and 420 s measured with and without 0.5 V reverse bias.

0 s is deposited with a relatively high crystalline volume fraction the V_{oc} of the resulting solar cell is –different to all the other samples– above 700 mV which is typical of an amorphous silicon device.

The smaller thickness of the layer deposited with a t_{dis} of 210 s indicates that the crystalline volume fraction of the topmost part of the layer grown during the disturbance was large enough to maintain the seed function for the growth of a μc-Si:H layer.

The reduced performance of the solar cells with t_{dis} smaller than 1050 s could be explained by the fact that the disturbance represents a barrier for the holes [108]. When the position of the disturbance is moved towards the i/n-interface an increasing number of carriers will be able to reach the p/i-interface.

The probability of the holes to pass the barrier is increased under an applied reverse bias. Measurements of the quantum efficiencies of solar cells with different t_{dis} were carried out to study this effect. In Figure 5.7 the QE of solar cells with a t_{dis} of 210 s and 420 s with and without an external bias in reverse direction are compared. The solar cell deposited with a t_{dis} of 210 s shows very

low performance without an applied reverse bias. With a reverse bias of 0.5 V the quantum efficiency is strongly enhanced over the whole spectral range. The QE of the solar cell with a t_{dis} of 420 s is only improved for long wavelengths by the applied voltage. This difference in QE supports the assumption that the disturbed layer represents a barrier for the holes:

Due to their high absorption coefficient (Figure 2.1) photons with wavelengths in the blue part of the solar spectrum are mainly absorbed in areas close to the p/i-interface whereas homogeneous absorption in the intrinsic layer is assumed for less energetic photons. The QE in the red part of the spectrum is hence improved by the applied reverse bias independent of the position of the disturbance. In the high energy part of the spectrum however the holes are generated close to the p-layer. Hence a larger fraction of the holes is generated between the disturbance and the p-layer for a t_{dis} of 420 s when compared to a solar cell with a t_{dis} 210 s. The extraction of the holes that are generated between the disturbance and the p-layer is not influenced by the barrier. Hence the QE of the solar cell deposited with a t_{dis} of 420 s is improved only in the red part of the spectrum whereas it is increased over the whole spectral range for a t_{dis} of 210 s.

Concerning the applicability of in-situ Raman spectroscopy these results indicate that a disturbance as studied in this section takes place during deposition of an intrinsic μc-Si:H absorber layer it depends on the fraction of the layer that has already been deposited whether or not it is possible to successfully control the process. In this case a successful process control means that state-of-the-art solar cell performance is achieved in spite of the disturbance.

5.2.2 Influence of the Width of the Disturbance

Additionally to the position of a disturbance its duration is expected to impact the negative effect on solar cell performance. As shown in Figure 5.4 the minimum crystalline volume fraction of a layer depends on the duration of the disturbance. To study the influence of these $I_{\mathrm{C}}^{\mathrm{RS}}$ profiles on solar cell performance working devices were fabricated from the p/i layer stacks described by Figure 5.4. In Figure 5.5 it has been shown that the impact of a disturbance on solar cell performance is large for small t_{dis}. To exclude effects originating from a disturbance of the initial phase of deposition SC, disturbances with different durations were

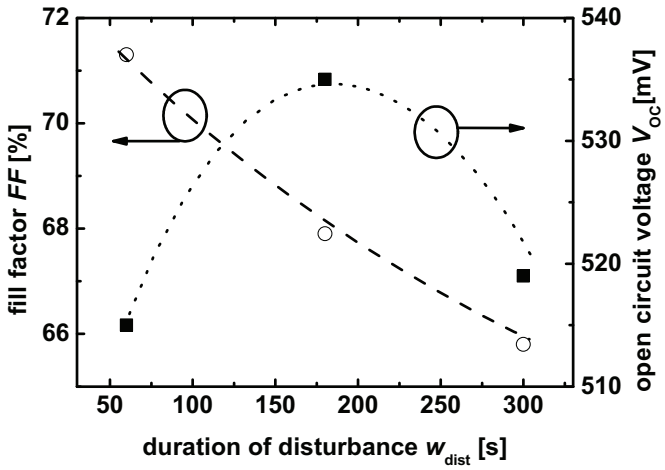

Figure 5.8: Fill factor and open-circuit voltage of solar cells with disturbances in the silane concentration introduced after 1050 s of absorber deposition with durations of 60 s, 180 s and 300 s.

included after 1050 s of deposition, which corresponds to a layer thickness of about 600 nm. Figure 5.8 shows the fill factor and the open-circuit voltages of solar cells deposited with three different w_{dis}. A continuous decrease of the fill factor with increasing w_{dis} is observed. This could be explained by the decrease of the minimum crystalline volume fraction with increasing w_{dis} shown in Figure 5.4. The open-circuit voltage however reaches a maximum for the solar-cell that includes a disturbance of 180 s duration in its intrinsic layer.

As shown in Figure 5.4 a crystalline phase is still present after a w_{dis} of 180 s. Together with a possible recrystallization of the layer after the deposition of predominately amorphous material this means that the electrical properties of the layer are good enough for state-of-the-art solar cell performance. If the w_{dis} is too large and accordingly the crystalline volume fraction is reduced too much the deposited material could provide a barrier for the generated holes and thus the solar-cell performance is decreased.

5.3 Transmission Electron Microscopy of Layers Deposited with a Disturbance

Transmission electron microscopy (TEM) is applied to obtain information about structural properties of solids on small length scales. Application of TEM for studies of μc-Si:H is discussed in References [22, 34]. The TEM specimens were prepared using a dual-beam scanning electron microscopy and focused ion beam system. Bright-field (BF), dark-field (DF) images and selected area electron diffraction (SAED) patterns were used to study the microstructure of samples in cross-section. Only undeflected electrons are recorded in BF images were crystallites appear as dark regions, since a part of the electrons is removed from the beam by Bragg reflections in these areas. In the case of DF images only scattered electrons are collected since the directly transmitted beam is blocked and crystallites of the same orientation appear as bright areas. SAED patterns allow to determine whether a layer is microcrystalline or amorphous.

To get additional insight into the structure of films deposited with a disturbance in *SC*, cross sectional TEM images were recorded. Figures 5.9 a) and b) show the bright and dark field images and selected area electron diffraction patterns at two positions of a film deposited with a t_{dis} of 1050 s and a w_{dis} of 600 s. As seen in Figure 5.8 the FF and V_{oc} of the associated solar cell are 65 % and 520 mV respectively. These solar cell characteristics are slightlly lower than those of the standard cells described in Table 2.1. The contrast between featureless amorphous regions and the structures shown in the crystalline parts of the Bf and DF images indicate that a crystalline layer grows on the ZnO substrate. After a layer thickness of roughly 600 nm a predominately amorphous layer develops. The interface between the μc-Si:H fraction and the a-Si:H part contains sharp crystalline spikes, which extend into the amorphous part of the layer. The spikes could be attributed to local epitaxial growth on the underlying crystallites.

After a predominately amorphous layer with a thickness of roughly 200 nm is deposited μc-Si:H growth starts with an extended incubations phase in which cone-like μc-Si:H crystals develop. Some of the earlier mentioned sharp spikes seem to interconnect with the tips of the μc-Si:H cones and hence act as starting points for the μc-Si:H incubation. Towards the top of the layer a predominately

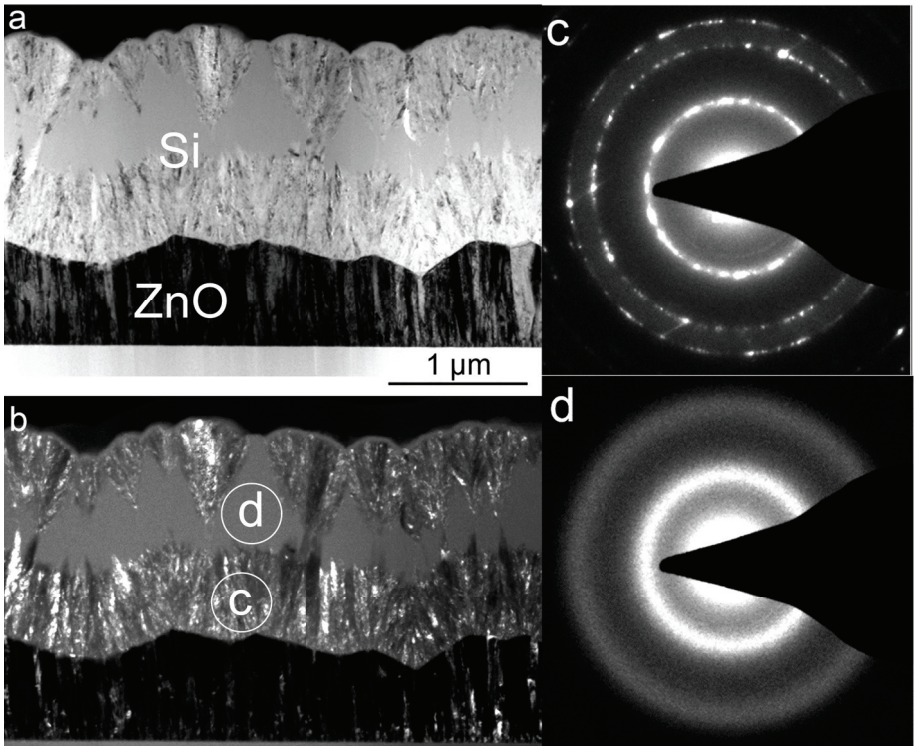

Figure 5.9: a) Bright field b) dark field image of a μc-Si:H layer deposited on rough ZnO with a disturbance in the silane concentration. c, d) Show selected area electron diffraction patterns obtained at the positions marked in (b). The lack of crystalline reflections in c) confirm the amorphous structure of Si.

microcrystalline layer develops.

The in-situ Raman measurements shown in Figure 5.4 agree with the observations made in the TEM images. In the Raman measurements a relatively fast but not instant decrease of the crystalline volume fraction was observed after an increase of SC during deposition. This agrees with the relatively sharp transition from μc-Si:H growth to a-Si:H material and the inclusion of crystalline spikes shown in Figure 5.9. The thickness of the μc-Si:H layer corresponds to a t_{dis} of 1050 s before which roughly 610 nm are deposited at a R_{d} of 5.8 Å/s, which was estimated from the modulation of the Stokes Raman intensity. An almost completely amorphous film was observed during the in-situ Raman measurements towards the end of the disturbance. This corresponds to the thick, predominately amorphous layer, shown in the TEM image. The thickness of the amorphous layer of 200 nm, extracted from the TEM images, is similar to the expected 175 nm at a w_{dis} of 600 s.

Due to the relatively large d_{inf} the results of the in-situ Raman measurement describe an average of the probed volume and hence the sharp transition shown in the TEM images can not be identified. Nevertheless the difference between the relatively low rate of increase of $I_{\mathrm{C}}^{\mathrm{RS}}$ at the end of the disturbance and the faster decrease at the beginning observed in-situ correspond to the cone-like incubation after the decrease of SC and the sharp drop of the crystallinity at t_{dis} observed in the TEM images. By determining the local crystalline volume fraction from the TEM measurements and averaging over layer thicknesses that correspond to d_{inf}, on larger volumes than shown in Figure 5.9, the TEM results are expected to reproduce the Raman measurements.

The relatively high fill factor of the solar cell deposited with a w_{dis} of 600 s might be explained by the interconnection of the crystallites observed at the top of the TEM image with the part of the layer that has been deposited previous to the disturbance. Nevertheless it is rather surprising to obtain relatively good solar cell performance when an absorber layer as shown in Figure 5.9 is included into a device. It can be speculated that the interconnection of the crystallites grown before and after the disturbance act as percolation paths for the charge carrier extraction. Hence it might be possible to determine a breakdown criterion, based on further TEM studies.

5.4 Conclusion

In this section it was shown that the impact of disturbances in the gas flow on a growing layer can be detected using in-situ Raman spectroscopy. For the studied deposition system and amplitude of the disturbance it takes about 10 s for the plasma composition to stabilize after the process gas flow is changed. A relatively fast reaction of the growing film has been observed in-situ. In contrast to the plasma composition the layer growth does not stabilize on the studied timescales of several minutes. The fraction of the layer that is affected and the magnitude of the decrease of solar cell performance depends on the position of the disturbance:

If it starts relatively close to the p/i-interface the layer growth is affected much longer than the gas flow is changed and the solar cell performance is strongly degraded. State-of-the art solar cell performance was achieved for disturbance in later stages of absorber layer deposition with durations of 180 s or less.

The depth dependent information about the crystalline volume fraction that was determined ex-situ using transmission electron microscopy showed an excellent correlation to the in-situ data. The formation of an amorphous fraction in the layer as a result of an increase of the silane concentration was found with both measurement techniques. A difference between the rates of decrease and increase of the crystalline volume fraction at the beginning and end of a disturbance was observed in-situ. This difference corresponds to the cross sectional information obtained with transmission electron microscopy.

An application of in-situ Raman spectroscopy as the basis for an active process control is possible since changes of the growing layers were observed before they resulted in a decline of solar cell performance. Due to the large amorphous fraction, that is included into μc-Si:H layers with a large w_{dis} the light induced degradation data, that has not yet been obtained, of solar-cells deposited with a disturbance of SC is expected to differ from that of standard μc-Si:H solar cell.

6 Influence of the Deposition Parameters on the Film Temperature

The film temperature is known to be a critical process parameter [111, 112, 72, 113]. Using in-situ Raman spectroscopy the temperature of a growing film can be directly determined. In this chapter pulsed plasma deposition is described as a method to improve the signal-to-noise ratio of in-situ Raman spectroscopy to a level that enables accurate temperature measurements. The characteristics of the film temperature in two deposition regimes is compared and a method to inhibit the observed increase of the film temperature during deposition is discussed.

6.1 Calibration of the Temperature Measurements

To perform temperature measurements with the help of Raman spectroscopy the calibration constant C_{Ram} that –according to equation 2.9– depends on the measurement setup and the laser wavelength is determined. The calibration constant is evaluated from Raman spectra recored on a previously deposited 1 μm thick μc-Si:H film on a ZnO substrate at known temperatures. Before each calibration measurement the sample is heated inside the deposition chamber at vacuum conditions until an equilibrium temperature is reached. Under these conditions it is assumed that the glass substrate and the silicon film are at the same temperature. The temperature of the glass substrate is determined with a pyrometer using the experimental setup described by van den Donker *et al.* [50]. By correlating the temperature measured with the pyrometer to the Stokes/anti-Stokes intensity ratio (R_{T}) the calibration constant C_{Ram} is estimated. Since the temperature

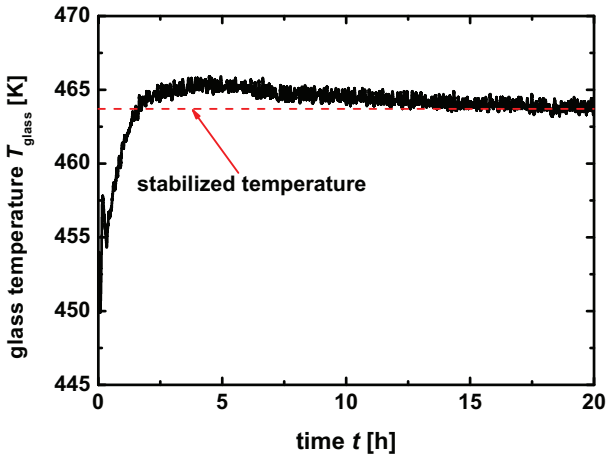

Figure 6.1: Glass temperature after transfer of the substrate into the deposition chamber measured with a pyrometer as a function of time.

(T_{heat}) of the substrate heater is the process parameter that is actively controlled it is correlated to the temperature (T_{glass}) determined with the pyrometer.

Figure 6.1 shows the glass temperature that was measured under vacuum conditions after a substrate is moved into the deposition chamber for a heater temperature of 573 K. The stabilized T_{glass} shown in the Figure of 463 K is obtained after more than 15 hours of temperature equilibration. The difference between heater and glass temperature is typical for the studied deposition system. The main reason for the temperature difference is radiative heat transfer –which is the major heat transfer mechanism in vacuum– from the heater to the glass substrate.

To allow an estimation of the substrate temperature as a function of T_{heat} the corresponding T_{glass} was determined in the temperature regime relevant for μc-Si:H deposition. Before each measurement the temperature was stabilized under vacuum conditions until the equilibrium temperature was reached. Figure 6.2 shows the relation between T_{heat} and T_{glass}. Using the data shown in Figure 6.2 a change of the heater temperature can be correlated to the expected temperature of the substrate. At process conditions the temperature difference between heater

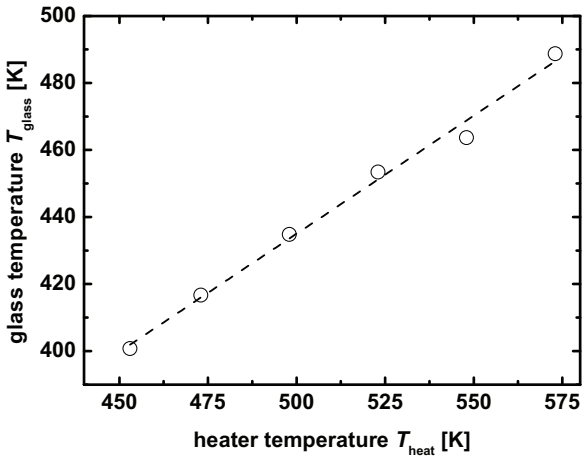

Figure 6.2: Temperature of a glass substrate determined with a pyrometer as a function of the heater temperature.

and glass substrate is different due to an increase of the heat transfer by convection in the process gas atmosphere. Due to the relatively long stabilization time of the temperature the calibration measurements of the Raman intensity ratio were carried out in vacuum conditions.

To determine C_{Ram} Raman spectra at different T_{heat} were recorded under vacuum conditions for heater temperatures ranging from 50°C to 300°C . The glass temperature was calculated using the results obtained in Figure 6.2. A linear correlation between the logarithm of the the stokes/anti-stokes intensity ratio (R_{T}) and the reciprocal T_{heat} –as expected regarding Equation 2.9– is observed in Figure 6.3. From these measurements C_{Ram} is determined as 1.19 ± 0.09.

In contrast to T_{heat} the temperature (T_{film}) measured by Raman spectroscopy reflects the film temperature independent of the process conditions.

A change of the film temperature during deposition is determined from an increase or decrease of the stokes/anti-stokes intensity ratio. To estimate the relative change of R_{T} at a temperature increase $\Delta\, T$, the ratio of R_{T} and $R_{T+\Delta\, T}$ is determined in Equation 6.1. With this result the minimum signal-to-noise ratio

at which it is possible to identify a temperature increase ΔT is estimated

$$R_{\mathrm{T}}/R_{\mathrm{T+\Delta T}} = \frac{\exp(\frac{\hbar\omega_0}{kT})}{\exp(\frac{\hbar\omega_0}{k(T+\Delta T)})} = \exp(-\frac{\hbar\omega_0}{k} \cdot \frac{1}{T \cdot (T+\Delta T)}). \tag{6.1}$$

The standard heater temperature set during the deposition of a microcrystalline i-layer is 473 K. From Figure 6.2 the corresponding film temperature is estimated to about 417 K. According to Equation 6.1 an increase of 10 K at this initial temperature results in a change of R_{T} of about 4 %. In Figure 4.2 an example of an in-situ spectrum obtained during the deposition of a μc-Si:H film is shown. With the relatively poor signal-to-noise-ratio shown in the figure it is not possible to detect small temperature increases with high precission.

An increase of the signal-to-noise ratio without elongating the individual measurement intervals can be achieved by excluding the plasma emission completely from the collected spectra. This method is described in the following section.

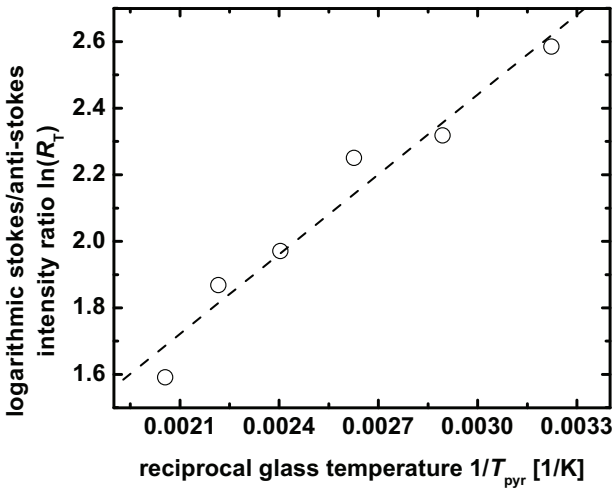

Figure 6.3: Stokes/anti-Stokes intensity ratio of a μc-Si:H film as a function of the heater temperature. From this measurement the proportionality constant C_{Ram} used to calibrate Raman temperature measurements is determined.

6.2 Pulsed Plasma Deposition

A straight forward way to obtain Raman spectra with a reduced noise level is to increase the integration time. Figure 4.1 and Equation 4.1 show that with the measurement routines described so far this leads to a strong reduction of the temporal resolution since the integration time of the plasma background signal would also have to be increased. By turning off the rf-input power during the laser pulses and avoiding contributions of the plasma after-glow it is possible to record Raman spectra in-situ without a plasma background signal. The duration of the plasma after glow and the influence of a periodic modulation of the input power on solar cell performance is described in this section.

6.2.1 Duration of the Plasma After-Glow

Pulsed plasma deposition is realized by synchronizing the rf-generator used to power the plasma with the chopper that is modulating the laser. Since the laser pulses are synchronized to the illumination of the CCD camera (see Section 3.2) no plasma light is recorded with the laser pulses. Figure 6.4 shows the phase between the two choppers. An afterglow of the plasma that contributes to the measured spectra is expected [114, 115, 116, 117]. Due to the finite life times of excited species and free electrons in a plasma light is emitted after the power input of the plasma is switched off. The optical emission of the plasma is hence composed of a steady state signal during the plasma on phase and the afterglow.

To prevent the light emitted during the afterglow from entering the spectrometer the duration (t_{spec}) during which light can enter the spectrometer has to be shorter than the plasma off time (t_{off}). Hence it is possible to integrate the Raman signal for a long time during pulsed plasma deposition without having to record and subtract a plasma background spectrum. To minimize the difference between t_{off} and t_{spec} and thus maximize the Raman signal the time (t_{glow}) the plasma emits light after the power is switched off is determined. In Figure 6.5 the schematical time course of an experiment that enables the determination of t_{glow} is shown. The total dark time (t_{dark}) of the plasma at a given t_{off} is estimated by changing the phase between t_{spec} and t_{off}:

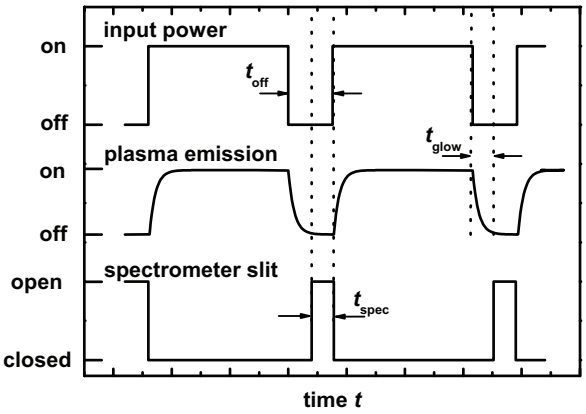

Figure 6.4: Time course of the input power, the light emission and the CCD exposition during pulsed plasma deposition. The open time of the spectrometer slit (t_{spec}), the plasma off time (t_{off}) and the afterglow time (t_{glow}) of the plasma are indicated.

The time interval during which light enters the spectrometer is shifted towards the start of the plasma off time until a plasma signal is detected. The same procedure is repeated while shifting t_{spec} towards the end of t_{dark}. Hence it is possible to determine t_{glow}

$$t_{\mathrm{glow}} = t_{\mathrm{off}} - t_{\mathrm{dark}}. \tag{6.2}$$

The determined after-glow time represents the detection limit at a given integration time and not an absolute constant. If the integration time is changed strongly a new t_{glow} has to be determined. At a pulse frequency of 423 Hz the plasma off time –corresponding to the laser pulse length– is 210 μs. This results in a plasma on time (t_{on}) of 2.15 ms. Hence the duty cycle δ of the plasma which is defined in Equation 6.3 is about 91 %.

$$\delta = \frac{t_{\mathrm{on}}}{t_{\mathrm{on}} + t_{\mathrm{off}}} \tag{6.3}$$

With the use of an oscilloscope the time shift of t_{spec} between the two positions indicated in Figure 6.5 is determined. From these t_{dark} is estimated as 145 μs $\pm$

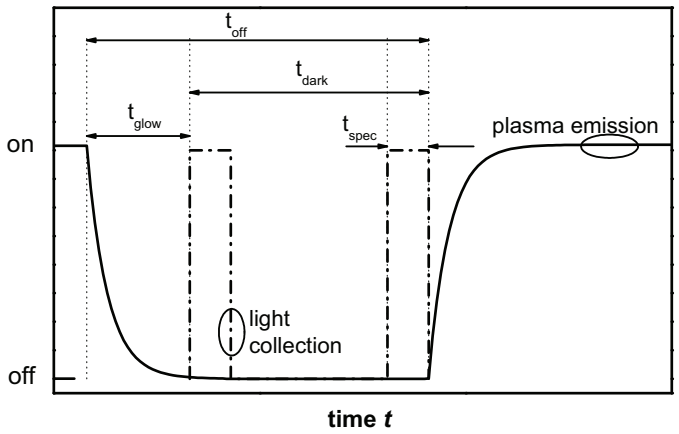

Figure 6.5: Light collection during a plasma off phase of a duration t_{off} in pulsed plasma deposition used to determine the after glow time (t_{glow}) of the plasma. The exposure time of the CCD camera (t_{spec}) and the total dark time (t_{dark}) of the plasma are indicated.

5 μs. With the known t_{off} the duration of the plasma after glow is estimated as 65 $\mu\mathrm{s} \pm 5$ μs. To guarantee that no detectable plasma light is part of the Raman signal t_{spec} is reduced to 120 μs at a plasma off time of 210 μs.

6.2.2 Influence of a Pulsed Plasma on Layer Growth

Aim of the in-situ measurements, performed with pulsed plasma deposition, is to draw conclusions that are also valid for a cw plasma. Apart from a reduction of the average power that is coupled into the plasma the modulation of the input power can lead to more severe changes in the composition of the charged particles inside a discharge. Hence the modulation of the rf-power can either result in a decrease or an increase of the deposition rate at constant average power [118, 119] depending on the applied deposition conditions. The change of deposition rate is explained by changes of the electron energy distribution and the radical production and transport inside the plasma at each re-ignition. It has

pressure [Torr]	**cw R_d [nm/s]**	**pulsed R_d [nm/s]**	**dep. ratio v_{rates}**
10	0.46	0.43	0.93
18	0.41	0.44	1.02

Table 6.1: Deposition rate R_d during cw and pulsed deposition and ratio v_{rates} between pulsed and cw deposition rates for pressures of 10 Torr and 18 Torr. The duty cycle of the pulsed deposition is about 91 % at a modulation frequency of 420 Hz.

also been reported that a large number of high energy electrons is present at the time of the plasma switch on which changes the composition of the plasma [117].

The high pressures used for μc-Si:H deposition result in a large reduction of the deposition rate in plasmas modulated by square waves whose frequencies are in the same order as the 420 Hz used during the Raman measurements [120]. The duty cycle during the pulsed Raman measurements is about 91 %, which is larger than the 50 % of a square wave. Hence the large duty cycle during the in-situ Raman measurements is expected to result in a moderate reduction of R_d and minor changes in the growth mechanisms under the assumption of a fast stabilization of the plasma after each reignition.

To study the influence of a modulated plasma on layer growth the R_d of films deposited with and without a modulation of the input power was compared. Table 6.1 lists the growth-rate ($R_{d,cw}$) obtained during continuous plasma deposition, the deposition rate ($R_{d,pulse}$) for pulsed plasma deposition and the ratio (v_{rates}) between $R_{d,cw}$ and $R_{d,pulse}$ for the 10 Torr and 18 Torr growth regimes. These data were obtained by determining the layer thickness after pulsed and cw-depositions with the help of a profilometer. The layers used for this study were deposited according to Table 3.2.

The duty cycle of the plasma (91 %) and v_{rates} of the deposition at 10 Torr show a similar value which is expected from the earlier studies mentioned above. For the deposition at 18 Torr a slight increase of the R_d is observed during pulsed plasma deposition. Since v_{rates} is relatively close to unity in both regimes it is assumed that the influence of the plasma off periods on the deposition is small.

Figure 6.6 shows the Raman spectrum of a μc-Si:H film obtained during pulsed plasma deposition, compared to a reference spectrum measured during a

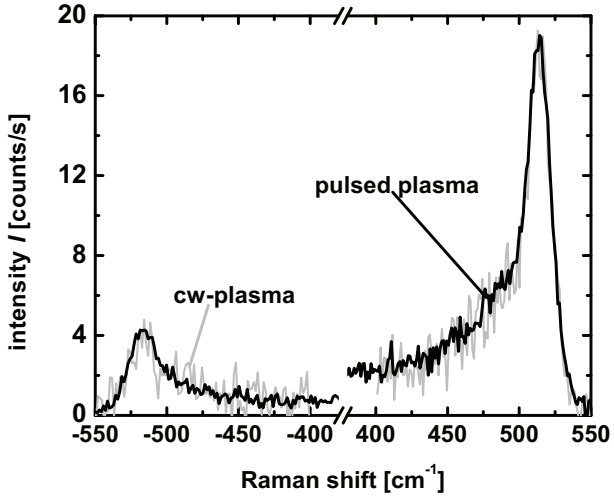

Figure 6.6: Raman shift recored during the pulsed plasma deposition of a μc-Si:H film compared to a spectrum recorded during a cw-plasma.

cw-plasma. It can be seen that the signal-to-noise ratio is increased drastically during pulsed plasma deposition which enables a better evaluation of the Stokes to anti-Stokes intensity ratio.

6.3 Determination of the Film Temperature in Different Growth Regimes

A plasma induced heating of the substrate has been reported previously [121, 50]. The plasma heating is especially important when considering the high input powers and deposition rates that are applied during the growth of μc-Si:H. Several mechanisms e.g. ion bombardment, the deposition of chemical energy, radiative heating and heat transfer from neutral gas molecules are contributing to the plasma induced heating of the substrate. In this section the temperature increase at a constant deposition rate and varying input powers and pressures is studied

integration time [s]	20
Number of Accumulations	5
start Stokes/AntiStokes Integration [cm^{-1}]	410
end Stokes/AntiStokes Integration [cm^{-1}]	560

Table 6.2: Integration time, number of accumulations, start and end points of the Stokes/Anti-stokes intensity integration applied during Raman temperature measurements.

by Raman spectroscopy. All the temperature measurements described in this section were carried out with the pulsed plasma parameters summarized in Table 3.3 and a temporal resolution of 100 s.

6.3.1 Observation of the Film Temperature at Constant Deposition Parameters

Two of the deposition regimes described in Table 3.2 are suitable to study a possible temperature increase caused by the plasma. It was shown in Section 3.4 that at pressures of 10 Torr and 18 Torr homogeneous films are deposited at growth rates of about 5 Å/s with different input powers. The measurement parameters used to determine T_{film} during the depositions are summarized in Table 6.2. The ratio of Stokes and anti-Stokes intensity is calculated from the integrated intensities of the peaks with the integration boundaries shown in Table 6.2. Two individual linear baselines with assumed zero Raman intensities at $\pm$ 400 cm^{-1} and $\pm$ 550 cm^{-1} were subtracted from the Stokes and anti-Stokes parts of the spectra before integration.

Figure 6.7 shows the film temperature obtained during the deposition and linear fits. The heater temperature was set to 200°C during both depositions and held constant. A relatively large scatter of the data is shown for both measurements. Initial film temperatures of roughly 180°C are determined for both depositions. Despite the large scatter of data a small increase of roughly 50°C is observed during the low pressure deposition. During the 18 Torr deposition a more pronounced increase of T_{film} of roughly 180°C is observed.

The initial temperature in both cases is closer to the heater temperature than

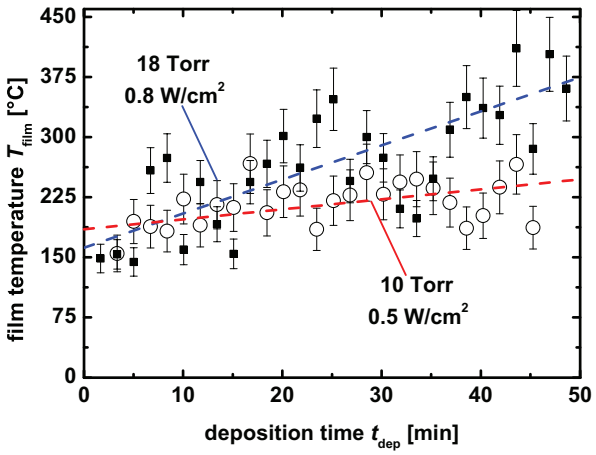

Figure 6.7: Film temperature measured during the deposition of two intrinsic layers with different input powers and pressures at growth rates of roughly 5 Å/s. The dotted lines are guides to the eye.

suggested by Figure 6.2. This is explained by the fact that during the measurements shown in Figure 6.2 no gas was inside the process chamber whereas the data shown in Figure 6.7 was obtained under process conditions at pressures of 10 Torr and 18 Torr. The temperature equilibration step at 5 Torr Ar pressure, described in Section 2.2, was carried out at an identical T_{heat} before both deposition. Hence –within the scatter of data– similar initial temperatures are expected and observed. Two effects are suspected to cause the significant difference in the temperature characteristics shown in Figure 6.7:

- At a higher pressure the heat transfer by conduction is more efficient. This leads on the one hand to a smaller temperature difference between the heater and the substrate and on the other hand to an improved thermal conductance of the neutrals inside the plasma.

- Due to the higher input power the gas temperature in the plasma is increased [122] which –together with the improved heat conductance– might also lead to the higher substrate temperature.

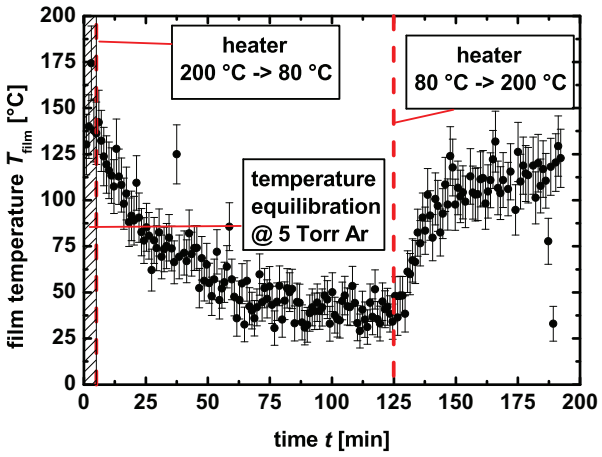

Figure 6.8: Cooling and heating of a μc-Si:H layer at a pressure of 18 Torr by a control of the heater temperature with process gas flow and without plasma.

6.3.2 Controlling the Film Temperature by adjusting the External Heating

A way to stabilize the film temperature at high input power and pressure over the whole extend of a deposition is to actively control the temperature of the substrate heater. To study the reaction of T_{film} to a change of T_{H} without a plasma the temperature of a previously deposited film was determined at the deposition pressure of 18 Torr.

Figure 6.8 shows the development of the temperature of a 1 μm thick μc-Si:H film at a change of the heater temperature from 200°C to 80°C without a plasma. The obtained scatter of data is much lower than observed in Figure 6.7. The improved accuracy was achieved by removing the chopper in front of the spectrometer (see Figure 3.1) –which is possible since no plasma light was present– and by increasing the integration times. Previous to changing the heater temperature the standard temperature equilibration step described in Section 2.2 under 5 Torr Argon atmosphere has been carried out. It can be seen that after

the heater is switched to 80°C the temperature of the film starts to decrease. The temperature increase shown in Figure 6.7 was obtained during a deposition time of 50 min. A decrease of T_{film} by about 90°C from an initial temperature of roughly 140°C is observed during the first 50 min in Figure 6.8. A stable minimum T_{film} is obtained after roughly 75 min. After 125 min T_{heat} is increased to 200°C. This is followed by a fast increase of $T_{\mathrm{film}}$by about 60°C within 20 min and a slower increase by 20°C during the last 50 min of the measurements.

The low observed cooling rate is due to the inertia of the heater. Hence it is not expected that the large temperature increase at a deposition pressure of 18 Torr indicated by Figure 6.7 can be completely counteracted by switching off the substrate heater.

Since no active cooling of the heater was available the film temperature during deposition is stabilized by reducing T_{heat}. In Figure 6.9 the temperature increase during depositions carried out with and without a reduction of T_{heat} is compared. In one case the heater temperature was constant in the other it was switched to 80°C after plasma ignition. The initial temperature of the films is similar within the scatter of data. The temperature of the film deposited with non-constant T_{heat} increases slightly from 200°C to about 225°C which is much less than the increase of roughly 180°C observed without a change of T_{H}.

This result shows that it is possible to reduce the plasma induced temperature increase at high input powers and pressures by actively controlling T_{heat}. From the measurements shown in Figure 6.8 performed without a plasma a maximal reduction of T_{film} of 90°C was expected as a result of the reduced T_{heat}. According to Figure 6.7 a temperature increase of roughly 180 °C is expected during a deposition in the high-pressure regime. Hence it was not assumed that it is possible to stabilize the temperature to the extend indicated by Figure 6.9. The difference in the observations could be due to the large scatter of the data that needs to be reduced to allow definite conclusions.

6.4 Conclusion

It was shown that it is possible to determine the temperature of a growing film in-situ by Raman spectroscopy whereas the temperature of the glass substrate was the best obtainable estimate for this important process parameter previously.

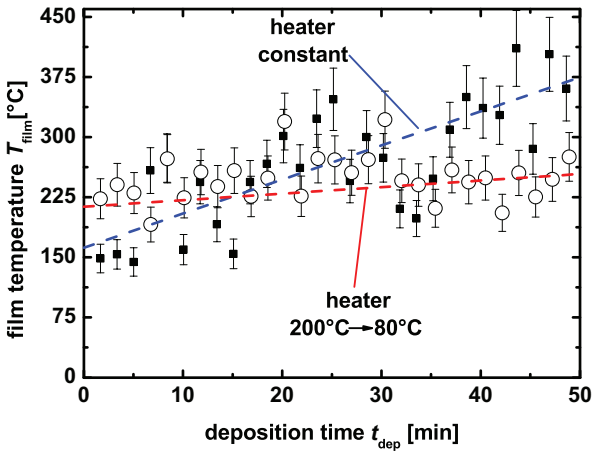

Figure 6.9: Film temperature determined during two depositions carried out under the same conditions with and without a control of the external heater

Due to pulsing the input power the Raman spectra were recorded without any background contribution by the plasma emission. This enables a high temporal resolution at low signal to noise level.

The scatter and the uncertainty of the obtained temperatures is relatively high. Despite this two growth regimes were distinguished based on the temperature increase during deposition. By estimating the absolute extend of the temperature increase obtained in-situ by Raman spectroscopy it was possible to counteract by controlling the external heating and obtain a more constant temperature throughout the deposition than achieved under constant conditions.

7 Summary & Outlook

The aim of this work was the development of an experimental setup that enables the in-situ determination of the Raman crystallinity and the film temperature during the growth of microcrystalline silicon thin films and solar cells. This was realized successfully by a novel design of a showerhead electrode, which enables direct optical access to the growing film under normal incidence. With this setup the Raman crystallinity was measured with a very good temporal resolution under industrially relevant process conditions. Due to the higher demands on the signal-to-noise-ratio for measurements of the film temperature, pulsed plasma deposition was applied. In the following the experimental results are summarized and an outlook on possible future studies possible with this novel setup is given.

In Chapter 3 of this work an experimental setup inside a parallel plate plasma-enhanced chemical vapor deposition system, which enables optical access to central regions of a growing film under normal incidence was developed. The setup was optimized to enable a large optical acceptance angle at a minimal disturbance of the surface of the rf-electrode.

The effect of the feed through on the homogeneity of microcrystalline silicon films strongly depends on the deposition regime. Hence electrical shields were developed to enable almost undisturbed depositions under various conditions. It was shown that with these shields the homogeneity of the growing films is strongly enhanced at sufficient optical transmission.

Due to the high required temporal resolution required in an in-situ experiment, the signal-to-noise ratio was maximized by pulsing the laser radiation. It was found out that with state-of-the-art technology the demand of an in-situ Raman experiment can be met best by a laser with a wavelength of 532 nm.

The pulsed illumination minimizes the temperature increase caused by the high power laser. The interconnection between film temperature and laser param-

eters was studied by experiment and estimated with the help of a finite element simulation. The laser parameters for a minimal impact of the in-situ measurements on film growth were determined.

Apart from in-situ Raman spectroscopy the newly designed electrode enables the application of various other characterization techniques during thin-film growth. An interesting example, which will be applied in the future, is spatially resolved optical emission spectroscopy. By applying a confocal geometry the plasma composition can be determined as a function of the distance to the surface of the growing layer.

The novel setup can also be used to change the properties of a growing film by illumination during the deposition. An interesting example of an experiment like this is the laser induced crystallization of a growing film. By modifying the optical path a larger area of the sample than before can be illuminated.

Chapter 4 deals with in-situ measurements of the Raman crystalline volume fraction of growing layers. The interrelation between the measurement parameters that determine the temporal resolution and the intensity of the collected light is studied. Background contributions to the measured Raman signals were identified and a routine to remove parts of the signal originating from the underlying substrate was developed.

To estimate the accuracy of the in-situ measurements, the sources of error involved in the calculation of the in-situ Raman crystallinity were identified. A procedure to estimate the magnitude of the uncertainty in the Raman crystallinity was developed.

In-situ Raman measurements on a μc-Si:H layer were carried out with a minimal temporal resolution of about 17 s. At a typical growth rate of 5 Å/s this means that as little as 8.5 nm are deposited during one measurement interval. In-situ measurements of the crystalline volume fraction were compared to depth dependent measurements obtained after the deposition. An excellent agreement was found. Since the ex- and in-situ measurements were performed at different positions on the sample, it was concluded that the influence of the in-situ Raman setup on film growth is very low. A possible, hydrogen induced reconfiguration of the topmost fraction of a growing layer, which is suspected by some models for the growth of microcrystalline silicon, has not been observed.

To study the initial phase of deposition with a high depth resolution as well as a high precision of the crystalline volume fraction, measurements at a reduced growth rate were carried out. It was shown in-situ that the crystalline volume fraction, which develops during the initial stage, depends on the substrate. An initial decrease and a subsequent gradual increase of the crystalline volume fraction during the first stage of deposition were observed for material deposited on highly crystalline p-layers. By actively controlling the deposition conditions during this phase, it was possible to improve the homogeneity of the crystalline volume fraction in growth direction during the initial phase of deposition.

These first experiments show that an active control of the evolution of the Raman crystallinity based on the results obtained in-situ is possible. On the basis of these results it is expected that well-defined profiles of the Raman crystallinity based on in-situ measurements can be implemented in microcrystalline layers. Hence it might be possible to determine optimum profiles for solar cell performance and to transfer these results to deposition systems without an in-situ measurement setup. It will also be interesting to observe how the growth of the microcrystalline absorber layer in a tandem solar-cell is influenced by the underlying (intermediate-) layer.

The combination of ex-situ measurements with in-situ Raman spectroscopy might provide a means to get a better understanding of the growth mechanisms that are involved during the deposition of microcrystalline silicon. A reduced penetration depth, compared to that achieved with 532 nm light, will be beneficial for such a study in order to obtain information on a smaller fraction of the growing film. With the reduced penetration depth it might be possible to detect differences in the crystalline volume fraction between the growing layer and the film after deposition.

In Chapter 5 the applicability of in-situ Raman spectroscopy as the basis of an active process control is tested. Layers and solar cells with disturbances of the gas flow during deposition were grown. The influence of the duration and the point in time of a disturbance with a fixed amplitude on the plasma, and as a result of that on the crystalline volume fraction of the layer were studied. It was found that the disturbance of the layer growth was detected in-situ at an early stage.

By studying the effect of disturbances on solar-cell performance, it was found that an active process control guided by in-situ Raman spectroscopy is fast enough to maintain state-of-the-art solar cell performance. A strong correlation of the position of the disturbance, with respect to the p/i-interface, to device performance was detected.

A fluctuation of the process gases with fixed amplitude was studied. To enable a precise control of the layer properties, the feed-back of deposition parameters on the growing film has to be studied in more detail. This will open up the possibility of compensating process instabilities by adapting deposition parameters during the growth of a layer.

Chapter 6 deals with the determination of the film temperature with the help of in-situ Raman spectroscopy. This parameter is suspected to have a large impact on the properties of a growing film. Previously a direct measurement of the film temperature in a parallel plate PECVD system was not possible.

Calibrations that allow the correlation of the applied heater temperature to the Stokes/anti-Stokes scattering intensity ratio were carried out. It was found that an improvement of the signal-to-noise ratio of the in-situ measurements is necessary to obtain an accurate measure of the relevant temperature fluctuations.

Pulsed plasma deposition was identified as a method of maintaining a high temporal resolution and simultaneously increasing the signal-to-noise ratio. With this deposition method Raman spectra without contributions of the plasma light were recorded.

Measurements in two different growth regimes with similar growth rates were performed. The two regimes differ by their deposition pressure and input power. Even though the scatter of the obtained data was relatively large, a large increase of temperature during deposition was observed in the high pressure/high power case. In the other case the detected temperature increase was much less pronounced.

To estimate the influence of the external heater on the film temperature under process conditions without a plasma, a reference experiment was carried out. The obtained results were used to counteract the temperature increase that was observed in the high power regime by actively controlling the external heater. Thus it was possible to stabilize the film temperature during the entire deposi-

tion.

The uncertainty and the scatter of the obtained film temperature during pulsed plasma deposition is still relatively large. Optimizations in the measurement procedure, which enable a greater accuracy, have to be carried out to improve the significance of the temperature measurements. With an improved accuracy the novel measurement setup will enable a study of the interdependence of deposition rate, excitation frequency and input power with the temperature increase in a growing film.

Bibliography

[1] Department of Economic United Nations and Population Division Social Affairs. World Population Prospects: The 2010 Revision, CD-ROM Edition. 2011.

[2] Renewables 2011 global status report, 2011.

[3] United Solar. http://www.uni-solar.com/2011/07/united-solar-reaches-16-3-efficiency-with-nano-crystalline% E2% 84% A2-technology/, 2011.

[4] F. Hottier and J.B. Theeten. Surface-Analysis During Vapor-Phase Growth. *Journal of Crystal Growth*, 48(4):644–654, 1980.

[5] B. Drevillon. A Spectroscopic Ellipsometry Study of the Nucleation and Growth of Plasma-Deposited Amorphous-Silicon. *Thin Solid Films*, 130(1-2):165–170, 1985.

[6] R.W. Collins. Insitu Ellipsometry Study of the Growth of Hydrogenated Amorphous Silicon by Glow-Discharge. *Journal of Vacuum Science & Technolgy A-Vacuum Surfaces and Films*, 4(3, Part 1):514–517, May-Jun 1986.

[7] N. Layadi, P. Roca i Cabarrocas, B. Drevillon, and I. Solomon. Real Time Spectroscopic Ellipsometry Study of the Growth of Amorphous and Microcrystalline Silicon Thin-Films Prepared by Alternating Silicon Deposition and Hydrogen Plasma Treatment. *Physical Review B*, 52(7):5136–5143, Aug 15 1995.

[8] J.H. Koh, Y.H. Lee, H. Fujiwara, C.R. Wronski, and R.W. Collins. Optimization of hydrogenated amorphous silicon p-i-n solar cells with two-step i layers guided by real-time spectroscopic ellipsometry. *Applied Physics Letters*, 73(11):1526–1528, Sep 14 1998.

[9] R.W. Collins, A.S. Ferlauto, G.M. Ferreira, C. Chen, J. Koh, R.J. Koval, Y. Lee, J.M. Pearce, and C.R. Wronski. Evolution of microstructure and

phase in amorphous, protocrystalline, and micro crystalline silicon studied by real time spectroscopic ellipsometry. *Solar Energy Materials and Solar Cells*, 78(1-4):143–180, Jul 2003.

[10] G. Dingemans, M.N. van den Donker, D. Hrunski, A. Gordijn, W.M.M. Kessels, and M. C. M. van de Sanden. In-Situ Film Transmittance Using the Plasma as Light Source: A Case Study of Thin Silicon Film Deposition in the Microcrystalline Growth Regime. In *Proceedings of the 22nd EPVSEC Milan 2007*, 2007.

[11] T. Meier, M. Merdthanova, U.W. Paetzold, S. Muthmann, A. Mueck, R. Schmitz, and A. Gordijn. In Situ Current Determination of a-Si/μc-Si Tandem Solar Cells via Transmission Measurements During Silicon PECVD. *IEEE Journal of Photovoltaics*, 2012. DOI: 10.1109/JPHOTOV.2011.2179413.

[12] F.J. Kampas and R.W. Griffith. Optical Emission Spectroscopy - Towards the Identification of Species in the Plasma Deposition of Hydrogenated Amorphous-Silicon Alloys. *Solar Cells*, 2(4):385–400, 1980.

[13] C. Bohm and J. Perrin. Spatially Resolved Optical-Emission and Electrical-Properties of SiH4 RF Discharges at 13.56 MHz in a Symmetrical Parallel-Plate Configuration. *Journal of Physics D-Applied Physics*, 24(6):865–881, Jun 14 1991.

[14] L.H. Guo, M. Kondo, M. Fukawa, K. Saitoh, and A. Matsuda. High rate deposition of microcrystalline silicon using conventional plasma-enhanced chemical vapor deposition. *Japanese Journal of Applied Physics Part 2 - Letters*, 37(10A):L1116–L1118, Oct 1 1998.

[15] Y. Fukuda, Y. Sakuma, C. Fukai, Y. Fujimura, K. Azuma, and H. Shirai. Optical emission spectroscopy study toward high rate growth of microcrystalline silicon. *Thin Solid Films*, 386(2):256–260, May 15 2001.

[16] L. Feitknecht, J. Meier, P. Torres, J. Zurcher, and A. Shah. Plasma deposition of thin film silicon: kinetics monitored by optical emission spectroscopy. *Solar Energy Materials and Solar Cells*, 74(1-4):539–545, Oct 2002.

[17] J.K. Rath, R. H. J. Franken, A. Gordijn, R. E. I. Schropp, and W. J.

Goedheer. Growth mechanism of microcrystalline silicon at high pressure conditions. *Journal of Non-Crystalline Solids*, 338-340:56 – 60, 2004.

[18] M.N. van den Donker, B Rech, F Finger, W.M.M Kessels, and M.C.M van de Sanden. Highly efficient microcrystalline silicon solar cells deposited from a pure SiH4 flow. *Applied Physics Letters*, 87(26), Dec 26 2005.

[19] H. Richter and L. Ley. Growth of Plasma-Tranport Microcrystalline Silicon as Studied by Insitu Raman-Spectroscopy. *Journal de Physique*, 43(Nc1):247–251, 1982.

[20] O. Vetterl, F. Finger, R. Carius, P. Hapke, L. Houben, O. Kluth, A. Lambertz, A. Muck, B. Rech, and H. Wagner. Intrinsic microcrystalline silicon: A new material for photovoltaics. *Solar Energy Materials and Solar Cells*, 62(1-2):97–108, Apr 15 2000.

[21] H. Richter, Z.P. Wang, and L. Ley. The One Phonon Raman-Spectrum in Microcrystalline Silicon. *Solid State Communications*, 39(5):625–629, 1981.

[22] L. Houben, M. Luysberg, P. Hapke, R. Carius, F. Finger, and H. Wagner. Structural properties of microcrystalline silicon in the transition from highly crystalline to amorphous growth. *Philosophical Magazine A - Physics of Condensed Matter Structure Defects and Mechanical Properties*, 77(6):1447–1460, Jun 1998.

[23] G.Z. Yue, J.D. Lorentzen, J. Lin, D.X. Han, and Q. Wang. Photoluminescence and Raman studies in thin-film materials: Transition from amorphous to microcrystalline silicon. *Applied Physics Letters*, 75(4):492–494, Jul 26 1999.

[24] C. Ossadnik, S. Veprek, and I. Gregora. Applicability of Raman scattering for the characterization of nanocrystalline silicon. *Thin Solid Films*, 337(1-2):148–151, Jan 11 1999.

[25] C.V. Raman and K.S. Krishnan. A New Type of Secondary Radiation. *Nature*, 121:501–502, Jan-Jun 1928.

[26] H.W. Lo and A. Compaan. Raman Measurements of Lattice Temperature During Pulsed Layer-Heating of Silicon. *Physical Review Letters*, 44(24):1604–1607, 1980.

[27] D.E. Carlson and C.R. Wronski. Amorphous Silicon Solar-Cell. *Applied Physics Letters*, 28(11):671–673, 1976.

[28] S. Benagli, D. Borrello, E. Vallat-Sauvain, J. Meier, U. Kroll, J. Ho¨tzel, J. Spitznagel, J. Steinhauser, L. Castens, and Y. Djeridane. High-efficiency amorphous silicon devices on LPCVD-ZnO TCO prepared in industrial KAI-M R&D reactor. In *24th European Photovoltaic Solar Energy Conference, Hamburg*, September 2009.

[29] R.E.I. Schropp and M. Zeman. *Amorphous and Microcrystalline Silicon Solar Cells*. Kluwer Academic Publishers, 1998.

[30] R. Carius, F. Finger, U. Backhausen, M. Luysberg, P. Hapke, L. Houben, M. Otte, and H. Overhof. Electronic properties of microcrystalline silicon. In *Amorphous and Microcrystalline Silicon Technology - 1997*, volume 467 of *Materials Research Society Proceedings*, 1997.

[31] D.L. Staebler and C.R. Wronski. Reversible Conductivity Changes in Discharge-Produced Amorphous Si. *Applied Physics Letters*, 31(4):292–294, 1977.

[32] S. Veprek and V. Marecek. Preparations of Thin Layers of Ge and Si by Chemical Hydrogen Plasma Transport. *Solid-State Electronics*, 11(7):683–&, 1968.

[33] M. Faraji, S. Gokhale, S.M. Choudhari, M.G. Takwale, and Ghaisas. S.V. High Mobility Hydrogenated and Oxigenated Microcrystalline Siliocn as a Photosensitive Material in Photovoltaic Applications. *Applied Physics Letters*, 60(26):3289–3291, Jun 29 1992.

[34] M. Luysberg, P. Hapke, R. Carius, and F. Finger. Structure and growth of hydrogenated microcrystalline silicon: Investigation by transmission electron microscopy and Raman spectroscopy of films grown at different plasma excitation frequencies. *Philosophical Magazine A - Physics of Condensed Matter Structure Defects and Mechanical Properties*, 75(1):31–47, Jan 1997.

[35] F. Finger, S. Klein, T. Dylla, A.L.B. Neto, O. Vetterl, and R. Carius. Defects in microcrystalline silicon prepared with hot wire CVD. In *Amorphous and Heterogeneous Silicon-Based Films-2002*, Materials Research Society Symposium Proceedings, 2002.

[36] Y. Mai, S. Klein, R. Carius, J. Wolff, A. Lambertz, F. Finger, and X. Geng. Microcrystalline silicon solar cells deposited at high rates. *Journal of Applied Physics*, 97(11), Jun 1 2005.

[37] S. Reynolds, R. Carius, F. Finger, and v. Smirnov. Correlation of Structural and Optoelectronic Properties of Thin Film Silicon Prepared at the Transition from Microcrystalline to Amorphous Growth. *Thin Solid Films*, 517(23):6392 – 6395, 2009.

[38] J.K. Rath. Low Temperature Polycrystalline Silicon: a Review on Deposition, Physical Properties and Solar Cell Applications. *Solar Energy Materials and Solar Cells*, 76(4):431–487, Apr 1 2003.

[39] K. Yamamoto, M. Toshimi, T. Suzuki, Y. Tawada, T. Okamoto, and A. Nakajima. Thin Film poly-Si Solar Cell on Glass Substrate Fabricated at Low Temperature. In *MRS Spring Meeting, San Francisco*, April 1998.

[40] Luque, A. and Hegedus, S., editor. *Handbook of Photovoltaic Science and Engineering*. John Wiley & Sons, Ltd, 2003.

[41] J. Bailat, L. Fesquet, J. Orhan, Y. Djeridane, P. Wolf, B. Madliger, J. Steinhauser, S. Benagli, D. Borrello, L. Castens, G. Monteduro, M. Marmelo, B. Dehbozorghi, E. Vailltat-Sauvain, X. Multone, D. Romang, J. Boucher, J. Meier, and U. Kroll. Recent developments of high-efficiency micromorph tandem solar cells in Kai-M PECVD reactors. In *25th European Photovoltaic Solar Energy Conf.*, September 2010.

[42] A.E. Becquerel. *Comt. Rend. Acad. Sci.*, 9:561, 1839.

[43] T. Kirchartz. *Generalized detailed balance theory of solar cells*. PhD thesis, RWTH Aachen, 2009.

[44] O. Kluth, B. Rech, L. Houben, S. Wieder, G. Schope, C. Beneking, H. Wagner, A. Loffl, and H.W. Schock. Texture etched ZnO : Al coated glass substrates for silicon based thin film solar cells. *Thin Solid Films*, 351(1-2):247–253, AUG 30 1999.

[45] J. Muller, B. Rech, J. Springer, and M. Vanecek. TCO and light trapping in silicon thin film solar cells. *Solar Energy*, 77(6):917–930, 2004.

[46] D. Grunski, B. Rech, R. Schmitz, A. Mueck, O. Pincon, U. Breuer, and W. Beyer. Influence of contaminations on the performance of thin-film

silicon solar cells prepared after in situ reactor plasma cleaning. *Thin Solid Films*, 516(14):4639–4644, May 30 2008.

[47] J. Woerdenweber, T. Merdzhanova, R. Schmitz, A. Mueck, U. Zastrow, L. Niessen, A. Gordijn, R. Carius, W. Beyer, H. Stiebig, and U. Rau. Influence of base pressure and atmospheric contaminants on a-Si:H solar cell properties. *Journal of Applied Physics*, 104(9), Nov 1 2008.

[48] T. Kilper, W. Beyer, G. Braeuer, T. Bronger, R. Carius, M.N. van den Donker, D. Hrunski, A. Lambertz, T. Merdzhanova, A. Mueck, B. Rech, W. Reetz, R. Schmitz, U. Zastrow, and A. Gordijn. Oxygen and nitrogen impurities in microcrystalline silicon deposited under optimized conditions: Influence on material properties and solar cell performance. *Journal of Applied Physics*, 105(7), Apr 1 2009.

[49] E. Amanatides, D. Mataras, D. Rapakoulias, M.N. van den Donker, and B. Rech. Plasma emission diagnostics for the transition from microcrystalline to amorphous silicon solar cells. *Solar Energy Materials and Solar Cells*, 87(1-4, Sp. Iss. SI):795–805, May 2005.

[50] M.N. van den Donker, R. Schmitz, W. Appenzeller, B. Rech, W.M.M. Kessels, and M.C.M. van de Sanden. The role of plasma induced substrate heating during high rate deposition of microcrystalline silicon solar cells. *Thin Solid Films*, 511:562–566, Jul 26 2006.

[51] A.H. Mahan, J. Carapella, B.P. Nelson, R.S. Crandal, and I. Balberg. Deposition of Device Quality, Low H Content Amorphous-Silicon. *Journal of Applied Physics*, 69(9):6728–6730, May 1 1991.

[52] S. Muhl and J.M. Mendez. A review of the preparation of carbon nitride films. *Diamond and Related Materials*, 8(10):1809–1830, Oct 1999.

[53] L. Martinu and D. Poitras. Plasma deposition of optical films and coatings: A review. *Journal of Vacuum Science & Technolgy A-Vacuum Surfaces and Films*, 18(6):2619–2645, Nov-Dec 2000.

[54] B. Rech, T. Roschek, T. Repmann, J. Muller, R. Schmitz, and W. Appenzeller. Microcrystalline Silicon for Large Area Thin Film Solar Cells. *Thin Solid Films*, 427(1-2):157–165, MAR 3 2003.

[55] J. Perrin, O. Leroy, and M.C. Bordage. Cross-sections, rate constants and transport coefficients in silane plasma chemistry. *Contributions to Plasma Physics*, 36(1):3–49, 1996.

[56] S. Veprek, Z. Iqbal, and A.P. Oswald H.R.and Webb. Properties of Polycrystalline Silicon Prepared by Chemical-Transport in Hydrogen Plasma at Temperatures Between 80-Degrees C and 400-Degrees C. *Journal of Physics C- Solid State Physics*, 14(3):295–308, 1981.

[57] S. Veprek, M. Heintze, F.A. Sarott, and M. Willmott. Mechanisms of Plasma Induced Silicon Deposition and the Control of the Properties of the Deposit. In *Material Research Society Proceedings*, volume 118, page 3, 1988.

[58] C.C. Tsai, G.B. Anderson, R. Thompson, and B. Wacker. Control of Silicon Networks Structure in Plasma Deposition. *Journal of Non-Crystalline Solids*, 114(Part 1):151–153, Dec 1989.

[59] A. Matsuda. Formation Kinetics and control of Microcrystallite in muc-Si-H from Glow-Discharge Plasma. *Journal of Non-Crystalline Solids*, 59-6(Dec):767–774, 1983.

[60] N. Shibata, K. Fukuda, H. Otoshi, J. Hanna, S. Oda, and I. Shimizu. Growth of Amorphous and Crystalline Silicon by HR-CVD (Hydrogen Radical Enhanced CVD). volume 95, page 225, 1987.

[61] A.J. Lichtenberg and M.E. Lieberman. *Principles of plasma discharges and materials processing.* Wiley, New York, 1994.

[62] R. Loudon. Raman Effect In Crystals. *Advances in Physics*, 13(52):423–&, 1964.

[63] D.A. Long. *Raman spectroscopy.* McGrow-Hill International Book Company, New York, 1977.

[64] M. Cardona. *Light Scattering in Solids.* Springer, Berlin, 1982.

[65] C. Smit, R.A.C.M.M. van Swaaij, H. Donker, A.M.H.N. Petit, W.M.M. Kessels, and M.C.M. van de Sanden. Determining the material structure of microcrystalline silicon from Raman spectra. *Journal of A*, 94(5):3582–3588, SEP 1 2003.

[66] O. Vetterl. *On the Physics of Microcrystalline silicon Thin film Solar Cells*. PhD thesis, Heinrich-Heine-Universität Düsseldorf, 2001.

[67] D. Bermejo and M. Cardona. Raman Scattering in Pure and Hydrogenated Amorphous-Germanium and Silicon. *Journal of Non-Crystalline Solids*, 32(1-3):405–419, 1979.

[68] M. Grimsditch and M. Cardona. Absolute Cross-Section for Raman Scattering by Phonons in Silicon. *Physica Status Solidi B-Basic Research*, 102(1):155–161, 1980.

[69] A. Einstein. Quantum theory of monatomic ideal gases. *Sitzungsberichte der Preussischen Akademie der Wissenschaften Physikalisch-Mathematische Klasse*, pages 261–267, 1924.

[70] F.A. Lindholm, J.G. Fossum, and E.L. Burgess. Application of the Superposition Principle to Solar-Cell Analysis. *IEEE Transactions on Electronic Devices*, 26(3):165–171, 1979.

[71] F. Koehler. Ramanspektroskopie zur Charakterisierung von μc-Si:H und verwandten Materialien. Master's thesis, RWTH Aachen, 2008.

[72] T. Roschek, T. Repmann, J. Muller, B. Rech, and H. Wagner. Comprehensive Study of Microcrystalline Silicon Solar Cells Deposited at High Rate Using 13.56 MHz Plasma-Enhanced Chemical Vapor Deposition. *Journal of Vacuum Science & Technolgy A-Vacuum Surfaces and Films*, 20(2):492–498, Mar-Apr 2002.

[73] A.A. Howling, B. Strahm, P. Colsters, L. Sansonnens, and C. Hollenstein. Fast equilibration of silane/hydrogen plasmas in large area RF capacitive reactors monitored by optical emission spectroscopy. *Plasma Sources Science and Technology*, 16(4):679, 2007.

[74] S. Nunomura, I. Yosida, and M. Kondo. Time-dependent gas phase kinetics in a hydrogen diluted silane plasma. *Applied Physics Letters*, 94:071502, 2009.

[75] J.M. Poate and J.W. Mayer. *Laser Annealing of Semiconductors*. Academic Press, New York, 1982.

[76] S. Muthmann, M. Meier, R. Schmitz, W. Appenzeller, A. Mück, and A. Gordijn. The Effect of Disturbed PECVD Electrode Surfaces on the

Homogeneity of Microcrystalline Silicon Films. *Surface and Coatings Technology*, 205(Supplement 2):S415 – S418, 2011.

[77] S. Nunomura and M. Kondo. Characterization of high-pressure capacitively coupled hydrogen plasmas. *Journal of Applied Physics*, 102(9), Nov 1 2007.

[78] M. Takai, T. Nishimoto, T. Takagi, M. Kondo, and A. Matsuda. Guiding principles for obtaining stabilized amorphous silicon at larger growth rates. *Journal of Non-Crystalline Solids*, 266-269(Part 1):90 – 94, 2000.

[79] M. Takai, T. Takagi, T. Nishimoto, M. Kondo, and A. Matsuda. Excitation frequency dependence of the optical emission intensity vs. deposition rate relationship in silane plasmas. *Surface and Coatings Technology*, 131(1-3):50 – 53, 2000.

[80] E. Amanatides, A. Hammad, E. Katsia, and D. Mataras. High pressure regime of plasma enhanced deposition of microcrystalline silicon. *Journal of Applied Physics*, 97(7), Apr 1 2005.

[81] D.G. Cahill, M. Katiyar, and J.R. Ableson. Thermal Conductivity of Alpha-SiH Thin-Films. *Physical Review B*, 50(9):6077–6081, Sep 1 1994.

[82] S. Uma, A.D. McConnell, M. Asheghi, K. Kurabayashi, and K.E. Goodson. Temperature-dependent thermal conductivity of undoped polycrystalline silicon layers. *International Journal of Thermophysics*, 22(2):605–616, MAR 2001.

[83] S. Haas. *Untersuchung und Optimierung der Serienverschaltung von Silizium-Dünnschicht-Solarmodulen*. PhD thesis, RWTH Aachen, 2010.

[84] M.W. Wolf and J.J Martin. Low Temperature Thermal-Conductivity of Zinc Oxide. *Physica Status Solidi A - Applied Research*, 17(1):215–220, 1973.

[85] H.C. Webbber, A.G. Cullis, and N.G. Chew. Computer-Simulation of High Speed Melting of Amorphous-Silicon. *Applied Physics Letters*, 43(7):669–671, 1983.

[86] H.J. Eichler, B. Eppich, J. Fischer, R. Güther, Gurzadyan G.G., A. Hermerschmidt, A. Laubereau, V.A. Lopota, Mehl O., C.R. Vidal, H. Weber, and B. Wende. *Laser Physics and Applications*, volume A: Laser Fundamentals. Springer-Verlag, Berlin, Heidelberg, New York, 2004.

[87] T.R. Hart, R.L. Aggarwal, and B. Lax. Temperature Dependence of Raman Scattering in Silicon. *Physical Review B*, 1(2):638–&, 1970.

[88] T. Merdzhanova, J. Woerdenweber, W. Beyer, U. Zastrow, H. Stiebig, and A. Gordijn. High critical oxygen concentration in microcrystalline silicon solar cells. *Physica Status Solidi - Rapid Research Letters*, 4(11):323–325, Nov 2010.

[89] R. Swanepoel. Determination of the Thickness and Optical-Constant of Amorphous Silicon. *Journal of Physics E-Scientific Instruments*, 16(12):1214–1222, 1983.

[90] M. Meier, S. Muthmann, A.J. Flikweert, G. Dingemans, and M.C.M. van de Sanden. In-situ transmission measurements as process control for thin-film silicon solar cells. *Solar Energy Materials and Solar Cells*, 2011.

[91] S. Muthmann, F. Koehler, M. Meier, M. Huelsbeck, R. Carius, and A. Gordijn. Monitoring of the growth of microcrystalline silicon by plasma-enhanced chemical vapor deposition using in-situ Raman spectroscopy. *Physica Status Solidi - Rapid Research Letters*, 5(4):144–146, Apr 2011.

[92] S. Koynov, S. Grebner, P. Radojkovic, E. Hartmann, R. Schwarz, L. Vasilev, R. Krankenhagen, I. Sieber, W. Henrion, and M. Schmidt. Initial stages of microcrystalline silicon film growth. *Journal of Non-Crystalline Solids*, 198-200(Part 2):1012–1016, 1996.

[93] P. Roca i Cabarrocas. Plasma enhanced chemical vapor deposition of amorphous, polymorphous and microcrystalline silicon films. *Journal of Non-Crystalline Solids*, 266-269(Part 1):31 – 37, 2000.

[94] F. Koehler, S. Schicho, B. Wolfrum, A. Gordijn, S.E. Pust, and R. Carius. Gradient Etching of Silicon-Based Thin Films for Depth-Resolved Measurements: The Example of Raman Crystallinity. *Thin Solid Films*, 520:2605–2608, 2012.

[95] K.H. Jun, R. Carius, and H. Stiebig. Optical characteristics of intrinsic microcrystalline silicon. *Physical Review B*, 66(11), Sep 15 2002.

[96] J. Bailat, E. Vallat-Sauvain, L. Feitknecht, C. Droz, and A. Shah. Microstructure and open-circuit voltage of n-i-p microcrystalline silicon solar cells. *Journal of Applied Physics*, 93(9):5727–5732, May 1 2003.

[97] T. Fujibayashi and M. Kondo. Roles of microcrystalline silicon p layer as seed, window, and doping layers for microcrystalline silicon p-i-n solar cells. *Journal of Applied Physics*, 99(4), Feb 15 2006.

[98] G.Z. Yue, B.J. Yan, G. Ganguly, J. Yang, S. Guha, and C.W. Teplin. Material structure and metastability of hydrogenated nanocrystalline silicon solar cells. *Applied Physics Letters*, 88(26), Jun 26 2006.

[99] T. Kilper, M.N. van den Donker, R. Carius, B. Rech, G. Bräuer, and T Repmann. Process control of high rate microcrystalline silicon based solar cell deposition by optical emission spectroscopy. *Thin Solid Films*, 516(14):4633 – 4638, 2008.

[100] M.N. van den Donker, B. Rech, W.M.M. Kessels, and M.C.M. van de Sanden. Transient depletion of source gases during materials processing: a case study on the plasma deposition of microcrystalline silicon. *New Journal of Physics*, 9, Aug 23 2007.

[101] R.W. Collins and B.Y. Yang. Iinsitu Ellipsometry of Thin-Film Deposition - Implications for Amorphous and Microcrystalline Growth. *Journal of Vacuum Science & Technolgy B*, 7(5):1155–1164, Sep-Oct 1989.

[102] M. Kondo, Y. Toyoshima, A. Matsuda, and K. Ikuta. Substrate dependence of initial growth of microcrystalline silicon in plasma-enhanced chemical vapor deposition. *Journal of Applied Physics*, 80(10):6061–6063, Nov 15 1996.

[103] M. Tzolov, F. Finger, R. Carius, and P. Hapke. Optical and transport studies on thin microcrystalline silicon films prepared by very high frequency glow discharge for solar cell applications. *Journal of Applied Physics*, 81(11):7376–7385, Jun 1 1997.

[104] N. Wyrsch, P. Torres, M. Goerlitzer, E. Vallat, U. Kroll, A. Shah, A. Poruba, and M. Vanecek. Hydrogenated Microcrystalline Silicon for Photovoltaic Applications. *Solid State Phenomena*, 67-8:89–100, 1999.

[105] Ch. Ross, J. Herion, R. Carius, and H. Wagner. Nucleation and growth of low-temperature fine-crystalline silicon: a scanning probe microscopy and Raman spectroscopy study of the influence of hydrogen and different substrates. *Materials Science and Engineering B*, 72(1):1 – 6, 2000.

[106] F. Edelman, A. Chack, R. Weil, R.and Beserman, Yu.L. Khait, P. Werner, B. Rech, T. Roschek, R. Carius, H. Wagner, and W. Beyer. Structure of PECVD Si:H films for solar cell applications. *Solar Energy Materials and Solar Cells*, 77(2):125 – 143, 2003.

[107] J. Bailat, E. Vallat-Sauvain, L. Feitknecht, C. Droz, and A. Shah. Influence of substrate on the microstructure of microcrystalline silicon layers and cells. *Journal of Non-Crystalline Solids*, 299(Part b):1219–1223, Apr 1 2002.

[108] B.E. Pieters, H. Stiebig, M. Zeman, and R.A.C.M.M. van Swaaij. Determination of the Mobility Gap of Intrinsic mu c-Si:H in p-i-n Solar Cells. *Journal of Applied Physics*, 105(4), Feb 15 2009.

[109] M.N. van den Donker, T. Kilper, D. Grunsky, B. Rech, L. Houben, W.M.M. Kessels, and M.C.M. van de Sanden. Microcrystalline silicon deposition: Process stability and process control. *Thin Solid Films*, 515(19):7455–7459, Jul 16 2007.

[110] B.J. Yan, G.Z. Yue, J. Yang, S. Guha, D.L. Williamson, D. Han, and C.S. Jiang. Hydrogen dilution profiling for hydrogenated microcrystalline silicon solar cells. *Applied Physics Letters*, 85(11):1955–1957, Sep 13 2004.

[111] A. Matsuda. Growth mechanism of microcrystalline silicon obtained from reactive plasmas. *Thin Solid Films*, 337(1-2):1–6, Jan 11 1999.

[112] M. Kondo, M. Fukawa, L.H. Guo, and A. Matsuda. High rate growth of microcrystalline silicon at low temperatures. *Journal of Non-Crystalline Solids*, 266(Part a):84–89, May 2000.

[113] S. Klein, F. Finger, R. Carius, and M. Stutzmann. Deposition of microcrystalline silicon prepared by hot-wire chemical-vapor deposition: The influence of the deposition parameters on the material properties and solar cell performance. *Journal of Applied Physics*, 98(2), Jul 15 2005.

[114] D. Smith and I.C. Plumb. Appraisal of Mass-Spectrometer Diagnostic Technique in Study of Afterglow Plasmas. *Journal of Physics D-Applied Physics*, 6(12):1431–1446, 1973.

[115] L.J. Overzet, J.H. Beberman, and J.T. Verdeyen. Enhancement of

the Negative-Ion Flux to Surfaces from Radio-Frequency Processing Discharges. *Journal of Applied Physics*, 66(4):1622–1631, Aug 15 1989.

[116] L.J. Overzet. Model for Charge Movement after the Radio-Frequency Excitation is Extinguished. *Journal of Vacuum Science & Technolgy A-Vacuum Surfaces and Films*, 11(4, Part 1):1114–1118, Jul-Aug 1993.

[117] A.A. Howling, L. Sansonnens, J.L. Dorier, and C. Hollenstein. Time Resolved Measurements of Highly Polymerized Negative-Ions in Radio Frequency Silane Plasma Deposition Experiments. *Journal of Applied Physics*, 75(3):1340–1353, Feb 1 1994.

[118] C. Anandan, C. Mukherjee, T. Seth, P.N. Dixit, and R. Bhattacharyya. Effect of Pulse Parameters on the Deposition Rate of Hydrogenated Amorphous Silicon in a Modified Pulsed Plasma Discharge. *Applied Physics Letters*, 66(1):85–87, Jan 2 1995.

[119] A.C.W. Biebericher, J. Bezemer, W.F. van der Weg, and W.J. Goedheer. Deposition rate in modulated radio-frequency silane plasmas. *Applied Physics Letters*, 76(15):2002–2004, Apr 10 2000.

[120] A.C.W. Biebericher. *Deposition Techniques of hydrogenated amorphous silicon using modulated radio-frequency plasmas*. PhD thesis, University of Utrecht, 2002.

[121] C. Niikura, M. Kondo, and A. Matsuda. Preparation of microcrystalline silicon films at ultra high-rate of 10 nm/s using high-density plasma. *Journal of Non-Crystalline Solids*, 338-340:42 – 46, 2004. Proceedings of the 20th International Conference on Amorphous and Microcrystalline Semiconductors.

[122] J. Perrin. Modelling of the power dissipation and rovibrational heating and cooling in SiH_4-H_2 RF glow discharges. *Journal of Physics D-Applied Physics*, 26(10):1662–1679, 1993.

Danksagung

An dieser Stelle möchte ich mich bei allen bedanken, die zum Gelingen dieser Arbeit beigetragen haben. Besonders erwähnen möchte ich hierbei:
Prof. Dr. Uwe Rau für die Betreuung und Begutachtung der Arbeit und die Möglichkeit an einem Institut in einer innovativen Atmosphäre an einem spannenden Thema zu arbeiten.
Prof. Dr. Vladimir Dyakonov für sein Interesse an der Arbeit und die Übernahme der Begutachtung.
Dr. Aad Gordijn für eine motivierende Betreuung, viele gute Ideen und das geduldige Korrekturlesen meiner Arbeit an dessen Ende endlich eine zufriedenstellende Struktur entstanden ist.
Prof. Dr. Reinhard Carius für die Mitübernahme der Betreuung, interessante Diskussionen und viele hilfreiche Ratschläge.
Markus Hülsbeck für die umfangreiche Hilfe beim Aufbau des Experiments, die Unterstützung bei allen optischen Fragen und die vielen guten Ideen, die das Gelingen der Arbeit erst ermöglicht haben.
Florian Köhler für die Vorbereitung meiner Arbeit durch seine Vorexperimente und viele hilfreiche Diskussionen zur Raman-Spektroskopie.
Das 5-Kammer Team Ralf Schmitz und Andreas Mück für eine sehr angenehme Arbeitsatmosphäre, technische Hilfe und für eine funktionierende PECVD Anlage (trotz meiner ständigen Schraubereien).
Dr. Stefan Haas für seine Unterstützung bei den Simulationen zur Laserabsorption und für hilfreiche Diskussionen zu vielen anderen Fragen.
Die Kollegen Dr. Matthias Meier, Dr. Tsvetelina Merdzhanova, Dr. Jan Wördenweber, Thomas Zimmermann, Dr. Sandra Schicho und Dr. Bart Pieters für viele interessante Diskussionen.
Die Mitkonstrukteure Wolfgang Appenzeller und Dr. Dzmitry Hrunsky für ihre wertvolle Hilfe bei der Konzeption der in-situ Raman Elektrode.

Die Konstruktionsabteilung und Werkstatt des ICS für die hervorragende Arbeit bei der Entwicklung und der Fertigung der in-situ Raman Elektrode.
Dr. Martina Luysberg und Dr. Andras Kovacs für TEM Messungen und Erklärungen, die auch für einen Laien verständlich waren.
Prof. Dr. Bernd Rech für eine hilfreiche Diskussion zum Thema der gepulsten Plasmen.
Die zahlreichen Bürokollegen, mit denen ich immer gerne zusammengearbeitet habe und die durch ihr Fachwissen zum Gelingen meiner Arbeit beigetragen haben.
Den Kollegen, die hier namentlich nicht erwähnt wurden, möchte ich für ein inspirierendes und von Kollegialität geprägtes Umfeld danken, in dem es sehr viel Spaß gemacht hat, meine Doktorarbeit anzufertigen.

List of Publications

Publications associated with this thesis

S. Muthmann, M. Meier, R. Schmitz, W. Appenzeller, A. Mück and A. Gordijn. The Effekt of Disturbed PECVD Electrode Surfaces on the Homogeneity of Microcrystalline Silicon Films. *Surface and Coatings Technology*, 205(Supplement 2): S415-S418, 2011

S. Muthmann, F. Koehler, M. Meier, M. Huelsbeck, R. Carius, and A. Gordijn. Monitoring of the growth of microcrystalline silicon by plasma-enhanced chemical vapor deposition using in-situ Raman spectroscopy. *Physica Status Solidi - Rapid Research Letters*, 5(4):144-146, 2011.

S. Muthmann, F. Köhler, M. Hülsbeck, M. Meier, A. Mück, R. Schmitz, W. Appenzeller, R. Carius and A. Gordijn. Monitoring the growth of microcrystalline silicon deposited by plasma-enhanced chemical vapor deposition using in-situ Raman spectroscopy. *Proc. of the MRS Spring Meeting 2011*

S. Muthmann, F. Köhler, M. Meier, M. Hülsbeck, R. Carius, A. Gordijn. In-situ Raman spectroscopy used to study and control the initial growth phase of microcrystalline absorber layers for thin-film silicon solar cells. *Journal of Non-Crystaline Solids* 2012, DOI: 10.1016/j.jnoncrysol.2011.12.061

Other Publications

S. Schicho, S. Muthmann, A. Gordijn. Thin (< 1 μm) a-Si/μc-Si tandem solar cells for high stable efficiencies. *Proc. of the 23rd PVSEC Valencia*, 2008

T. Kilper, D. Hrunski, J. Kirchhoff, J. Kroll, S. Muthmann, J. Noll, W. Reetz, S. Schicho, G. Schöpe, C. Zahren and A.Gordijn. High-Rate Deposited Amorphous and Microcrystalline Silicon Based Tandem Cells and Modules. *Proc. of the 24th PVSEC Hamburg*, 2009

S. Muthmann, F. Köhler, R. Carius, and A. Gordijn. Structural order on different length scales in amorphous silicon investigated by Raman spectroscopy. *Physica Status Solidi A* 207 (3) 544-547, 2010

A. Gordijn, S. Schicho, S. Muthmann, T. Kilper, H. Zhu, E. Bunte, and J. Hüpkes. Significantly decreased production times for a-Si/mc-Si tandem cells on texture-etched ZnO:Al. *Physica Stauts Solidi A* 207 (3) 678-681, 2010

M. Meier, S. Muthmann, G. Dingemans, M. C. M. van de Sanden, M. Schulte, and A. Gordijn. Optical Transmission Spectroscopy as Real Time Process Control for Thin-Film Silicon PECVD. *Proc. of the 25th PVSEC Valencia*, 2010

S. Muthmann and A. Gordijn. Amorphous silicon solar cells deposited with non-constant silane concentration.*Solar Energy Materials and Solar Cells* 95 (2) 573-578, 2011

M. Meier, T. Merdzhanova, U. W. Paetzold, S. Muthmann, A. M¨uck, R. Schmitz, and A. Gordijn. In Situ Current Determination of a-Si/μc-Si Tandem Solar Cells via Transmission Measurements During Silicon PECVD. *IEEE Journal of Photovoltaics*, 2012 DOI:10.1109/JPHOTOV.2011.2179413

M. Meier, S. Muthmann, A.J. Flikweert, G. Dingemans, M.C.M. van de Sanden, A. Gordijn. In-situ transmission measurements as process control for thin-film silicon solar cells. *Solar Energy Materials and Solar Cells* 95, 3328-3332, 2011

1. **Einsatz von multispektralen Satellitenbilddaten in der Wasserhaushalts- und Stoffstrommodellierung – dargestellt am Beispiel des Rureinzugsgebietes**
   von C. Montzka (2008), XX, 238 Seiten
   ISBN: 978-3-89336-508-1

2. **Ozone Production in the Atmosphere Simulation Chamber SAPHIR**
   by C. A. Richter (2008), XIV, 147 pages
   ISBN: 978-3-89336-513-5

3. **Entwicklung neuer Schutz- und Kontaktierungsschichten für Hochtemperatur-Brennstoffzellen**
   von T. Kiefer (2008), 138 Seiten
   ISBN: 978-3-89336-514-2

4. **Optimierung der Reflektivität keramischer Wärmedämmschichten aus Yttrium-teilstabilisiertem Zirkoniumdioxid für den Einsatz auf metallischen Komponenten in Gasturbinen**
   von A. Stuke (2008), X, 201 Seiten
   ISBN: 978-3-89336-515-9

5. **Lichtstreuende Oberflächen, Schichten und Schichtsysteme zur Verbesserung der Lichteinkopplung in Silizium-Dünnschichtsolarzellen**
   von M. Berginski (2008), XV, 171 Seiten
   ISBN: 978-3-89336-516-6

6. **Politikszenarien für den Klimaschutz IV – Szenarien bis 2030**
   hrsg.von P. Markewitz, F. Chr. Matthes (2008), 376 Seiten
   ISBN 978-3-89336-518-0

7. **Untersuchungen zum Verschmutzungsverhalten rheinischer Braunkohlen in Kohledampferzeugern**
   von A. Schlüter (2008), 164 Seiten
   ISBN 978-3-89336-524-1

8. **Inorganic Microporous Membranes for Gas Separation in Fossil Fuel Power Plants**
   by G. van der Donk (2008), VI, 120 pages
   ISBN: 978-3-89336-525-8

9. **Sinterung von Zirkoniumdioxid-Elektrolyten im Mehrlagenverbund der oxidkeramischen Brennstoffzelle (SOFC)**
   von R. Mücke (2008), VI, 165 Seiten
   ISBN: 978-3-89336-529-6

10. **Safety Considerations on Liquid Hydrogen**
    by K. Verfondern (2008), VIII, 167 pages
    ISBN: 978-3-89336-530-2

11. **Kerosinreformierung für Luftfahrtanwendungen**
von R. C. Samsun (2008), VII, 218 Seiten
ISBN: 978-3-89336-531-9

12. **Der 4. Deutsche Wasserstoff Congress 2008 – Tagungsband**
hrsg. von D. Stolten, B. Emonts, Th. Grube (2008), 269 Seiten
ISBN: 978-3-89336-533-3

13. **Organic matter in Late Devonian sediments as an indicator for environmental changes**
by M. Kloppisch (2008), XII, 188 pages
ISBN: 978-3-89336-534-0

14. **Entschwefelung von Mitteldestillaten für die Anwendung in mobilen Brennstoffzellen-Systemen**
von J. Latz (2008), XII, 215 Seiten
ISBN: 978-3-89336-535-7

15. **RED-IMPACT**
Impact of Partitioning, Transmutation and Waste Reduction Technologies on the Final Nuclear Waste Disposal
SYNTHESIS REPORT
ed. by W. von Lensa, R. Nabbi, M. Rossbach (2008), 178 pages
ISBN 978-3-89336-538-8

16. **Ferritic Steel Interconnectors and their Interactions with Ni Base Anodes in Solid Oxide Fuel Cells (SOFC)**
by J. H. Froitzheim (2008), 169 pages
ISBN: 978-3-89336-540-1

17. **Integrated Modelling of Nutrients in Selected River Basins of Turkey**
Results of a bilateral German-Turkish Research Project
project coord. M. Karpuzcu, F. Wendland (2008), XVI, 183 pages
ISBN: 978-3-89336-541-8

18. **Isotopengeochemische Studien zur klimatischen Ausprägung der Jüngeren Dryas in terrestrischen Archiven Eurasiens**
von J. Parplies (2008), XI, 155 Seiten, Anh.
ISBN: 978-3-89336-542-5

19. **Untersuchungen zur Klimavariabilität auf dem Tibetischen Plateau - Ein Beitrag auf der Basis stabiler Kohlenstoff- und Sauerstoffisotope in Jahrringen von Bäumen waldgrenznaher Standorte**
von J. Griessinger (2008), XIII, 172 Seiten
ISBN: 978-3-89336-544-9

20. **Neutron-Irradiation + Helium Hardening & Embrittlement Modeling of 9%Cr-Steels in an Engineering Perspective (HELENA)**
by R. Chaouadi (2008), VIII, 139 pages
ISBN: 978-3-89336-545-6

21. **in Bearbeitung**

22. **Verbundvorhaben APAWAGS (AOEV und Wassergenerierung) – Teilprojekt: Brennstoffreformierung – Schlussbericht**
von R. Peters, R. C. Samsun, J. Pasel, Z. Porš, D. Stolten (2008), VI, 106 Seiten
ISBN: 978-3-89336-547-0

23. **FREEVAL**
Evaluation of a Fire Radiative Power Product derived from Meteosat 8/9 and Identification of Operational User Needs
Final Report
project coord. M. Schultz, M. Wooster (2008), 139 pages
ISBN: 978-3-89336-549-4

24. **Untersuchungen zum Alkaliverhalten unter Oxycoal-Bedingungen**
von C. Weber (2008), VII, 143, XII Seiten
ISBN: 978-3-89336-551-7

25. **Grundlegende Untersuchungen zur Freisetzung von Spurstoffen, Heißgaschemie, Korrosionsbeständigkeit keramischer Werkstoffe und Alkalirückhaltung in der Druckkohlenstaubfeuerung**
von M. Müller (2008), 207 Seiten
ISBN: 978-3-89336-552-4

26. **Analytik von ozoninduzierten phenolischen Sekundärmetaboliten in *Nicotiana tabacum* L. cv Bel W3 mittels LC-MS**
von I. Koch (2008), III, V, 153 Seiten
ISBN 978-3-89336-553-1

27. **IEF-3 Report 2009. Grundlagenforschung für die Anwendung**
(2009), ca. 230 Seiten
ISBN: 978-3-89336-554-8

28. **Influence of Composition and Processing in the Oxidation Behavior of MCrAlY-Coatings for TBC Applications**
by J. Toscano (2009), 168 pages
ISBN: 978-3-89336-556-2

29. **Modellgestützte Analyse signifikanter Phosphorbelastungen in hessischen Oberflächengewässern aus diffusen und punktuellen Quellen**
von B. Tetzlaff (2009), 149 Seiten
ISBN: 978-3-89336-557-9

30. **Nickelreaktivlot / Oxidkeramik – Fügungen als elektrisch isolierende Dichtungskonzepte für Hochtemperatur-Brennstoffzellen-Stacks**
von S. Zügner (2009), 136 Seiten
ISBN: 978-3-89336-558-6

31. **Langzeitbeobachtung der Dosisbelastung der Bevölkerung in radioaktiv kontaminierten Gebieten Weißrusslands – Korma-Studie**
von H. Dederichs, J. Pillath, B. Heuel-Fabianek, P. Hill, R. Lennartz (2009), Getr. Pag.
ISBN: 978-3-89336-532-3

32. **Herstellung von Hochtemperatur-Brennstoffzellen über physikalische Gasphasenabscheidung**
von N. Jordán Escalona (2009), 148 Seiten
ISBN: 978-3-89336-532-3

33. **Real-time Digital Control of Plasma Position and Shape on the TEXTOR Tokamak**
by M. Mitri (2009), IV, 128 pages
ISBN: 978-3-89336-567-8

34. **Freisetzung und Einbindung von Alkalimetallverbindungen in kohlebefeuerten Kombikraftwerken**
von M. Müller (2009), 155 Seiten
ISBN: 978-3-89336-568-5

35. **Kosten von Brennstoffzellensystemen auf Massenbasis in Abhängigkeit von der Absatzmenge**
von J. Werhahn (2009), 242 Seiten
ISBN: 978-3-89336-569-2

36. **Einfluss von Reoxidationszyklen auf die Betriebsfestigkeit von anodengestützten Festoxid-Brennstoffzellen**
von M. Ettler (2009), 138 Seiten
ISBN: 978-3-89336-570-8

37. **Großflächige Plasmaabscheidung von mikrokristallinem Silizium für mikromorphe Dünnschichtsolarmodule**
von T. Kilper (2009), XVII, 154 Seiten
ISBN: 978-3-89336-572-2

38. **Generalized detailed balance theory of solar cells**
by T. Kirchartz (2009), IV, 198 pages
ISBN: 978-3-89336-573-9

39. **The Influence of the Dynamic Ergodic Divertor on the Radial Electric Field at the Tokamak TEXTOR**
von J. W. Coenen (2009), xii, 122, XXVI pages
ISBN: 978-3-89336-574-6

40. **Sicherheitstechnik im Wandel Nuklearer Systeme**
von K. Nünighoff (2009), viii, 215 Seiten
ISBN: 978-3-89336-578-4

41. **Pulvermetallurgie hochporöser NiTi-Legierungen für Implanat- und Dämpfungsanwendungen**
von M. Köhl (2009), XVII, 199 Seiten
ISBN: 978-3-89336-580-7

42. **Einfluss der Bondcoatzusammensetzung und Herstellungsparameter auf die Lebensdauer von Wärmedämmschichten bei zyklischer Temperaturbelastung**
von M. Subanovic (2009), 188, VI Seiten
ISBN: 978-3-89336-582-1

43. **Oxygen Permeation and Thermo-Chemical Stability of Oxygen Permeation Membrane Materials for the Oxyfuel Process**
by A. J. Ellett (2009), 176 pages
ISBN: 978-3-89336-581-4

44. **Korrosion von polykristallinem Aluminiumoxid (PCA) durch Metalljodidschmelzen sowie deren Benetzungseigenschaften**
von S. C. Fischer (2009), 148 Seiten
ISBN: 978-3-89336-584-5

45. **IEF-3 Report 2009. Basic Research for Applications**
(2009), 217 Seiten
ISBN: 978-3-89336-585-2

46. **Verbundvorhaben ELBASYS (Elektrische Basissysteme in einem CFK-Rumpf) - Teilprojekt: Brennstoffzellenabgase zur Tankinertisierung - Schlussbericht**
von R. Peters, J. Latz, J. Pasel, R. C. Samsun, D. Stolten
(2009), xi, 202 Seiten
ISBN: 978-3-89336-587-6

47. **Aging of ^{14}C-labeled Atrazine Residues in Soil: Location, Characterization and Biological Accessibility**
by N. D. Jablonowski (2009), IX, 104 pages
ISBN: 978-3-89336-588-3

48. **Entwicklung eines energetischen Sanierungsmodells für den europäischen Wohngebäudesektor unter dem Aspekt der Erstellung von Szenarien für Energie- und CO_2 - Einsparpotenziale bis 2030**
von P. Hansen (2009), XXII, 281 Seiten
ISBN: 978-3-89336-590-6

49. **Reduktion der Chromfreisetzung aus metallischen Interkonnektoren für Hochtemperaturbrennstofzellen durch Schutzschichtsysteme**
von R. Trebbels (2009), iii, 135 Seiten
ISBN: 978-3-89336-591-3

50. **Bruchmechanische Untersuchung von Metall / Keramik-Verbundsystemen für die Anwendung in der Hochtemperaturbrennstoffzelle**
von B. Kuhn (2009), 118 Seiten
ISBN: 978-3-89336-592-0

51. **Wasserstoff-Emissionen und ihre Auswirkungen auf den arktischen Ozonverlust**
Risikoanalyse einer globalen Wasserstoffwirtschaft
von T. Feck (2009), 180 Seiten
ISBN: 978-3-89336-593-7

52. **Development of a new Online Method for Compound Specific Measurements of Organic Aerosols**
by T. Hohaus (2009), 156 pages
ISBN: 978-3-89336-596-8

53. **Entwicklung einer FPGA basierten Ansteuerungselektronik für Justageeinheiten im Michelson Interferometer**
von H. Nöldgen (2009), 121 Seiten
ISBN: 978-3-89336-599-9

54. **Observation – and model – based study of the extratropical UT/LS**
by A. Kunz (2010), xii, 120, xii pages
ISBN: 978-3-89336-603-3

55. **Herstellung polykristalliner Szintillatoren für die Positronen-Emissions-Tomographie (PET)**
von S. K. Karim (2010), VIII, 154 Seiten
ISBN: 978-3-89336-610-1

56. **Kombination eines Gebäudekondensators mit H2-Rekombinatorelementen in Leichtwasserreaktoren**
von S. Kelm (2010), vii, 119 Seiten
ISBN: 978-3-89336-611-8

57. **Plant Leaf Motion Estimation Using A 5D Affine Optical Flow Model**
by T. Schuchert (2010), X, 143 pages
ISBN: 978-3-89336-613-2

58. **Tracer-tracer relations as a tool for research on polar ozone loss**
by R. Müller (2010), 116 pages
ISBN: 978-3-89336-614-9

59. **Sorption of polycyclic aromatic hydrocarbon (PAH) to Yangtze River sediments and their components**
by J. Zhang (2010), X, 109 pages
ISBN: 978-3-89336-616-3

60. **Weltweite Innovationen bei der Entwicklung von CCS-Technologien und Möglichkeiten der Nutzung und des Recyclings von CO_2**
Studie im Auftrag des BMWi
von W. Kuckshinrichs et al. (2010), X, 139 Seiten
ISBN: 978-3-89336-617-0

61. **Herstellung und Charakterisierung von sauerstoffionenleitenden Dünnschichtmembranstrukturen**
von M. Betz (2010), XII, 112 Seiten
ISBN: 978-3-89336-618-7

62. **Politikszenarien für den Klimaschutz V – auf dem Weg zum Strukturwandel, Treibhausgas-Emissionsszenarien bis zum Jahr 2030**
hrsg. von P. Hansen, F. Chr. Matthes (2010), 276 Seiten
ISBN: 978-3-89336-619-4

63. **Charakterisierung Biogener Sekundärer Organischer Aerosole mit Statistischen Methoden**
von C. Spindler (2010), iv, 163 Seiten
ISBN: 978-3-89336-622-4

64. **Stabile Algorithmen für die Magnetotomographie an Brennstoffzellen**
von M. Wannert (2010), ix, 119 Seiten
ISBN: 978-3-89336-623-1

65. **Sauerstofftransport und Degradationsverhalten von Hochtemperaturmembranen für CO2-freie Kraftwerke**
von D. Schlehuber (2010), VII, 139 Seiten
ISBN: 978-3-89336-630-9

66. **Entwicklung und Herstellung von foliengegossenen, anodengestützten Festoxidbrennstoffzellen**
von W. Schafbauer (2010), VI, 164 Seiten
ISBN: 978-3-89336-631-6

67. **Disposal strategy of proton irradiated mercury from high power spallation sources**
by S. Chiriki (2010), xiv, 124 pages
ISBN: 978-3-89336-632-3

68. **Oxides with polyatomic anions considered as new electrolyte materials for solid oxide fuel cells (SOFCs)**
by O. H. Bin Hassan (2010), vii, 121 pages
ISBN: 978-3-89336-633-0

69. **Von der Komponente zum Stack: Entwicklung und Auslegung von HT-PEFC-Stacks der 5 kW-Klasse**
von A. Bendzulla (2010), IX, 203 Seiten
ISBN: 978-3-89336-634-7

70. **Satellitengestützte Schwerewellenmessungen in der Atmosphäre und Perspektiven einer zukünftigen ESA Mission (PREMIER)**
von S. Höfer (2010), 81 Seiten
ISBN: 978-3-89336-637-8

71. **Untersuchungen der Verhältnisse stabiler Kohlenstoffisotope in atmosphärisch relevanten VOC in Simulations- und Feldexperimenten**
von H. Spahn (2010), IV, 210 Seiten
ISBN: 978-3-89336-638-5

72. **Entwicklung und Charakterisierung eines metallischen Substrats für nanostrukturierte keramische Gastrennmembranen**
von K. Brands (2010), vii, 137 Seiten
ISBN: 978-3-89336-640-8

73. **Hybridisierung und Regelung eines mobilen Direktmethanol-Brennstoffzellen-Systems**
von J. Chr. Wilhelm (2010), 220 Seiten
ISBN: 978-3-89336-642-2

74. **Charakterisierung perowskitischer Hochtemperaturmembranen zur Sauerstoffbereitstellung für fossil gefeuerte Kraftwerksprozesse**
von S.A. Möbius (2010) III, 208 Seiten
ISBN: 978-3-89336-643-9

75. **Characterization of natural porous media by NMR and MRI techniques: High and low magnetic field studies for estimation of hydraulic properties**
by L.-R. Stingaciu (2010), 96 pages
ISBN: 978-3-89336-645-3

76. **Hydrological Characterization of a Forest Soil Using Electrical Resistivity Tomography**
by Chr. Oberdörster (2010), XXI, 151 pages
ISBN: 978-3-89336-647-7

77. **Ableitung von atomarem Sauerstoff und Wasserstoff aus Satellitendaten und deren Abhängigkeit vom solaren Zyklus**
von C. Lehmann (2010), 127 Seiten
ISBN: 978-3-89336-649-1

78. **18th World Hydrogen Energy Conference 2010 – WHEC2010 Proceedings**
Speeches and Plenary Talks
ed. by D. Stolten, B. Emonts (2012), V, 141 pages
ISBN: 978-3-89336-658-3

78-1. **18th World Hydrogen Energy Conference 2010 – WHEC2010 Proceedings**
Parallel Sessions Book 1:
Fuel Cell Basics / Fuel Infrastructures
ed. by D. Stolten, T. Grube (2010), ca. 460 pages
ISBN: 978-3-89336-651-4

78-2. **18th World Hydrogen Energy Conference 2010 – WHEC2010 Proceedings**
Parallel Sessions Book 2:
Hydrogen Production Technologies – Part 1
ed. by D. Stolten, T. Grube (2010), ca. 400 pages
ISBN: 978-3-89336-652-1

78-3. **18th World Hydrogen Energy Conference 2010 – WHEC2010 Proceedings**
Parallel Sessions Book 3:
Hydrogen Production Technologies – Part 2
ed. by D. Stolten, T. Grube (2010), ca. 640 pages
ISBN: 978-3-89336-653-8

78-4. **18th World Hydrogen Energy Conference 2010 – WHEC2010 Proceedings**
Parallel Sessions Book 4:
Storage Systems / Policy Perspectives, Initiatives and Cooperations
ed. by D. Stolten, T. Grube (2010), ca. 500 pages
ISBN: 978-3-89336-654-5

78-5. **18th World Hydrogen Energy Conference 2010 – WHEC2010 Proceedings**
Parallel Sessions Book 5:
Stategic Analysis / Safety Issues / Existing and Emerging Markets
ed. by D. Stolten, T. Grube (2010), ca. 530 pages
ISBN: 978-3-89336-655-2

78-6. **18th World Hydrogen Energy Conference 2010 – WHEC2010 Proceedings**
Parallel Sessions Book 6:
Stationary Applications / Transportation Applications
ed. by D. Stolten, T. Grube (2010), ca. 330 pages
ISBN: 978-3-89336-656-9

78 Set (complete book series)

18th World Hydrogen Energy Conference 2010 – WHEC2010 Proceedings
ed. by D. Stolten, B. Emonts, T. Grube (2010)
ISBN: 978-3-89336-657-6

79. **Ultrafast voltex core dynamics investigated by finite-element micromagnetic simulations**
by S. Gliga (2010), vi, 144 pages
ISBN: 978-3-89336-660-6

80. **Herstellung und Charakterisierung von keramik- und metallgestützten Membranschichten für die CO_2-Abtrennung in fossilen Kraftwerken**
von F. Hauler (2010), XVIII, 178 Seiten
ISBN: 978-3-89336-662-0

81. **Experiments and numerical studies on transport of sulfadiazine in soil columns**
by M. Unold (2010), xvi, 115 pages
ISBN: 978-3-89336-663-7

82. **Prompt-Gamma-Neutronen-Aktivierungs-Analyse zur zerstörungsfreien Charakterisierung radioaktiver Abfälle**
von J.P.H. Kettler (2010), iv, 205 Seiten
ISBN: 978-3-89336-665-1

83. **Transportparameter dünner geträgerter Kathodenschichten der oxidkeramischen Brennstoffzelle**
von C. Wedershoven (2010), vi, 137 Seiten
ISBN: 978-3-89336-666-8

84. **Charakterisierung der Quellverteilung von Feinstaub und Stickoxiden in ländlichem und städtischem Gebiet**
von S. Urban (2010), vi, 211 Seiten
ISBN: 978-3-89336-669-9

85. **Optics of Nanostructured Thin-Film Silicon Solar Cells**
by C. Haase (2010), 150 pages
ISBN: 978-3-89336-671-2

86. **Entwicklung einer Isolationsschicht für einen Leichtbau-SOFC-Stack**
von R. Berhane (2010), X, 162 Seiten
ISBN: 978-3-89336-672-9

87. **Hydrogen recycling and transport in the helical divertor of TEXTOR**
by M. Clever (2010), x, 172 pages
ISBN: 978-3-89336-673-6

88. **Räumlich differenzierte Quantifizierung der N- und P-Einträge in Grundwasser und Oberflächengewässer in Nordrhein-Westfalen unter besonderer Berücksichtigung diffuser landwirtschaftlicher Quellen**
von F. Wendland et. al. (2010), xii, 216 Seiten
ISBN: 978-3-89336-674-3

89. **Oxidationskinetik innovativer Kohlenstoffmaterialien hinsichtlich schwerer Lufteinbruchstörfälle in HTR´s und Graphitentsorgung oder Aufarbeitung**
von B. Schlögl (2010), ix, 117 Seiten
ISBN: 978-3-89336-676-7

90. **Chemische Heißgasreinigung bei Biomassenvergasungsprozessen**
von M. Stemmler (2010), xv, 196 Seiten
ISBN: 978-3-89336-678-1

91. **Untersuchung und Optimierung der Serienverschaltung von Silizium-Dünnschicht-Solarmodulen**
von S. Haas (2010), ii, 202 Seiten
ISBN: 978-3-89336-680-4

92. **Non-invasive monitoring of water and solute fluxes in a cropped soil**
by S. Garré (2010), xxiv, 133 pages
ISBN: 978-3-89336-681-1

93. **Improved hydrogen sorption kinetics in wet ball milled Mg hydrides**
by L. Meng (2011), II, 119 pages
ISBN: 978-3-89336-687-3

94. **Materials for Advanced Power Engineering 2010**
ed. by J. Lecomte-Beckers, Q. Contrepois, T. Beck and B. Kuhn
(2010), 1327 pages
ISBN: 978-3-89336-685-9

95. **2D cross-hole MMR – Survey design and sensitivity analysis for cross-hole applications of the magnetometric resistivity**
by D. Fielitz (2011), xvi, 123 pages
ISBN: 978-3-89336-689-7

96. **Untersuchungen zur Oberflächenspannung von Kohleschlacken unter Vergasungsbedingungen**
von T. Melchior (2011), xvii, 270 Seiten
ISBN: 978-3-89336-690-3

97. **Secondary Organic Aerosols: Chemical Aging, Hygroscopicity, and Cloud Droplet Activation**
by A. Buchholz (2011), xiv, 134 pages
ISBN: 978-3-89336-691-0

98. **Chrom-bezogene Degradation von Festoxid-Brennstoffzellen**
von A. Neumann (2011), xvi, 218 Seiten
ISBN: 978-3-89336-692-7

99. **Amorphous and microcrystalline silicon applied in very thin tandem solar cells**
by S. Schicho (2011), XII, 190 pages
ISBN: 978-3-89336-693-4

100. **Sol-gel and nano-suspension electrolyte layers for high performance solid oxide fuel cells**
by F. Han (2011), iv, 131 pages
ISBN: 978-3-89336-694-1

101. **Impact of different vertical transport representations on simulating processes in the tropical tropopause layer (TTL)**
by F. Plöger (2011), vi, 104 pages
ISBN: 978-3-89336-695-8

102. **Untersuchung optischer Nanostrukturen für die Photovoltaik mit Nahfeldmikroskopie**
von T. Beckers (2011), xiii, 128 Seiten
ISBN: 978-3-89336-696-5

103. **Impact of contamination on hydrogenated amorphous silicon thin films & solar cells**
by J. Wördenweber (2011), XIV, 138 pages
ISBN: 978-3-89336-697-2

104. **Water and Organic Nitrate Detection in an AMS: Laboratory Characterization and Application to Ambient Measurements**
by A. Mensah (2011), XI, 111 pages
ISBN: 978-3-89336-698-9

105. **Entwicklung eines neuen Konzepts zur Steuerung der thermischen Ausdehnung von glaskeramischen Verbundwerkstoffen mit angepasster Fließfähigkeit am Beispiel der Hochtemperatur-Brennstoffzelle**
von E. Wanko (2011), xi, 134 Seiten
ISBN: 978-3-89336-705-4

106. **Tomographic reconstruction of atmospheric volumes from infrared limb-imager measurements**
by J. Ungermann (2011), xiv, 153 pages
ISBN: 978-3-89336-708-5

107. **Synthese und Identifizierung von substituierten Mg-Al-Cl Doppelhydroxidverbindungen mit Schwerpunkt IR-Spektroskopie**
von B. Hansen (2011), XII, 121 Seiten
ISBN: 978-3-89336-709-2

108. **Analysis of spatial soil moisture dynamics using wireless sensor networks**
by U. Rosenbaum (2011), xxii, 120 pages
ISBN: 978-3-89336-710-8

109. **Optimierung von APS-ZrO2-Wärmedämmschichten durch Variation der Kriechfestigkeit und der Grenzflächenrauhigkeit**
von M. E. Schweda (2011), 168 Seiten
ISBN: 978-3-89336-711-5

110. **Sorption of a branched nonylphenol isomer and perfluorooctanoic acid on geosorbents and carbon nanotubes**
by C. Li (2011), X, 102 pages
ISBN: 978-3-89336-716-0

111. **Electron Transport in the Plasma Edge with Rotating Resonant Magnetic Perturbations at the TEXTOR Tokamak**
by H. Stoschus (2011), iv, 113 pages
ISBN: 978-3-89336-718-4

112. **Diffusion and Flow Investigations in Natural Porous Media by Nuclear Magnetic Resonance**
by N. Spindler (2011), viii, 144 pages
ISBN: 978-3-89336-719-1

113. **Entwicklung und Erprobung des Hygrometer for Atmospheric Investigations**
von T. Klostermann (2011), IV, 118 Seiten
ISBN: 978-3-89336-723-8

114. **Application of functional gene arrays for monitoring influences of plant/seasons on bacterial functions and community structures in constructed wetlands (Bitterfeld, Germany)**
by J. Ning (2011), xiv, 157 pages
ISBN: 978-3-89336-724-5

115. **Wasseraustrag aus den Kathodenkanälen von Direkt-Methanol-Brennstoffzellen**
von A. Schröder (2011), VII, 228 Seiten
ISBN: 978-3-89336-727-6

116. **CITYZEN Climate Impact Studies**
ed. by M. Schultz (2011), 45 pages
ISBN: 978-3-89336-729-0

117. **Software Tools zum interoperablen Austausch und zur Visualisierung von Geodatensätzen über das Internet**
von M. Schultz, M. Decker, S. Lührs (2011), iv, 156 Seiten
ISBN: 978-3-89336-730-6

118. **Optimierung eines Leichtbaudesigns für ein SOFC-Brennstoffzellenstack**
von T. Nguyen-Xuan (2011), III, 154 Seiten
ISBN: 978-3-89336-732-0

119. **Institute of Energy and Climate Research IEK-6:**
Nuclear Waste Management & Reactor Safety Report 2009/2010
Material Science for Nuclear Waste Management
ed. by M. Klinkenberg, S. Neumeier, D. Bosbach (2011), 242 pages
ISBN: 978-3-89336-735-1

120. **Fate of the Antibiotic Sulfadiazine in Yangtze River Sediments: Transformation, Sorption and Transport**
by N. Meng (2011), XII, 111 pages
ISBN: 978-3-89336-736-8

121. **Thermodynamische Eigenschaften gasförmiger und kondensierter Verbindungen für Hochtemperaturanwendungen**
von T. Markus (2011), II, 131 Seiten
ISBN: 978-3-89336-728-3

122. **Ein neues LIF-Instrument für flugzeug- und bodengebundene Messungen von OH- und HO_2-Radikalen in der Troposphäre**
von S. Broch (2011), IV, 160 Seiten
ISBN: 978-3-89336-742-9

123. **Processes in the Yangtze River System - Experiences and Perspectives**
Workshop-Proceedings
ed. by S. Küpper, G. Subklew, R.-D. Wilken (2011), 83 pages
ISBN: 978-3-89336-744-3

124. **Thermo-Mechanical Properties of Mixed Ion-Electron Conducting Membrane Materials**
by B. Huang (2011), 130 pages
ISBN: 978-3-89336-746-7

125. **Growth, Etching, and Stability of Sputtered ZnO:Al for Thin-Film Silicon Solar Cells**
by J. I. Owen (2011), xv, 192 pages
ISBN: 978-3-89336-749-8

126. **Entwicklung geträgerter $Ba_{0,5}Sr_{0,5}Co_{0,8}Fe_{0,2}O_{3-\delta}$ Sauerstoff-Permeationsmembranen**
von F. Schulze-Küppers (2011), ii, 119 Seiten
ISBN: 978-3-89336-752-8

127. **Development of the 2-Component-Injection Moulding for Metal Powders**
by A. P. Cysne Barbosa (2011), XIV, 150 pages
ISBN: 978-3-89336-753-5

128. **Performance of Tungsten-Based Materials and Components under ITER and DEMO Relevant Steady-State Thermal Loads**
by G. H. Ritz (2011), X, 128 pages
ISBN: 978-3-89336-755-9

129. **Experimentelle Bestimmung und numerische Simulation von Viskositäten in Schlackesystemen unter Vergasungsbedingungen**
von T. Nentwig (2011), 156 Seiten
ISBN: 978-3-89336-756-6

130. **Development of Thin Film Oxygen Transport Membranes on Metallic Supports**
by Y. Xing (2012), iv, 117 pages
ISBN: 978-3-89336-765-8

131. **Release of Inorganic Trace Elements from High-Temperature Gasification of Coal**
by M. Bläsing (2012), XVIII, 145 pages
ISBN: 978-3-89336-772-6

132. **Rauchgasseitige Korrosion von Nickelbasislegierungen für zukünftige 700°C-Dampfkraftwerke**
von F. Lüttschwager (2012), 145 Seiten
ISBN: 978-3-89336-773-3

133. **In-Situ Raman Spectroscopy: A Method to Study and Control the Growth of Microcrystalline Silicon for Thin-Film Solar Cells**
by S. Muthmann (2012), x, 134 pages
ISBN: 978-3-89336-774-0

Energie & Umwelt / Energy & Environment
Band / Volume 133
ISBN 978-3-89336-774-0

JÜLICH
FORSCHUNGSZENTRUM